

ON SIGNAL PROCESSING AND ELECTROMAGNETIC MODELLING

APPLICATIONS IN ANTENNAS AND TRANSMISSION LINES

Jonas Lundbäck

Blekinge Institute of Technology
Doctoral Dissertation Series No. 2007:08
School of Engineering



**On Signal Processing and
Electromagnetic Modelling
Applications in Antennas and Transmission Lines**

Jonas Lundbäck

Blekinge Institute of Technology Doctoral Dissertation Series

No 2007:08

ISSN 1653-2090

ISBN 978-91-7295-109-9

On Signal Processing and Electromagnetic Modelling

Applications in Antennas and Transmission Lines

Jonas Lundbäck



Department of Signal Processing
School of Engineering
Blekinge Institute of Technology
SWEDEN

© 2007 Jonas Lundbäck
Department of Signal Processing
School of Engineering
Publisher: Blekinge Institute of Technology
Printed by Printfabriken, Karlskrona, Sweden 2007
ISBN 978-91-7295-109-9

Abstract

This doctoral thesis is comprised of five parts. The first three parts concern signal processing and electromagnetic modelling of multiport antennas. The last two parts concern signal processing and transmission line theory applied to wave splitting on transmission lines.

In Part I, the spherical vector wave expansion of the electromagnetic field is used to completely characterize a multiport antenna. A general framework for modelling an antenna configuration based on measurement data and numerical computation is obtained. The generic electromagnetic model for arbitrary multiport antennas or vector sensors is applied in direction of arrival (DOA) estimation.

Next, in Part II using the generic electromagnetic model (from Part I), we obtain the Cramér–Rao bound (CRB) for DOA and polarization estimation using arbitrary multiport antennas. In the Gaussian case, the CRB is given in terms of the transmission matrix, the spherical vector harmonics and its spatial derivatives. Numerical examples using an ideal Tripole antenna array and a non-ideal Tetrahedron antenna array are included.

In Part III, the theory of optimal experiments is applied to a cylindrical antenna near-field measurement setup. The D-optimal (determinant) formulation using the Fisher information matrix of the multipole coefficients in the spherical wave expansion of the electrical field result in the optimal measurement positions. The estimation of the multipole coefficients and corresponding electric field using the optimal measurement points is studied using numerical examples and singular value analysis.

Further, Part IV describes a Digital Directional Coupler (DDC), a device for wave splitting on a transmission line. The DDC is a frequency domain digital wave splitter based on two independent wide-band measurements of the voltage and the current. A calibration of the digital processor is included to account for the particular transmission line and the sensors that are employed. Properties of the DDC are analyzed using the CRB and an experiment where wave splitting was conducted on a coaxial-cable is accounted for.

Finally, in Part V the DDC has been designed and implemented for wave splitting on a medium voltage power cable in a power distribution station using low cost wide-band sensors. Partial discharge measurements are conducted on cross-linked polyethylene insulated power cables. The directional separation capabilities of the DDC are visualized and utilized to separate multiple reflections from partial discharges based on the direction of travel.

Contents

Preface	ix
Acknowledgements	xi
Thesis parts	xiii
Publication list	xv
Introduction	1
Thesis summary	33
Part	
I A Generic Electromagnetic Model for DOA Estimation Using Arbitrary Multiport Antennas	39
II Fundamental Limitations for DOA and Polarization Estimation with Applications in Array Signal Processing	49
III On the Design of Optimal Cylindrical Antenna Near-Field Measurements	71
IV Statistical Analysis of a Digital Directional Coupler for Transmission Line Measurements	97
V Partial Discharge Measurement Using a Digital Directional Coupler	121

Preface

During the years as a graduate student I have had the privilege to expand my knowledge in signal processing and electromagnetic theory where several applications have been studied, ranging from radar processing, radio astronomy, electromagnetic inverse problems and array processing. It has been very rewarding to combine my fields of interest. The mixture of the vast areas of signal processing and electromagnetic theory is fruitful, providing both an understanding of *e.g.*, signal manipulation and information theory as well as antenna design and electromagnetic wave propagation. This doctoral thesis concludes my work as a graduate student at the School of Mathematics and System Engineering at Växjö University.

The thesis consists of five parts, joined together by the combination of signal processing and electromagnetic theory. Part I-III concerns signal processing applications and antennas using the spherical vector wave expansion of the electromagnetic field, specifically modelling of multiport antennas, Cramér-Rao bound analysis of direction of arrival and polarization estimation, and sensitivity analysis of antenna measurements. In Part IV and V, a Digital Directional Coupler is put forward as a digital wave splitter for transmission lines. The directional separation is primarily applied to partial discharge measurements on power cables.

Parts

- I** A Generic Electromagnetic Model for DOA Estimation Using Arbitrary Multiport Antennas
- II** Fundamental Limitations for DOA and Polarization Estimation with Applications in Array Signal Processing
- III** On the Design of Optimal Cylindrical Antenna Near-Field Measurements
- IV** Statistical Analysis of a Digital Directional Coupler for Transmission Line Measurements
- V** Partial Discharge Measurement Using a Digital Directional Coupler

Acknowledgments

I am truly grateful for all the support, help and guidance that my supervisor Prof. Sven Nordebo has given me during the years that we have worked together. Sven has generously shared his knowledge and been a source of inspiration.

I wish to appreciatively acknowledge the people that I have had the pleasure to work with. I thank Prof. Bo Thidé at Uppsala University for giving me the opportunity to participate in the development of LOIS. Doc. Mats Gustafsson at Lund Institute of Technology has gladly contributed with his knowledge in antennas and electromagnetic theory. Dr. Thomas Biro, Prof. Börje Nilsson at Växjö University and Doc. Magnus Akke at Lund Institute of Technology, for our collaboration and joint efforts. I am grateful for the support and for the opportunity to conduct experiments given to me by Olle Corfitsson and Christian Gustavsson at Öresundskraft. Christer Stojj at Siverts IMA has generously contributed with knowledge and microwave equipment.

My gratitude goes to Therese Sjöden for our joint efforts and the fruitful discussions regarding everything and nothing. Many thanks are directed to *all* former and present colleagues at the department of Electrical Engineering. The department is an open and friendly atmosphere.

I would like to thank Prof. Edwin Marengo, Northeastern University for serving as my opponent and Prof. Anders Karlsson, Lund Institute of Technology, Prof. Peter Händel, Royal Institute of Technology, and Doc. Claes Hedberg, Blekinge Institute of Technology for serving on the committee at my dissertation.

Finally, I would like to thank my family for supporting me and for being interested in my work. To my wonderful wife Jessica, thank you for you and for being who you are.

*Jonas Lundbäck
Växjö, May 2007*

Thesis parts

Part I is published as:

J. Lundbäck, S. Nordebo and M. Gustafsson, "A Generic Electromagnetic Model for DOA Estimation Using Arbitrary Multiport Antennas", In *proceedings of the IEEE International Symposium on Antennas and Propagation*, pp. 2549-2552, Albuquerque, USA, July 2006.

Part II is published as:

S. Nordebo, M. Gustafsson and J. Lundbäck, "Fundamental Limitations for DOA and Polarization Estimation with Applications in Array Signal Processing", *IEEE Transactions on Signal Processing*, vol. 54, no. 10, pp. 4055-4061, October 2006.

Part III is published as:

J. Lundbäck, "On the Design of Optimal Cylindrical Antenna Near-Field Measurements", *Research Report 07043*, ISSN 1650-2647, VXU/MSI/EL/R/-07043/-SE, Växjö University, Sweden, March 2007.
To be submitted.

Part IV is submitted as:

J. Lundbäck and S. Nordebo, "Statistical Analysis of a Digital Directional Coupler for Transmission Line Measurements", submitted to *IEEE Transactions on Circuits and Systems I*.

Part V is submitted as:

J. Lundbäck, S. Nordebo and T. Biro, "Partial Discharge Measurement Using a Digital Directional Coupler", submitted to *IEEE Transactions on Instrumentation and Measurements*.

Publication list

Theses

On Parameter Estimation - Applications in Radio Astronomy and Power Networks, Licentiate Thesis, No. 2005:09, Blekinge Institute of Technology.

Journal papers

S. Nordebo, M. Gustafsson and J. Lundbäck, "Fundamental Limitations for DOA and Polarization Estimation with Applications in Array Signal Processing", *IEEE Transactions on Signal Processing*, vol. 54, no. 10, pp. 4055-4061, October 2006.

J. Lundbäck and S. Nordebo, "Statistical Analysis of a Digital Directional Coupler for Transmission Line Measurements", submitted to *IEEE Transactions on Circuits and Systems I*.

J. Lundbäck, S. Nordebo and T. Biro, "Partial Discharge Measurement Using a Digital Directional Coupler", submitted to *IEEE Transactions on Instrumentation and Measurements*.

Conference Papers

S. Nordebo, A. Mohammed and J. Lundbäck, "On the Capacity of Polarization Diversity Antennas in Satellite Communications", In *proceedings of RadioVetenskap och Kommunikation 02*, Stockholm, Sweden, June 2002.

S. Nordebo and J. Lundbäck, "On Signal Separation Using Polarization Diversity and Tripole Arrays", In *proceedings of Mathematical Modeling of Wave Phenomena*, Växjö, Sweden, November 2002.

J. Lundbäck and S. Nordebo, "Linear Independence of Steering Vector in Polarization Estimation with Tripole Antennas", In *proceedings of the IEEE International Symposium on Antennas and Propagation*, Columbus, Ohio, USA, June 2003.

J. Lundbäck and S. Nordebo, "Analysis of a Tripole Array for Polarization and Direction of Arrival Estimation", In *proceedings of the Third IEEE Sensor Array and Multichannel Signal Processing Workshop*, pp. 284-288, Sitges, Spain, July 2004.

J. Lundbäck and S. Nordebo, "FMCW Radar for Fault Localization on Power Lines", In *proceedings of RadioVetenskap och Kommunikation 05*, Linköping, Sweden, June 2005.

J. Lundbäck, S. Nordebo and M. Gustafsson, "A Generic Electromagnetic Model for DOA Estimation Using Arbitrary Multiport Antennas", In *proceedings of the IEEE International Symposium on Antennas and Propagation*, pp. 2549-2552, Albuquerque, USA, July 2006.

Reports

J. Lundbäck, S. Nordebo, M. Akke and T. Biro, "On Fault Localization on Power Lines - An FMCW Based Fault Locator", *Research Report 05030*, ISSN 1650-2647, VXU/MSI/EL/R/-05030/-SE, Växjö University, Sweden, April 2005.

J. Lundbäck, S. Nordebo, T. Biro and O. Corfitsson, "Direction separation of Partial Discharges Using a Digital Directional Coupler", *Research Report 07042*, ISSN 1650-2647, VXU/MSI/EL/R/-07042/-SE, Växjö University, Sweden, March 2007.

J. Lundbäck, "On the Design of Optimal Cylindrical Antenna Near-Field Measurements", *Research Report 07043*, ISSN 1650-2647, VXU/MSI/EL/R/-07043/-SE, Växjö University, Sweden, March 2007.

Introduction

In the research-field of signal processing, many topics are directly connected to other research areas. The interdisciplinary combination can be more or less extensive and include concepts that have developed independently during the years. As an example, consider applications involving processing of signals obtained from antennas. An accurate mathematical model of the signals is based on the physical understanding and mathematical modelling of the antennas. Development of advanced algorithms involving the antenna signals can therefore benefit from this interdisciplinary mixture.

Signal processing is sometimes referred to as the manipulation of signals received from some type of sensor *e.g.*, an antenna. Just as the sensors vary from one application to another, so does the actual processing of the signals. In model-based signal processing, the signal obtained can be traced to a physical process and a corresponding mathematical model of the signal can be obtained. In this thesis, signal processing is combined with electromagnetic theory to obtain further knowledge and to support applications in the areas of antennas and transmission lines.

The parts of this doctoral thesis can be read individually since each part is based on a publication. To clarify and simplify the tools used herein, both in signal processing and in electromagnetic modelling; an introduction to selected topics related to the parts of the thesis is included. A collection of references is provided for further reading. The treatment is by no means complete and should serve as a short introduction.

First, the Cramér-Rao bound is described assuming both complex and real parameters. Detailed formulas that are used in this thesis are provided. The Cramér-Rao bound is an important and often exploited tool in statistical signal processing, a quantitative tool for the achievable accuracy in parameter estimation problems. Thereafter follows a brief summary of the spherical vector wave expansion of the electromagnetic field, which is frequently employed in *e.g.*, antenna measurements, electromagnetic inverse problems and scattering. The mathematical modelling of the electric field using this approach provide a generic model that can be analyzed and exploited in *e.g.*, estimation theory in array processing. Finally, a summary of the field of partial discharge diagnostics on power cables is included. This area has received much attention during the last decade where signal processing capabilities in conjunction with the advancement of integrated electronics have improved the diagnostic tools that researchers have provided.

The thesis consists of five parts. Part I concern the modelling of an ar-

bitrary multiport antenna or vector sensor using the spherical vector wave expansion of the electromagnetic field in the context of direction of arrival estimation. In Part II, the spherical vector wave expansion of the electromagnetic field of an arbitrary multiport antenna is utilized in combination with the Cramér-Rao bound to obtain an understanding of the fundamental limits of direction of arrival and polarisation estimation in array processing. In Part III, a cylindrical antenna near-field measurement is designed as an optimal experiment based on the Fisher information matrix of the multipole coefficients of the electrical field. Parts I, II and III were partially supported financially by the Swedish Research Council.

Further, in Part IV, a Digital Directional Coupler (DDC) for direction separation of travelling waves on transmission lines is detailed. This device conduct wave splitting based on digital signal processing. Finally, in Part V the DDC is applied to partial discharge measurements for direction based separation of partial discharge pulses on power cables. Part IV and V were partially funded by the Swedish Knowledge Foundation. Experiments have been conducted in collaboration with Öresundskraft. A patent based on Part IV and Part V, detailing the functionality of the DDC has been submitted, AWAPATENT AB Ref: SE-21028018.

On the Cramér-Rao bound

For many decades the Cramér-Rao Bound (CRB) [Sch91, SM97, Tre01] has been one of the most applied tools for performance investigations in parameter estimation problems. In 1922, the Cramér-Rao inequality for nonrandom parameters was introduced by Fisher [Fis22] and a few years later derived independently by Cramér [Cra46] and Rao [Rao45]. In estimation theory, the bound is an important tool and provide a lower bound on the variance of an unbiased estimator $\hat{\theta}$ of a parameter θ . The performance of an unbiased estimator is then evaluated through the comparison of the variance of the estimator and the CRB. This will provide insight into the accuracy of the estimator as function of model parameters, sometimes including the parameters that are to be estimated. Due to the applicability and usefulness of the CRB, much research regarding the properties of the CRB has been published, see *e.g.*, [SM90, SO96, Bos94]

From the theory of the CRB an efficient estimator (if it exists) can be deduced. If this is not the case the CRB does not provide any information on how to find an estimator. However, the CRB has the important connection with the Maximum likelihood (ML) method, that asymptotically the variance of the ML estimator is approximately equal to the CRB, see *e.g.*, [SN90a, VSO97, KV96]. Hence, the ML estimator is an asymptotically effective estimator for large number of samples, if the number of unknown parameters does not increase with the number of samples [SN90b, SM97]. Any other estimator can be compared to the CRB which then approximate the variance of the ML estimator. Yet another advantage of the CRB is that the bound is relatively easy to compute compared to other bounds [Tre01, SM97], especially for Gaussian distributed data.

The CRB has been used extensively in parameter estimation, see *e.g.*, [YD05, BAM05, SJL97, AH06] and in array processing, *e.g.*, [Tre02, SN90a, SMFS89]. As a natural extension to array signal processing, electromagnetic properties of antennas or wave propagation are often included in the signal model. This provides a closer connection between signal processing and electromagnetic modelling where the CRB is employed, see *e.g.*, [WZ00, Li93, SV93, HTT98, WF93, LS94, HN95, HTT97, HTN99, WLZ04, Won01, HN96, TSR04, WF91, NP94, NGP07, NG06, GN06, NG05b, MD99, MDG04]. Although fruitful, the application might be less useful if the electromagnetic model is too ideal, *e.g.*, disregarding the mutual coupling between antennas in an arbitrary vector sensor [QQS05].

Even though no actual estimator is available, the CRB by itself is of in-

terest. The bound can provide information regarding the estimation problem and the incorporated parameters that influence the problem formulation. So by analysing the CRB, knowledge of the problem formulation can be obtained. This is especially of interest if interpretations of the CRB can lead to increased knowledge and deeper understanding of the underlying physics. Hence, the combination of statistical signal processing and electromagnetic theory yields useful tools for analysing fundamental physical limitations. By utilizing the CRB, information regarding the physical properties or model specific properties included in the signal processing model can be interpreted and exploited to improve the goal of the application, see *e.g.*, [HN06, OM05, PRWP05, DL05].

Assume that the data observed using appropriate sensors is complex-valued $\mathbf{x} \in \mathcal{C}$ and the corresponding probability density function (PDF) $p(\mathbf{x}; \boldsymbol{\theta})$ is known. In many applications the parameters are real-valued and the extension to complex-valued parameters is often made by separation of the complex parameters into real and imaginary parts [Kay93a]. Yet another approach is to describe the complex-valued parameters by a linear transformation of the real-valued parameters [Smi05, Col05].

The CRB for a vector parameter $\boldsymbol{\theta}$, $[\boldsymbol{\theta}]_i = \theta_i$ is obtained as

$$\mathcal{E} \left\{ |\hat{\theta}_i - \theta_i|^2 \right\} \geq [\boldsymbol{\mathcal{I}}^{-1}(\boldsymbol{\theta})]_{ii}, \quad (1)$$

where $\mathcal{E} \{ \cdot \}$ denotes the expectation operator and $\boldsymbol{\mathcal{I}}$ is the Fisher information matrix (FIM), [Kay93b, Tre01, Fis22].

Consider both complex and/or real-valued parameters and define the gradient vector of the parameters $\boldsymbol{\theta}$ as,

$$\frac{\partial}{\partial \boldsymbol{\theta}} = \left(\frac{\partial}{\partial \theta_1}, \dots, \frac{\partial}{\partial \theta_i}, \dots, \frac{\partial}{\partial \theta_M} \right)^T, \quad (2)$$

where

$$\frac{\partial}{\partial \theta_i} = \begin{cases} \frac{\partial}{\partial \theta_i} & \text{when } \theta_i \in \mathcal{R} \\ \frac{1}{2} \left(\frac{\partial}{\partial x} - i \frac{\partial}{\partial y} \right) & \text{when } \theta_i \in \mathcal{C}. \end{cases} \quad (3)$$

Based on the regularity condition $\mathcal{E} \left\{ \frac{\partial}{\partial \boldsymbol{\theta}} \ln p(\mathbf{x}; \boldsymbol{\theta}) \right\} = \mathbf{0}$, (which follows from the demand of an unbiased estimator) and Cauchy-Schwartz inequality, the FIM reads,

$$\boldsymbol{\mathcal{I}}(\boldsymbol{\theta}) = \mathcal{E} \left\{ \frac{\partial}{\partial \boldsymbol{\theta}^*} \ln p(\mathbf{x}; \boldsymbol{\theta}) \left(\frac{\partial}{\partial \boldsymbol{\theta}} \ln p(\mathbf{x}; \boldsymbol{\theta}) \right)^T \right\}, \quad (4)$$

where $*$ denote the conjugate operation. Each element of the FIM is given by

$$[\mathcal{I}(\boldsymbol{\theta})]_{ij} = -\mathcal{E} \left\{ \frac{\partial^2}{\partial \theta_i^* \partial \theta_j} \ln p(\mathbf{x}; \boldsymbol{\theta}) \right\}. \quad (5)$$

In this thesis, the signal models consist of complex-valued signals with complex and/or real-valued parameters and noise that is complex Gaussian distributed [Mil74]. We therefore include the complex Gaussian PDF,

$$p(\mathbf{x}, \boldsymbol{\theta}) = \frac{1}{\pi \det \mathbf{R}(\boldsymbol{\theta})} \exp \left(-(\mathbf{x} - \boldsymbol{\mu}(\boldsymbol{\theta}))^H \mathbf{R}^{-1}(\boldsymbol{\theta}) (\mathbf{x} - \boldsymbol{\mu}(\boldsymbol{\theta})) \right), \quad (6)$$

where $(\cdot)^H$ denotes the Hermitian transpose, $\boldsymbol{\mu} = \mathcal{E}\{\mathbf{x}\}$ is the expectation value and $\mathbf{R} = \mathcal{E}\{(\mathbf{x} - \boldsymbol{\mu})(\mathbf{x} - \boldsymbol{\mu})^H\}$ is the covariance matrix. The expression for the FIM using complex-valued Gaussian data is then given as,

$$[\mathcal{I}(\boldsymbol{\theta})]_{ij} = \text{tr} \left\{ \frac{\partial \mathbf{R}}{\partial \theta_i^*} \mathbf{R}^{-1} \frac{\partial \mathbf{R}}{\partial \theta_j} \mathbf{R}^{-1} \right\} + \frac{\partial \boldsymbol{\mu}^H}{\partial \theta_i^*} \mathbf{R}^{-1} \frac{\partial \boldsymbol{\mu}}{\partial \theta_j} + \frac{\partial \boldsymbol{\mu}^H}{\partial \theta_j} \mathbf{R}^{-1} \frac{\partial \boldsymbol{\mu}}{\partial \theta_i^*}, \quad (7)$$

where $\text{tr}\{\cdot\}$ denote the trace operator.

Consider the estimation of $\boldsymbol{\alpha}$ where $\boldsymbol{\alpha} = \mathbf{g}(\boldsymbol{\theta})$. The vector parameter transformation is used and the CRB for $\boldsymbol{\alpha}$ is,

$$\mathcal{E} \{ |\hat{\alpha}_i - \alpha_i|^2 \} \geq \left[\frac{\partial \mathbf{g}(\boldsymbol{\theta})}{\partial \boldsymbol{\theta}} \mathcal{I}^{-1}(\boldsymbol{\theta}) \left(\frac{\partial \mathbf{g}(\boldsymbol{\theta})}{\partial \boldsymbol{\theta}} \right)^H \right]_{ii}. \quad (8)$$

Two special cases can be identified. First, when θ_i is purely real, $\partial/\partial \theta_i^* = \partial/\partial \theta_i$ and (7) reads

$$[\mathcal{I}(\boldsymbol{\theta})]_{ij} = \text{tr} \left\{ \frac{\partial \mathbf{R}}{\partial \theta_i} \mathbf{R}^{-1} \frac{\partial \mathbf{R}}{\partial \theta_j} \mathbf{R}^{-1} \right\} + 2\text{Re} \left\{ \frac{\partial \boldsymbol{\mu}^H}{\partial \theta_i} \mathbf{R}^{-1} \frac{\partial \boldsymbol{\mu}}{\partial \theta_j} \right\}, \quad (9)$$

which is the standard FIM formula for real-valued parameters in complex valued data [Kay93b]. Second, if $\boldsymbol{\mu}$ is analytic in θ_i (observe that \mathbf{R} can not be analytical in θ_i since $\mathbf{R} = \mathbf{R}^H$) then $\partial \boldsymbol{\mu} / \partial \theta_i^* = 0$ and the last term of (7) is equal to zero.

As a special case, when $\mathbf{R} = \sigma^2 \mathbf{I}$ and $\boldsymbol{\mu}$ is differentiable and analytical,

$$[\mathcal{I}(\boldsymbol{\theta})]_{ij} = \begin{cases} \frac{2}{\sigma^2} \text{Re} \left\{ \frac{\partial \boldsymbol{\mu}^H}{\partial \theta_i} \frac{\partial \boldsymbol{\mu}}{\partial \theta_j} \right\} & \theta_i \in \mathbb{R} \text{ and } \theta_j \in \mathbb{R} \\ \frac{1}{\sigma^2} \frac{\partial \boldsymbol{\mu}^H}{\partial \theta_i^*} \frac{\partial \boldsymbol{\mu}}{\partial \theta_j} & \theta_i \in \mathbb{C} \text{ and/or } \theta_j \in \mathbb{C}. \end{cases} \quad (10)$$

When the FIM has diagonal or block diagonal structure valuable information is obtained. This provides knowledge regarding the relation between the parameters. If the FIM is diagonal all parameters are uncoupled, while a block diagonal FIM indicates that the parameters can be arranged in subspaces where each subspace is uncoupled from the other. The parameters in a specific subspace could still be coupled within that subspace. Properties of the FIM and the corresponding CRB are analysed and exploited in Part II, Part III and Part IV of this thesis.

On the spherical vector wave expansion

Within the field of electromagnetic theory, especially the area of near-field measurements and antenna theory, a common and well known technique to describe a general electromagnetic field is the spherical vector wave expansion [Han88, Har61, Han35, Kri99, Thi07]. Much research concerning physical limitations of antennas in free space have been based on spherical waves, see *e.g.*, [Chu48, CR64, Col98, Har61], including the derivations of the optimal Q-value of a general antenna. The well defined mathematical theory of the spherical waves is a stable foundation for applications involving electromagnetic modelling that can benefit from the spherical wave expansion.

The combination of signal processing and antenna theory grows stronger, much research now include the two areas *e.g.*, Multiple Input, Multiple Output systems (MIMO) and Radar systems, see *e.g.*, [VBA03, JW04, JW05, GSV⁺07, FHB⁺06]. The spherical wave expansion of the electromagnetic field of an arbitrary antenna is done on a spherical surface enclosing the antenna. Since the antenna can be arbitrary, this approach of electromagnetic modelling provides a general framework to analyse the properties of the antenna from a signal processing perspective. Since many applications depend strongly on the antenna properties, a general description including all properties of the antenna is of great interest *e.g.*, in DOA estimation using the super-resolution techniques MUSIC and ESPRIT [LW90, RH89, KSS94, SS97, RK89, GSRK94].

Below, a short summary of the spherical wave expansion for the applications in this thesis is included.

In a spherical coordinate system, spherical vector waves are solutions to Maxwell's equations in a homogenous, linear and isotropic material without sources. The sources are confined within and surrounded by a spherical volume with radius a . In the exterior of the sphere, the electric and magnetic fields are expanded in spherical waves. From Maxwell's equations,

$$\begin{cases} \nabla \times \mathbf{E}(\mathbf{r}) &= -i\omega\mu\mathbf{H}(\mathbf{r}) \\ \nabla \times \mathbf{H}(\mathbf{r}) &= i\omega\epsilon\mathbf{E}(\mathbf{r}) \end{cases} \quad (11)$$

and utilizing that $\nabla \cdot \mathbf{E} = 0$ in a source-free surrounding, the Helmholtz vector wave equation reads

$$\nabla^2 \mathbf{E}(\mathbf{r}) + k^2 \mathbf{E}(\mathbf{r}) = \mathbf{0}, \quad (12)$$

where $k = 2\pi/\lambda$, λ the wavelength, ϵ and μ the permittivity and permeability, respectively.

The solution of the vector wave equation in a spherical coordinate system is obtained via a generating scalar function that is separable in the spherical variables r, θ, ϕ . The scalar wave equation in spherical coordinates is given by

$$\left(\frac{1}{r^2} \frac{\partial}{\partial r} \left(r^2 \frac{\partial}{\partial r} \right) + \frac{1}{r^2 \sin \theta} \frac{\partial}{\partial \theta} \left(\sin \theta \frac{\partial}{\partial \theta} \right) + \frac{1}{r^2 \sin^2 \theta} \frac{\partial^2}{\partial \phi^2} + k^2 \right) \Psi = 0, \quad (13)$$

and using the separation of variables method $\Psi(r, \theta, \phi) = R(r)T(\theta)P(\phi)$. Then, (13) can be reformulated as three ordinary differential equations since the three variables are independent [AW01],

$$\frac{d^2}{d\phi^2} P(\phi) + Q_1 P(\phi) = 0, \quad (14)$$

$$\frac{1}{\sin \theta} \frac{d}{d\theta} \left(\sin \theta \frac{d}{d\theta} T(\theta) \right) - \frac{Q_1}{\sin \theta} + Q_2 = 0, \quad (15)$$

$$\frac{d}{dr} \left(r^2 \frac{d}{dr} R(r) \right) + k^2 r^2 R(r) - Q_2 R(r) = 0, \quad (16)$$

where Q_1 and Q_2 are constants. The azimuth angle ϕ has a periodicity of 2π , a natural choice is to set $Q_1 = m^2$, $m = \dots, -1, 0, 1, \dots$. The solution to (14) consists of a complex exponential that has the same periodicity. Next, by setting $Q_2 = l(l+1)$, $l \geq 0$, (15) becomes the associated Legendre equation [AW01]. The general solutions are the *associated Legendre functions* $P_l^m(x)$ where $x = \cos \theta$. Further, (16) is identified as the spherical Bessel's equation with solutions consisting of linear combinations of spherical Bessel and Neumann functions. A linear combination of the two is the *spherical Hankel functions* $h_l^{(1)}(kr)$ and $h_l^{(2)}(kr)$ of first and second kind, respectively. When describing the electromagnetic field outside the sphere enclosing the sources centered at origin of the spherical coordinate system, the Hankel functions are used. For the employed time convention, $e^{i\omega t}$, the spherical Hankel functions of first and second kind correspond to incoming and outgoing propagation of spherical waves, respectively. Finally, combine the individual solutions of (14)-(16) to obtain $\Psi(r, \theta, \phi) = R(r)T(\theta)P(\phi)$, where

$$\begin{aligned} P(\phi) &= \frac{1}{\sqrt{2\pi}} e^{im\phi}, \quad m = \dots, -1, 0, 1, \dots \\ R(r) &= h_l^{(1)}(kr) \text{ or } h_l^{(2)}(kr), \quad l = 0, 1, 2, \dots \\ T(\theta) &= P_l^m(\cos \theta). \end{aligned} \quad (17)$$

Important properties of both $P(\phi)$ and $T(\phi)$ includes orthogonality,

$$\int_0^{2\pi} \frac{1}{\sqrt{2\pi}} e^{im\phi} \frac{1}{\sqrt{2\pi}} e^{-im'\phi} = \delta_{m,m'}, \quad (18)$$

and

$$\int_0^\pi P_l^m(\cos\theta)P_{l'}^m(\cos\theta)\sin\theta d\theta = \frac{2}{2l+1} \frac{(l+m)!}{(l-m)!} \delta_{l,l'}. \quad (19)$$

From the generating scalar function that solves the Helmholtz scalar wave equation, the scalar *spherical harmonics* are [AW01],

$$Y_{ml}(\hat{\mathbf{r}}) = (-1)^m \sqrt{\frac{2l+1}{4\pi}} \sqrt{\frac{(l-m)!}{(l+m)!}} P_l^m(\cos\theta) e^{im\phi}. \quad (20)$$

Next, the *spherical vector harmonics* $\mathbf{A}_{\tau ml}(\hat{\mathbf{r}})$ reads

$$\begin{cases} \mathbf{A}_{1ml}(\hat{\mathbf{r}}) &= \frac{1}{\sqrt{l(l+1)}} \nabla \times (\mathbf{r} Y_{ml}(\hat{\mathbf{r}})) \\ \mathbf{A}_{2ml}(\hat{\mathbf{r}}) &= \hat{\mathbf{r}} \times \mathbf{A}_{1ml} = \frac{1}{\sqrt{l(l+1)}} r \nabla Y_{ml}(\hat{\mathbf{r}}) \\ \mathbf{A}_{3ml}(\hat{\mathbf{r}}) &= \hat{\mathbf{r}} Y_{ml}(\hat{\mathbf{r}}) \end{cases} \quad (21)$$

and on the unit sphere,

$$\int_0^{2\pi} \int_0^\pi \mathbf{A}_{\tau ml}(\hat{\mathbf{r}}) \mathbf{A}_{\tau' m' l'}^*(\hat{\mathbf{r}}) d\Omega = \delta_{\tau, \tau'} \delta_{m, m'} \delta_{l, l'}. \quad (22)$$

A series expansion of the electric field in a source-free surrounding outside a sphere of radius a enclosing all sources and origo as described here is [AW01, Jac75, Han88]

$$\mathbf{E}(\mathbf{r}) = \sum_{l=1}^{\infty} \sum_{m=-l}^l \sum_{\tau=1}^2 f_{\tau ml} \mathbf{u}_{\tau ml}(k\mathbf{r}) + a_{\tau ml} \mathbf{v}_{\tau ml}(k\mathbf{r}), \quad (23)$$

where $r > a$, $f_{\tau ml}$ and $a_{\tau ml}$ are the multipole coefficients. Further, the *outgoing spherical vector waves* are given by

$$\begin{aligned} \mathbf{u}_{1ml}(k\mathbf{r}) &= h_l^{(2)}(kr) \mathbf{A}_{1ml}(\hat{\mathbf{r}}) \\ \mathbf{u}_{2ml}(k\mathbf{r}) &= \frac{1}{k} \nabla \times \mathbf{u}_{1ml}(k\mathbf{r}) = \\ &= \frac{(kr h_l^{(2)}(kr))'}{kr} \mathbf{A}_{2ml}(\hat{\mathbf{r}}) + \sqrt{l(l+1)} \frac{h_l^{(2)}(kr)}{kr} \mathbf{A}_{3ml}(\hat{\mathbf{r}}) \end{aligned} \quad (24)$$

and the *incoming spherical vector waves* reads,

$$\begin{aligned} \mathbf{v}_{1ml}(k\mathbf{r}) &= h_l^{(1)}(kr) \mathbf{A}_{1ml}(\hat{\mathbf{r}}) \\ \mathbf{v}_{2ml}(k\mathbf{r}) &= \frac{1}{k} \nabla \times \mathbf{v}_{1ml}(k\mathbf{r}). \end{aligned} \quad (25)$$

The value of l is the order of the *modes* $m = -l, \dots, l$. The electrical field described by (23) is a solution to Helmholtz vector wave equation (12), [AW01, Jac75, Han88]. Since $\nabla \cdot \mathbf{u}_{1ml}(k\mathbf{r}) = \nabla \cdot \mathbf{u}_{2ml}(k\mathbf{r}) = 0$, $\mathbf{u}_{1ml}(k\mathbf{r})$ and $\mathbf{u}_{2ml}(k\mathbf{r})$ are suitable for describing the outgoing electrical field in a source-free surrounding.

For analysing transmitting antennas without accounting for scattering, it is enough to consider a description of the transmitted (outgoing) electrical field given by (23) where $a_{\tau ml} = 0$,

$$\mathbf{E}(\mathbf{r}) = \sum_{l=1}^{\infty} \sum_{m=-l}^l \sum_{\tau=1}^2 f_{\tau ml} \mathbf{u}_{\tau ml}(k\mathbf{r}). \quad (26)$$

Using Faradays law (11), the corresponding magnetic field is

$$\mathbf{H}(\mathbf{r}) = -\frac{1}{i\eta} \sum_{l=1}^{\infty} \sum_{m=-l}^l \sum_{\tau=1}^2 f_{\tau ml} \mathbf{u}_{\bar{\tau} ml}(k\mathbf{r}), \quad (27)$$

where $\tau = 1, 2$ corresponds to $\bar{\tau} = 2, 1$.

All multipoles corresponding to $\tau = 1$ are named magnetic multipoles or transversal electrical multipoles while multipoles with $\tau = 2$ are named electrical multipoles or transversal magnetic multipoles. Since $\hat{\mathbf{r}} \cdot \mathbf{u}_{1ml}(\hat{\mathbf{r}}) = 0$, $\mathbf{u}_{1ml}(\hat{\mathbf{r}})$ describe the transversal part of the electric or magnetic field.

The total transmitted power through a sphere of radius a is given by the sum of the absolute square of the multipole coefficients,

$$P = \frac{1}{2\eta k^2} \sum_{l=1}^{\infty} \sum_{m=-l}^l \sum_{\tau=1}^2 |f_{\tau ml}|^2. \quad (28)$$

The power transported by each mode is therefore independent of all other modes.

In all practical applications the sum of l is finite, $l = 1, 2, \dots, L$ where L is the maximum order of modes. The maximum order L is determined by the electrical size and bandwidth of the antenna [Han88, NG05a, Fan50]. According to [Han88], L can be determined by the empirical rule

$$L = [ka] + n_1, \quad (29)$$

where $[\cdot]$ denotes the closest larger integer and n_1 is an integer constant that varies in value depending on the application. For most practical purposes in

spherical antenna near-field measurements $n_1 = 10$ is considered sufficient [Han88].

A second approach to obtain L , consider [NG05a, Fan50, GN04, NG04, CR64] where the transmission coefficients for each mode can be calculated as

$$|t_l| \leq \sqrt{1 - e^{-\frac{2\pi}{Q_l} \frac{1-B^2/4}{B}}}, \quad (30)$$

where B is the fractional bandwidth and Q_l the Q-factors of each mode l . By utilizing modes up to a certain power level $P_{\tau ml} \leq \epsilon$ the maximum mode order L satisfies

$$P_{\tau mL} = \frac{1}{2\eta k^2} |f_{\tau mL}|^2 \leq |t_L|^2 P_{\text{in}} \leq \epsilon, \quad (31)$$

where P_{in} is the input power.

At a large distance from the antenna *i.e.*, in the far-field of the antenna where $kr \gg a$, we can approximate the spherical Hankel functions

$$h_l^{(2)}(kr) \approx (-i)^{l+1} \frac{e^{-ikr}}{kr} \quad (32)$$

and from (26) obtain the electrical far-field

$$\mathbf{E}(\mathbf{r}) = \frac{e^{-ikr}}{kr} \sum_{l=1}^L \sum_{m=-l}^l \sum_{\tau=1}^2 i^{l+2-\tau} f_{\tau ml} \mathbf{A}_{\tau ml}(\hat{\mathbf{r}}) = \frac{e^{-ikr}}{kr} \mathbf{F}(\hat{\mathbf{r}}), \quad (33)$$

where $\mathbf{F}(\hat{\mathbf{r}})$ is the far-field amplitude. An important property observed in (33) is that based on the orthonormality of the spherical vector harmonics,

$$f_{\tau ml} = i^{-l-2+\tau} \int \mathbf{A}_{\tau ml}^*(\hat{\mathbf{r}}) \cdot \mathbf{F}(\hat{\mathbf{r}}) d\Omega. \quad (34)$$

Orthogonality of the spherical vector waves $\mathbf{u}_{\tau ml}$ is applied in antenna near-field measurements where the objective is to estimate the multipole coefficients from the measured electromagnetic field transmitted from the antenna under test (AUT) [Han88]. This is known as the inverse problem in antenna measurements, see *e.g.*, [Lai05]. To obtain the multipole coefficients based on samples of the electric and/or magnetic field, several methods have been suggested that could include probe calibration, *e.g.*, [Han97, LPB06]. Methods without probe calibration is often based directly on (26) and a least-square

solution [Han88]. Using the estimated multipole coefficients, important parameters of the AUT can be calculated *e.g.*, the directivity, far-field pattern etc. The task of antenna measurement is often discussed in terms of numerical algorithms and experiment design involving *e.g.*, probe correction [Lar80] and measurement configuration [HRs99].

In Part III of this thesis, the theory of optimal experiment design is applied in a cylindrical antenna measurement configuration, see *e.g.*, [AD92, Fed72, EN98, VBW98, WGF06, XC04]. Based on an optimization formulation using the Fisher information matrix, the measurement strategy or the measurement positions are obtained. Properties of the optimization formulation and the result of the inverse problem are analysed using numerical examples and singular value analysis.

An arbitrary antenna can conveniently be described as a spherical wave guide with one port connected to the transmitter or receiver and several radiating ports, one port for each multipole coefficient. Properties of the antenna in transmission and receiving mode and scattering properties are then described by a linear relationship between the complex multipole coefficients, transmitted signal x^+ and received signal x^- . For notation simplification, the multi-index $\alpha = (\tau, m, l)$ is introduced, $f_{\tau ml} = f_\alpha$. Also, normalization of the power is chosen such that the transmitted and received power equals $|x^+|^2/(2Z_g)$ and $|x^-|^2/(2Z_g)$, respectively, where Z_g is the impedance of the propagating wave guide mode (often $Z_g = 1$ is chosen for simplicity). The antenna scattering matrix (one input port) of size $2L(L+2)+1$ is given by,

$$\begin{pmatrix} \Gamma & \mathbf{R} \\ \mathbf{T} & \mathbf{S} \end{pmatrix} \begin{pmatrix} x^+ \\ \mathbf{a} \end{pmatrix} = \begin{pmatrix} x^- \\ \mathbf{f} \end{pmatrix}, \quad (35)$$

where Γ is the antenna reflection coefficient, \mathbf{R} ($1 \times 2L(L+2)$) is the antenna receiving coefficients, \mathbf{T} ($2L(L+2) \times 1$) is the antenna transmission coefficients and \mathbf{S} ($2L(L+2) \times 2L(L+2)$) is the antenna scattering matrix. The total scattering matrix of (35) is unitary if the antenna is lossless. Also, \mathbf{f} and \mathbf{a} are the vector representation of the multipole coefficients.

For receiving antennas, the voltages corresponding to the received signals are related to the far-field amplitude of the antennas via the effective length or size [Bal97]. A slightly different approach based on (35) is considered here, see Fig 1. By reciprocity, the receiving multiport antenna is characterized in terms of the transmission matrix from incident voltage waves to multipole coefficients of the outgoing spherical vector waves.

Let x_i^+ and x_i^- denote the incident and reflected voltages at the antenna waveguide connections for $i = 1, \dots, N$. These voltages are normalized so

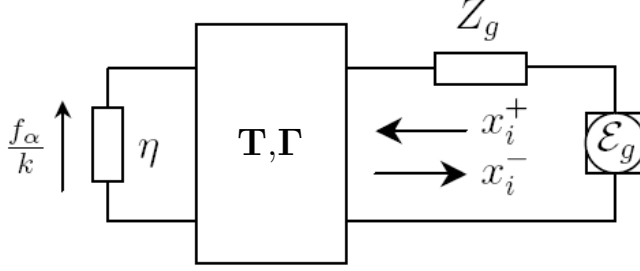


Figure 1: An arbitrary multiport antenna where the transmitter is located to the right and the radiating part of the antenna to the left.

that the power delivered to a particular antenna port is $\frac{|x_i^+|^2}{2Z_g}$ and the corresponding reflected power is $\frac{|x_i^-|^2}{2Z_g}$. On transmission from the input terminals with incident voltage waves x_i^+ , the transmitted wave field f_α is given by

$$\begin{bmatrix} \frac{f_\alpha}{k} \end{bmatrix} = \mathbf{T} \mathbf{x}^+ \sqrt{\frac{\eta}{Z_g}}, \quad (36)$$

where $\mathbf{T} = [T_{\alpha i}]$ is the $2L(L+2) \times N$ properly scaled transmission matrix which maps the vector of incident voltages $\mathbf{x}^+ = [x_i^+]$ to propagated multipoles f_α . Compare to (35) where only one incident signal is transmitted. Here, \mathbf{T} has N columns and a slightly different scaling is applied. However, (35) could be extended to describe a multiport antenna, see *e.g.*, [GN06]. The reflected voltages are given by $\mathbf{x}^- = \mathbf{\Gamma} \mathbf{x}^+$ where $\mathbf{\Gamma}$ ($N \times N$) is the reflection matrix. For power conservation,

$$\mathbf{\Gamma}^H \mathbf{\Gamma} + \mathbf{T}^H \mathbf{T} \leq \mathbf{I} \quad (37)$$

holds with equality for lossless antennas.

Consider one incident signal x_i^+ ,

$$x_i^- x_i^+ = -i \frac{\lambda^2}{2\pi} \frac{Z_g}{\eta} \mathbf{F}(\hat{\mathbf{k}}_0) \cdot \mathbf{E}_0 \quad (38)$$

follows from the antenna reciprocity theorem [DPG⁺98] where \mathbf{E}_0 is the complex vector amplitude of a plane wave $\mathbf{E}_0 e^{-ik\hat{\mathbf{k}}_0 \cdot \mathbf{r}}$ incident from direction $\hat{\mathbf{k}}_0$ and x_i^- the corresponding received signal. Here, $\mathbf{F}(\hat{\mathbf{r}})$ (33) is the far-field amplitude corresponding to the transmitted signal x_i^+ . From (33) and (38), the received vector signal is

$$\mathbf{x}^- = \sqrt{\frac{Z_g}{\eta}} \lambda \mathbf{R} \mathbf{A} \mathbf{E} \quad (39)$$

where $\mathbf{R} = \mathbf{T}^T$, \mathbf{A} ($2L(L+2) \times 2$) is a matrix where each column corresponds to the spherical components of the spherical vector harmonics $i^{l+1-\tau} \mathbf{A}_\alpha(\hat{\mathbf{k}}_0)$, and \mathbf{E} is an 2×1 vector containing the corresponding signal components of the electric field \mathbf{E}_0 .

Finally, the extension to K incoming vector signals result in

$$\mathbf{x}^- = \sqrt{\frac{Z_g}{\eta}} \lambda \sum_{k=1}^K \mathbf{R} \mathbf{A}_k \mathbf{E}_k \quad (40)$$

and in the case of completely polarized signals $\mathbf{E}_k = \mathbf{E}_k^0 s_k$,

$$\mathbf{x}^- = \mathbf{H} \mathbf{s}, \quad (41)$$

where the columns of \mathbf{H} are given by,

$$[\mathbf{H}]_k = \sqrt{\frac{Z_g}{\eta}} \lambda \mathbf{R} \mathbf{A}_k \mathbf{E}_k^0 \quad (42)$$

and $[\mathbf{s}]_k = s_k$. If a different multiport antenna should be investigated, only \mathbf{R} in (42) should be replaced by the corresponding receiving matrix of the desired antenna.

In Part I, the method of obtaining the signal model for an multiport antenna introduced here is described and applied in DOA estimation. In Part II, based on the generic electromagnetic model is an analysis of the physical limitations for DOA and polarization estimation using multiport antennas.

On partial discharge diagnostics

The modern society in its present form is strongly dependent on continuous power supply. This is especially true for the industry but also for the community and its citizens. To meet the demands the power companies needs to apply methods for continuous surveillance of the power network in order to obtain early warning signals from faulty equipment, see *e.g.*, [ZQC06, Mon06, FS06]. Assessments regarding if a repair or replacement of the equipment is necessary should be supported by fault indications. One method of fault indication supported assessment is Partial Discharge (PD) diagnostics that is based on the insulation properties of the electrical equipment.

Although used as a diagnostic tool, PD measurements are also used by the manufacturers of electrical equipment to evaluate the design and to assure that requirements are met regarding the insulation properties. Here, the focus is on power cables. However, PD diagnostics is used in connection with other electrical devices *e.g.*, stator bars, transformers or capacitors [Bar02].

A presence of PD can indicate electrical, mechanical, thermal or environmental aging [Sto05]. PD diagnostics can be applied either off-line or on-line where the former means that the device under test is not subjected to ordinary operational conditions *e.g.*, no voltage is applied and the equipment under test is disconnected from other devices.

Partial discharges are small and fast electrical sparks resulting from electrical breakdown in a gas filled void *e.g.*, an air filled cavity in the insulation of a power cable. In this situation the cavity might be filled with air inside or on the surface of the insulation. This can be caused by a damage occuring at the installation or it can result from degradation of the insulation material due to aging [Sto05].

If the cavity is subjected to a sinusoidal voltage, a breakdown can occure when the applied voltage exceed the breakdown level and a free electron can initiate the electron flow accross the cavity [Bar02]. This process results in a short current pulse, typically measured in nanoseconds, due to the charge carried by the electron flow. Interesting properties of the PD pulse includes the amplitude, the time duration and the point of occurence related to the phase of the applied sinusoidal voltage.

The partial discharge is regarded as a stochastic process with all of its parameters stochastic variables that depend on the creation process see *e.g.*, [Hei99, Bar02, GB95, CMF00]. The parameters of successive recordings of PD pulses are used in an effort to identify the cause of the PD but also to

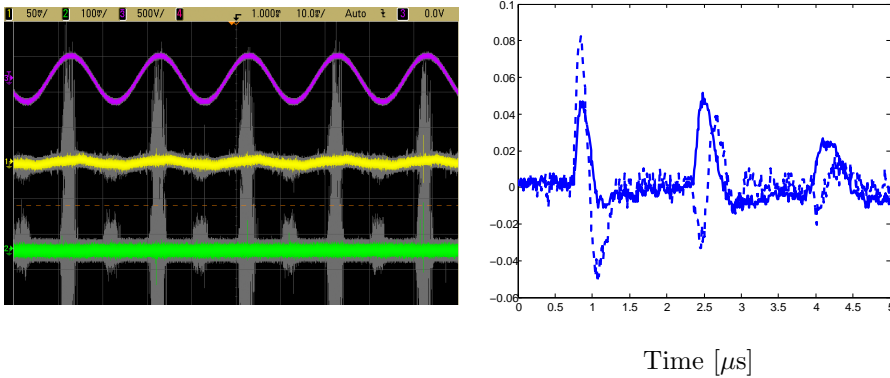


Figure 2: A picture of the oscilloscope window in one measurement where the infinite persistence is applied (left figure). The top curve is the applied voltage (scaled to 220 V), the middle and bottom curves are the voltage sensor and current sensor signals, respectively. The setting on the oscilloscope is 10 ms/div, 50 mV and 100 mV for the two sensors, respectively. In the right figure is shown one PD pulse (to the left) and multiple reflections occurring in the system of power cables. The solid and dashed curves correspond to the voltage and current sensor, respectively.

separate multiple PD sources, see *e.g.*, [CCM⁺02, BHN06, SSB05, SB02].

The ongoing research of PD diagnostics has produced several apparatus that have been commercially available *e.g.*, [SHV91, Mas00, Sto05]. Most of the PD diagnostic equipment available are off-line technologies [Vee05]. However, off-line techniques can affect the properties of the partial discharges that may depend on other factors such as mechanical or thermal stress. Instead, on-line PD diagnostics provides means to continuously monitor the current state of the power cable during regular operation. This requires a different approach using sensors that must sustain operational conditions.

The usage of advanced signal processing has been extensively applied, especially since the cost of processing power has decreased. Continuous monitoring can provide early warnings and indications of degradations in the power cable system. This combined with a long-term history of the power cables condition would be most useful in determining the present state of the power cables.

The final result would provide an instrument for early warnings of impending problems but it might never give an estimation of the remaining life time of the monitored equipment [Sto05].

On-line PD diagnostics has not been used extensively but rather received large attention during the last decade [Sto05], this mostly due to the rapid improvement in integrated electronics enabling *e.g.*, the usage of more advanced noise reduction techniques.

One fundamental part of a PD diagnostic technique is to handle the large amount of noise and interference that are present in PD measurements [SSS00, LPP03]. The noise and interference includes components of different nature *e.g.*, wide-band background noise, narrow-band interference and pulse-shaped disturbances, see *e.g.*, [LPP03, BD00, And98]. Many different noise reduction techniques have been proposed. One classification of noise reduction techniques is open-loop and closed-loop techniques [SSS01] where closed-loop techniques refers to a situation where a reference signal is used to measure the noise and interference *e.g.*, an external antenna. Open-loop techniques includes filtering, spectral analysis and wavelets analysis see *e.g.*, [VW03, AS98, KG05] and references therein.

The art of detecting, characterization and localization of PD in power cable systems has been investigated in many studies and publications. Detection and characterization can be performed in several ways *e.g.*, statistical analysis using probabilistic quantities related to the PD signal [GK92]. Other techniques that have received much attention are Neural Networks, Fuzzy Logic and Pattern Recognition, see *e.g.*, [Bar02, SB02, CCM⁺02].

In the context of localization of PD sites on power cables, several different types of solutions have been reported *e.g.*, off-line time domain reflectrometry and synchronization of dual-end measurements using Global Positions System (GPS) [Vee05]. In [Vee05], a reference signal is injected in the power cable, providing a basis for difference-in-time-of-arrival (DTOA) measurement which outperforms the GPS based system under certain conditions. The task of localization is dependent on the system at hand and on the characteristics of the power cables under investigation. Power cables have a large attenuation for high frequencies so PD pulses are likely to be distorted and attenuated [BPW96]. This affects the timing resolution of the diagnostic system. Further, timing resolution is a factor that in combination with the properties of the power cable, specifically the high-frequency attenuation and the length, determines the optimum bandwidth for PD detection [SSS01]. Since a PD pulse can have a bandwidth of several hundred megahertz but the power cable act as a low-pass filter, a practical approach using a bandwidth of approximately

20 MHz is sometimes proposed [BPW96]. However, there are several reports of PD detection using a high-frequency sensor *e.g.*, [AS98, ZYJZ05] that has a bandwidth of approximately 100 MHz. Commercial PD diagnostic equipment is mostly designed with a bandwidth of approximately 10 MHz.

Sensors used for PD detection can be divided into capacitive or inductive sensors, measuring the voltage or current on the power cable, respectively. In addition, the sensor position can be varied [WVWS03] to obtain the best possible signals. The general inductive sensor can either be a High Frequency Current Transformer (HFCT) or a Rogowski Coil (RC). The two differs in the core material of the sensor, HFCT is usually based on a splitted ferrite core while a RC has an air core. This distinction is not so strict and combinations of the two occurs [ZYJZ05]. The properties and physical limitations often decide which type of sensor that can be employed [WVWS03, DE04]. The choice of sensor depends also on the power system properties and the installation requirements. In [PSH⁺99] directional coupling sensors were mounted on both sides of a joint between two power cables. This enabled estimation of the direction of the PD pulse propagation.

The estimation of the direction from which a PD pulse arrives is an important part of a PD diagnostic system. Separation by direction provides the first identification step in a PD diagnostic system. However, due to the size and number of cables in a power network, PD pulses could travel far in the system and thereby be recorded at different positions where sensors are installed. Part VI and V of this thesis concerns the development of a Digital Directional Coupler, an instrument for wave splitting by digital means. The DDC is applied to separate forward and backward traveling waves. In Part IV, the properties of the DDC is investigated using the CRB as an assesment tool. Also, a laboratory experiment is conducted, resulting in an isolation and a directivity of approximately 40 dB over a frequency range of 20 – 80 MHz. In Part V, the DDC is implemented and utilized for PD measurements on a cross-linked polyethylene (XLPE) insulated power cable. The performance of the DDC was approximately 30 dB isolation and 25 dB directivity over a frequency range of approximately 50 MHz. The narrower frequency band in Part V compared to Part IV is due to the sensor design and selected to mitigate noise and interference.

In Fig. 3 is shown the site used to test the DDC. In the bottom figure is seen the low to medium voltage transformer, power cables and measurement equipment. In the top figure, the device used to penetrate the insulation of the power cable is depicted.



Figure 3: In the bottom figure is shown the site where the DDC is used for directional separation of partial discharge pulses and in the top figure, the device constructed to create partial discharges by penetrating the insulation of a power cable.

References

- [AD92] A. Atkinson and A. Doner. *Optimum Experiment Design*. Clarendon Press, Oxford, 1992.
- [AH06] T. Andersson and P. Händel. IEEE standard 1057, Cramér-Rao bound and the parsimony principle. *IEEE Transactions on Instrumentation and Measurement*, 55(1):44–53, 2006.
- [And98] P. M. Anderson. *Power System Protection*. Wiley-IEEE Press, 1998.
- [AS98] N. H. Ahmed and N. N. Srinivas. On-line partial discharge detection in cables. *IEEE Transactions on Dielectrics and Electrical Insulation*, 5(2):181–188, April 1998.
- [AW01] G. B. Arfken and H. J. Weber. *Mathematical Methods for Physicists*. Academic Press, New York, fifth edition, 2001.
- [Bal97] C. A. Balanis. *Antenna Theory*. John Wiley & Sons, New York, second edition, 1997.
- [BAM05] R. Boyer and K. Abed-Meraim. Damped and delayed sinusoidal model for transient signals. *IEEE Transactions on Signal Processing*, 53(5):1720–1730, 2005.
- [Bar02] R. Bartnikas. Partial discharges. their mechanism, detection and measurement. *IEEE Transactions on Dielectrics and Electrical Insulation*, 9(5):763–808, 2002.
- [BD00] S. Boggs and J. Densley. Fundamentals of partial discharge in the context of field cable testing. *IEEE Electrical Insulation Magazine*, 16(5):13–18, Sep./Okt. 2000.
- [BHN06] M. Belec, C. Hudon, and D. N. Nguyen. Statistical analysis of partial discharge data. In *Conference Record of the 2006 IEEE International Symposium on Electrical Insulation*, pages 122–125, 2006.
- [Bos94] A. van den Bos. A Cramér-Rao lower bound for complex parameters. *IEEE Transactions on Signal Processing*, 42(10):2859, 1994.

-
- [BPW96] S. A. Boggs, A. Pathak, and P. Walker. Partial discharge XXII: high frequency attenuation in shielded solid dielectric power cable and implications thereof for PD location. *IEEE Electrical Insulation Magazine*, 12(1):9–16, Jan./Feb. 1996.
- [CCM⁺02] A. Contin, A. Cavallini, G. C. Montanari, G. Pasini, and F. Puletti. Digital detection and fuzzy classification of partial discharge signals. *IEEE Transactions on Dielectrics and Electrical Insulation*, 9(3):335–348, 2002.
- [Chu48] L. J. Chu. Physical limitations of Omni-Directional antennas. *Appl. Phys.*, 19:1163–1175, December 1948.
- [CMF00] A. Contin, G.C. Montanari, and C. Ferraro. PD source recognition by weibull processing of pulse height distributions. *IEEE Transactions on Dielectrics and Electrical Insulation*, 7(1):48–58, 2000.
- [Col98] R. E. Collin. Minimum Q of small antennas. *J. Electro. Waves Applic.*, 12:1369–1393, 1998.
- [Col05] S. L. Collier. Fisher information for a complex gaussian random variable: beamforming applications for wave propagation in a random medium. *IEEE Transactions on Signal Processing*, 53(11):4236–4248, 2005.
- [CR64] R. E. Collin and S. Rothschild. Evaluation of antenna Q. *IEEE Transactions on Antennas and Propagation*, 12:23–27, January 1964.
- [Cra46] H. Cramér. Mathematical methods of statistics. *Princeton University Press*, 1946.
- [DE04] V. Dubickas and H. Edin. Couplers for on-line time domain reflectometry diagnostics of power cables. In *2004 Annual Report Conference on Electrical Insulation and Dielectric Phenomena*, pages 210–214, 2004.
- [DL05] M.I. Doroslovacki and E.G. Larsson. Nonuniform linear antenna arrays minimising Cramér-Rao bounds for joint estimation of single source range and direction of arrival. *IEE Proceedings - Radar, Sonar and Navigation*, 152(4):225–231, 2005.

- [DPG⁺98] S. Drabowitch, A. Papiernik, H. Griffiths, J. Encinas, and B. L. Smith. *Modern Antennas*. Chapman & Hall, 1998.
- [EN98] A. F. Emery and A. V. Nenarokomov. Optimal experiment design. *Measurement Science and Technology*, 9(6):864–876, 1998.
- [Fan50] R. M. Fano. Theoretical limitations on the broadband matching of arbitrary impedances. *Journal of the Franklin Institute*, 249(1,2):57–83 and 139–154, Jan/Feb 1950.
- [Fed72] V. Fedorov. *Theory of Optimal Experiments*. Academic Press, New York, 1972.
- [FHB⁺06] E. Fishler, A. Haimovich, R. S. Blum, Jr. L. J. Cimini, D. Chizhik, and R. A. Valenzuela. Spatial diversity in radar-models and detection performance. *IEEE Transactions on Signal Processing*, 54(3):823–838, 2006.
- [Fis22] R. A. Fisher. On the mathematical foundations of theoretical statistics. *Phil. Trans. Roy. Soc.*, 222:309, 1922.
- [FS06] M. Fenger and H. Sedding. Recent experiences with on-line PD testing of MV XLPE and EPR cable. In *Conference Record of the 2006 IEEE International Symposium on Electrical Insulation, 2006*, pages 42–45, 2006.
- [GB95] P. Von Glahn and R. J. Van Brunt. Continuous recording and stochastic analysis of PD. *IEEE Transactions on Dielectrics and Electrical Insulation*, 2(4):590–601, 1995.
- [GK92] E. Gulski and F. H. Kreuger. Computer-aided recognition of discharge sources. *IEEE Transactions on Electrical Insulation*, 27(1):82–92, 1992.
- [GN04] M. Gustafsson and S. Nordebo. On the spectral efficiency of a sphere. Technical Report LUTEDX/(TEAT-7127)/1–24/(2004), Lund Institute of Technology, Department of Electrosience, P.O. Box 118, S-211 00 Lund, Sweden, 2004.
- [GN06] M. Gustafsson and S. Nordebo. Characterization of MIMO antennas using spherical vector waves. *IEEE Transactions on Antennas and Propagation*, 54(9):2679–2682, 2006.

-
- [GSRK94] X. Guanghai, S. D. Silverstein, R. H. Roy, and T. Kailath. Beamspace ESPRIT. *IEEE Transactions on Signal Processing*, 42(2):349–356, 1994.
- [GSV⁺07] C. C. Gaudes, I. Santamaria, J. Via, E. Masgrau Masgrau Gomez, and T. Ses Paules. Robust array beamforming with sidelobe control using support vector machines. *IEEE Transactions on Signal Processing*, 55(2):574–584, 2007.
- [Han35] W. W. Hansen. A new type of expansion in radiation problems. *Physics Review*, 47:139–143, 1935.
- [Han88] J. E. Hansen, editor. *Spherical Near-Field Antenna Measurements*. Number 26 in IEE electromagnetic waves series. Peter Peregrinus Ltd., Stevenage, UK, 1988. ISBN: 0-86341-110-X.
- [Han97] T. B. Hansen. Formulation of spherical near-field scanning for electromagnetic fields in the time domain. *IEEE Transactions on Antennas and Propagation*, 45(4):620–630, 1997.
- [Har61] R. F. Harrington. *Time Harmonic Electromagnetic Fields*. McGraw-Hill, New York, 1961.
- [Hei99] C. Heitz. A generalized model for partial discharge processes based on a stochastic process approach. *Journal of Physics D: Applied Physics*, 32(9):1012–1023, 1999.
- [HN95] B. Hochwald and A. Nehorai. Polarimetric modeling and parameter estimation with applications to remote sensing. *IEEE Transactions on Signal Processing*, 43(8):1923–1935, August 1995.
- [HN96] B. Hochwald and A. Nehorai. Identifiability in array processing models with vector-sensor applications. *IEEE Transactions on Signal Processing*, 44:83–95, January 1996.
- [HN06] M. Hurtado and A. Nehorai. Optimal polarized waveform design for active target parameter estimation using electromagnetic vector sensors. In *2006 IEEE International Conference on Acoustics Speed and Signal Processing Proceedings*, volume 5, 2006.
- [HRs99] Z. A. Hussein and Y. Rahmat-samii. Application of cylindrical near-field measurement technique to the calibration of spaceborne

- radar antennas:. *IEEE Transactions on Geoscience and remote sensing*, 37(1):360–373, 1999.
- [HTN99] K-C Ho, K-C Tan, and A. Nehorai. Estimating directions of arrival of completely and incompletely polarized signals with electromagnetic vector sensors. *IEEE Transactions on Signal Processing*, 47(10):2845–2852, October 1999.
- [HTT97] K-C Ho, K-C Tan, and B. T. G. Tan. Efficient method for estimating directions-of-arrival of partially polarized signals with electromagnetic vector sensors. *IEEE Transactions on Signal Processing*, 45(10):2485–2498, October 1997.
- [HTT98] K-C Ho, K-C Tan, and B. T. G. Tan. Linear dependence of steering vectors associated with tripole arrays. *IEEE Transactions on Antennas and Propagation*, 46(11):1705–1711, November 1998.
- [Jac75] J. D. Jackson. *Classical Electrodynamics*. John Wiley & Sons, New York, second edition, 1975.
- [JW04] M.A. Jensen and J.W. Wallace. A review of antennas and propagation for MIMO wireless communications. *IEEE Transactions on Antennas and Propagation*, 52(11):2810–2824, 2004.
- [JW05] M.A. Jensen and J.W. Wallace. Antenna-independent capacity bound of electromagnetic channels. In *IEEE Antennas and Propagation Society International Symposium*, volume 2A, pages 317–320, 2005.
- [Kay93a] S. M. Kay. *Fundamentals of Statistical Signal Processing, Estimation Theory*. Prentice-Hall, Inc., NJ, 1993.
- [Kay93b] S. M. Kay. *Fundamentals of Statistical Signal Processing, Estimation Theory*. Prentice-Hall, Inc., Upper Saddle River, NJ, 1993.
- [KG05] A. Kyprianou and G. E. Georghiou. Wavelet packet denoising for on-line partial discharge detection in high voltage systems. In *Mediterranean Conference on Control and Automation*, pages 1184–1189, 2005.
- [Kri99] G. Kristensson. *Spridningsteori med antenntillämpningar*. Studentlitteratur, 1999.

-
- [KSS94] A. Kangas, P. Stoica, and T. Söderstrom. Finite sample and modelling error effects on ESPRIT and MUSIC direction estimators. *IEE Proceedings - Radar, Sonar and Navigation*, 141(5):249–255, 1994.
- [KV96] H. Krim and M. Viberg. Two decades of array signal processing research: the parametric approach. *IEEE Signal Processing Magazine*, 13(4):67–94, July 1996.
- [Lai05] T. Laitinen. *Advanced Spherical Antenna Measurements*. Ph.d. thesis, Helsinki University of Technology, Finland, 2005.
- [Lar80] Larsen1980. *Probe-corrected Spherical Near-field Antenna Measurements*. Ph.d. thesis, Technical University of Denmark, Denmark, 1980.
- [Li93] J. Li. Direction and polarization estimation using arrays with small loops and short dipoles. *IEEE Transactions on Antennas and Propagation*, 41(3):379–387, March 1993.
- [LPB06] T. Laitinen, S. Pivnenko, and O. Breinbjerg. Application of the iterative probe correction technique for a high-order probe in spherical near-field antenna measurements. *IEEE Antennas and Propagation Magazine*, 48(4):179–185, 2006.
- [LPP03] V. Latva-Pukkila and P. Pakonen. Disturbances occurring in on-site partial discharge measurements. In *Conference record of Nordic Insulation Symposium (NORDIS)*, pages 11–19, 2003.
- [LS94] J. Li and P. Stoica. Efficient parameter estimation of partially polarized electromagnetic waves. *IEEE Transactions on Signal Processing*, 42(11):3114–3125, November 1994.
- [LW90] H. B. Lee and M. S. Wengrovitz. Resolution threshold of beamspace MUSIC for two closely spaced emitters. *Acoustics, Speech and Signal Processing*, 38(9):1545–1559, 1990.
- [Mas00] M. Mashikian. Partial discharge location as a diagnostics tool for power cables. In *Proceedings of the IEEE Power Engineering Society Winter Meeting*, volume 3, pages 1604–1608, 2000.

- [MD99] E. A. Marengo and A. J. Devaney. The inverse source problem of electromagnetics: linear inversion formulation and minimum energy solution. *IEEE Transactions on Antennas and Propagation*, 47(2):410–412, 1999.
- [MDG04] E. A. Marengo, A. J. Devaney, and F. K. Gruber. Inverse source problem with reactive power constraint. *IEEE Transactions on Antennas and Propagation*, 52(6):1586–1595, 2004.
- [Mil74] K. S. Miller. *Complex Stochastic Processes*. Addison–Wesley Publishing Company, Inc., 1974.
- [Mon06] C. G. Montanari. Partial discharge measurements: Becoming a fundamental tool for quality control and a risk assessment of electrical systems? In *Conference record of 2006 IEEE International Symposium on Electrical Insulation*, pages 281–285, 2006.
- [NG04] S. Nordebo and M. Gustafsson. Fundamental limitations for DOA estimation by a sphere. Technical Report LUTEDX/(TEAT-7128)/1–26/(2004), Lund Institute of Technology, Department of Electrosience, P.O. Box 118, S-211 00 Lund, Sweden, 2004.
- [NG05a] S. Nordebo and M. Gustafsson. Multichannel broadband Fano theory for arbitrary lossless antennas with applications in DOA estimation. In *2005 IEEE International Conference on Acoustics, Speech, and Signal Processing*. IEEE Signal Processing Society, 2005.
- [NG05b] S. Nordebo and M. Gustafsson. Multichannel broadband fano theory with applications in array signal processing. *AIP Conference Proceedings*, 750(1):288–298, 2005.
- [NG06] S. Nordebo and M. Gustafsson. Statistical signal analysis for the inverse source problem of electromagnetics. *IEEE Transactions on Signal Processing*, 54(6):2357–2362, 2006.
- [NGP07] S. Nordebo, M. Gustafsson, and K. Persson. Sensitivity analysis for antenna near-field imaging. *IEEE Transactions on Signal Processing*, 55(1):94–102, 2007.
- [NP94] A. Nehorai and E. Paldi. Vector-sensor array processing for electromagnetic source localization. *IEEE Transactions on Signal Processing*, 42(2):376–398, February 1994.

-
- [OM05] U. Oktel and R. L. Moses. A bayesian approach to array geometry design. *IEEE Transactions on Signal Processing*, 53(5):1919–1923, 2005.
- [PRWP05] A. R. Pineda, S. B. Reeder, Z. Wen, and N. J. Pelc. Cramér-Rao bounds for three-point decomposition of water and fat. *Magnetic Resonance in Medicine*, 54(3):625–635, 2005.
- [PSH⁺99] D. Pommerenke, T. Strehl, R. Heinrich, W. Kalkner, F. Schmidt, and W. Weissenberg. Discrimination between interal PD and other pulses using directional coupling sensors on HV cable systems. *IEEE Transactions on Dielectrics and Electrical Insulation*, 6(6):814–824, Dec. 1999.
- [QQS05] Y. Qiaowei, C. Qiang, and K. Sawaya. Accurate DOA estimation using array antenna with arbitrary geometry. *IEEE Transactions on Antennas and Propagation*, 53(4):1352–1358, 2005.
- [Rao45] C. R. Rao. Information and accuracy attainable in the estimation of statistical parameters. *Bull. Calcutta Math. Soc.*, 37:81–91, 1945.
- [RH89] B. D. Rao and K. V. S. Hari. Performance analysis of Root-MUSIC. *Acoustics, Speech and Signal Processing*, 37(12):1939–1949, 1989.
- [RK89] R. Roy and T. Kailath. ESPRIT-estimation of signal parameters via rotational invariance techniques. *Acoustics, Speech and Signal Processing*, 37(7):984–995, 1989.
- [SB02] M. M. A. Salama and R. Bartnikas. Determination of neural-network topology for partial discharge pulse pattern recognition. *IEEE Transactions on Neural Networks*, 13(2):446–456, 2002.
- [Sch91] L. L. Scharf. *Statistical Signal Processing: Detection, Estimation and Time Series Analysis*. Reading, MA: Addison-Wesley, 1991.
- [SHV91] E. F. Steennis, E. Hetzel, and C. W. J. Verhoeven. Diagnostic medium voltage cable test at 0.1 Hz. In *Proceedings of the 3rd IEEE International Conference on Insulated Power Cables*, pages 408–414, 1991.

-
- [SJL97] P. Stoica, A. Jakobsson, and J. Li. Cisoid parameter estimation in the colored noise case: asymptotic Cramér-Rao bound, maximum likelihood, and nonlinear least-squares. *IEEE Transactions on Signal Processing*, 45(8):2048–2059, 1997.
- [SM90] P. Stoica and R.L. Moses. On biased estimators and the unbiased Cramér-Rao lower bound. *Signal Processing*, 21(4):349–350, 1990.
- [SM97] P. Stoica and R. L. Moses. *Introduction to Spectral Analysis*. Prentice-Hall, Englewood Cliffs, NJ, 1997.
- [SMFS89] P. Stoica, R. L. Moses, B. Friedlander, and T. Söderstrom. Maximum likelihood estimation of the parameters of multiple sinusoids from noisy measurements. *Acoustics, Speech and Signal Processing*, 37(3):378–392, 1989.
- [Smi05] S. T. Smith. Statistical resolution limits and the complexified Cramér-Rao bound. *IEEE Transactions on Signal Processing*, 53(5):1597–1609, 2005.
- [SN90a] P. Stoica and A. Nehorai. MUSIC, maximum likelihood, and Cramér-Rao bound: further results and comparisons. *IEEE Transactions on Acoustics, Speech, and Signal Processing*, 38(12):2140–2150, December 1990.
- [SN90b] P. Stoica and A. Nehorai. Performance study of conditional and unconditional direction-of-arrival estimation. *IEEE Transactions on Acoustics, Speech, and Signal Processing*, 38(10):1783–1795, 1990.
- [SO96] P. Stoica and B. Ottersten. The evil of superefficiency. *Signal Processing*, 55(1):133–136, 1996.
- [SS97] P. Stoica and T. Söderstrom. Eigenelement statistics of sample covariance matrix in the correlated data case. *Digital Signal Processing*, 7(2):136–143, 1997.
- [SSB05] N.C. Sahoo, M. M. A. Salama, and R. Bartnikas. Trends in partial discharge pattern classification: a survey. *IEEE Transactions on Dielectrics and Electrical Insulation*, 12(2):248–264, 2005.

-
- [SSS00] I. Shim, J. J. Soraghan, and W. H. Siew. Digital signal processing applied to the detection of partial discharge: an overview. *IEEE Electrical Insulation Magazine*, 16(3):6–12, May/June 2000.
- [SSS01] I. Shim, J. J. Soraghan, and W. H. Siew. Detection of PD utilizing digital signal processing methods part 3: open loop noise reduction. *IEEE Electrical Insulation Magazine*, 17(1):6–13, Jan./Feb. 2001.
- [Sto05] G. C. Stone. Partial discharge diagnostics and electrical equipment insulation condition assessment. *IEEE Transactions on Dielectrics and Electrical Insulation*, 12(5):891–904, 2005.
- [SV93] A. Swindlehurst and M. Viberg. Subspace fitting with diversely polarized antenna arrays. *IEEE Transactions on Antennas and Propagation*, 41(12):1687–1694, December 1993.
- [Thi07] B. Thidé. *Electromagnetic Field Theory*. Upsilon Books, 2007. www.plasma.uu.se/CED/book.
- [Tre01] H. L. Van Trees. *Detection, Estimation and Modulation Theory*. John Wiley & Sons, Inc., New York, 2001.
- [Tre02] H. L. Van Trees. *Optimum Array Processing*. John Wiley & Sons, Inc., New York, 2002.
- [TSR04] J. Tabrikian, R. Shavit, and D. Rahamim. An efficient vector sensor configuration for source localization. *IEEE Signal Processing Letters*, 11(8):690–693, 2004.
- [VBA03] R. Vaughan and J. Bach Andersen. *Channels, Propagation and Antennas for Mobile Communications*. Institution of Electrical Engineers, 2003.
- [VBW98] L. Vandenberghe, S. Boyd, and S. Wu. Determinant maximization with linear matrix inequality constraints. *SIAM Journal on Matrix Analysis and Applications*, 19(2):499–534, 1998.
- [Vee05] J. Veen. *On-line signal analysis of partial discharges in medium-voltage power cables*. Ph.d. thesis, Eindhoven University of Technology, the Netherlands, 2005.

- [VSO97] M. Viberg, P. Stoica, and B. Ottersten. Maximum likelihood array processing in spatially correlated noise fields using parameterized signals. *IEEE Transactions on Signal Processing*, 45(4):996–1004, April 1997.
- [VW03] J. Veen and P. C. J. M. van der Wielen. The application of matched filter to PD detection and localization. *IEEE Electrical Insulation Magazine*, 19(5):20–26, Sep./Okt. 2003.
- [WF91] A. J. Weiss and B. Friedlander. Performance analysis of diversely polarized antenna arrays. *IEEE Transactions on Signal Processing*, 39(7):1589–1603, July 1991.
- [WF93] A. J. Weiss and B. Friedlander. Maximum likelihood signal estimation for polarization sensitive arrays. *IEEE Transactions on Antennas and Propagation*, 41(7):918–925, July 1993.
- [WGF06] J. S. Welsh, G. C. Goodwin, and A. Feuer. Evaluation and comparison of robust optimal experiment design criteria. In *American Control Conference, 2006*, 2006.
- [WLZ04] K. T. Wong, L. Li, and M. D. Zoltowski. Root-MUSIC-based direction-finding and polarization estimation using diversely polarized possibly collocated antennas. *IEEE Antennas & Wireless Propagation Letters*, 3(8):129–132, 2004.
- [Won01] K. T. Wong. Direction finding/polarization estimation – dipole and/or loop triad(s). *IEEE Transactions on Aerospace and Electronic Systems*, 37(2):679–684, April 2001.
- [WVWS03] P. C. J. M. van der Wielen, J. Veen, P. A. A. F. Wuters, and E. F. Steennis. Sensors for on-line PD detection in MV power cables and their location in substations. In *Proceedings of 7th International Conference on Properties and Applications of Dielectric Materials*, pages 215–219, 2003.
- [WZ00] K. T. Wong and M. D. Zoltowski. Closed-form direction finding and polarization estimation with arbitrarily spaced electromagnetic vector-sensors at unknown locations. *IEEE Transactions on Antennas and Propagation*, 48(5):671–681, May 2000.

-
- [XC04] L. Xuejun and L. Carin. Application of the theory of optimal experiments to adaptive electromagnetic-induction sensing of buried targets. *IEEE Transactions on Pattern Analysis and Machine Intelligence*, 26(08):961–972, 2004.
- [YD05] E. Yilmaz and E. Dilaveroglu. Asymptotic worst and best case Cramér-Rao bounds for estimation of parameters of low-frequency damped sinusoid. *Electronics Letters*, 41(2):73–74, 2005.
- [ZQC06] Y. Zhou, Y. Qin, and P. Chappell. Cost-effective on-line partial discharge measurements for cables. *IEEE Electrical Insulation Magazine*, 22(2):31–38, 2006.
- [ZYJZ05] J. Zhu, L. Yang, J. Jia, and Q. Zhang. The design of rogowski coil with wide band using for partial discharge measurements. In *Proceedings of 2005 International Symposium on Electrical Insulation*, pages 518–521, 2005.

Thesis summary

Part I - A Generic Electromagnetic Model for DOA Estimation Using Arbitrary Multiport Antennas

A generic model of multiport antennas based on spherical vector waves is developed. This constitutes a general framework for modelling a general multiport antenna. From measurement or numerical calculations of the antenna far-field amplitude, a complete description can be obtained through a numerical method based on the FFT and properties of the spherical vector waves.

All properties of the modelled antenna are included *e.g.*, mutual coupling is accounted for, which if not included can cause deterioration in the result of applications that are sensitive to errors in the antenna model, *e.g.*, beam-forming and DOA estimation using super-resolution techniques.

In the context of DOA estimation, increasing the resolution of DOA estimation techniques are easily done by computations of the array manifold on a dense spatial grid, no further measurements of the antenna properties are required. Illustrations of DOA estimation using a Tetrahedron array are included.

Part II - Fundamental Limitations for DOA and Polarization Estimation with Applications in Array Signal Processing

In Part II, based on the generic electromagnetic model of part I, fundamental physical limitations associated with DOA and polarization estimation using arbitrary antennas or antenna arrays are analysed. The Cramér–Rao bound (CRB) for DOA and polarization estimation is provided for any real multiport antenna.

The spherical vector waves and their associated equivalent circuits and Q factor approximations are used together with the broadband Fano theory as a general framework for analysing electrically small multiport antennas. The CRB is given in terms of the transmission matrix, the spherical vector harmonics and its spatial derivatives.

A principal parameter analysis using the singular value decomposition of the Fisher information matrix is employed to evaluate the performance of an ideal Tripole antenna array with respect to its ability to estimate the state of polarization of a partially polarized plane wave coming from a given direc-

tion. As a second example of an arbitrary multiport antenna, the non-ideal Tetrahedron array (including mutual coupling) is considered in the context of DOA estimation.

Part III - On the Design of Optimal Cylindrical Antenna Near-Field Measurements

A cylindrical antenna near-field measurement setup is considered based on the theory of optimal experiment design. Two separate semi-definite optimization formulations are considered and based on the Fisher information matrix of the multipole coefficients in the spherical vector wave expansion of the electrical field. The optimal measurement points are obtained from the solution of the two separate optimization formulations, respectively.

The inverse source problem *i.e.*, the estimation of the multipole coefficients is studied using equidistant measurement points and optimal measurement points. A singular value analysis is used to interpret the result of the optimization, the estimation of the multipole coefficients and the corresponding electrical field.

The first optimization formulation provides close to a minimum number of measurement points sufficient to solve the inverse problem. The second optimization formulation introduce more measurement points. Numerical examples are provided to study the results and include an extension to a cylindrical measurement.

Part IV - Statistical Analysis of a Digital Directional Coupler for Transmission Line Measurements

A Digital Directional Coupler (DDC) that separates forward and backward propagating waves on a transmission line is presented. The application is direction separation of signals propagating on a transmission line. The DDC is based on two independent wide-band measurements of voltage and current and a frequency domain digital wave splitting using the FFT.

To account for imperfections *e.g.*, the sensors might have a non-flat frequency response; a practical procedure is described for calibration of the digital wave splitter. The CRB is used as a statistical tool to analyse the properties of the DDC. Important parameters are identified *e.g.*, the signal-to-noise ratio in the calibration procedure, the characteristic impedance of the transmission line and the frequency transfer functions of the voltage and current sensors.

An experiment was conducted where a DDC is implemented to operate over an appreciable bandwidth using simple and low cost sensors. The transmission line was a standard coaxial antenna cable and the resulting directivity (ratio between coupling and cross-coupling) was approximately 37 dB over a bandwidth of 20–80 MHz.

Part V - Partial Discharge Measurement Using a Digital Directional Coupler

First, the Digital Directional Coupler that separates forward and backward propagating waves on a transmission line is described. Then, experiments using medium voltage equipment in a power distribution station and a DDC implemented to conduct wave splitting on a cross-linked polyethylene (XLPE) insulated power cable are described.

Using a set of power cables designed for different voltage levels, a multi-reflection environment is obtained. A needle is used to penetrate the insulation of a power cable, providing some control to the amount and to the properties of the resulting partial discharges.

The isolation and coupling of the DDC were determined to 27 dB and 5 dB, respectively; over a bandwidth of approximately 50 MHz. Measurements displays the ability of DDC to separate partial discharge pulses based on the direction of travel even for pulses hardly visible in the sensor signals.

PART I

**A Generic Electromagnetic
Model for DOA Estimation
Using Arbitrary Multiport
Antennas**

Part I is published as:

J. Lundbäck, S. Nordebo and M. Gustafsson, "A Generic Electromagnetic Model for DOA Estimation Using Arbitrary Multiport Antennas", In *proceedings of the IEEE International Symposium on Antennas and Propagation*, pp. 2549-2552, Albuquerque, USA, July 2006.

A Generic Electromagnetic Model for DOA Estimation Using Arbitrary Multiport Antennas

J. Lundbäck, S. Nordebo and M. Gustafsson

Abstract

During the last decades electromagnetic vector sensors have been extensively investigated, especially since the properties of electromagnetic wave propagation are incorporated in the statistical signal estimation techniques used for direction finding and polarization estimation in sensor array processing, see *e.g.*, [WLZ04]. In this paper, we utilize a generic electromagnetic model for arbitrary multiport antennas *e.g.*, vector sensors applied in DOA estimation, which was exploited in [NGL06] for statistical analysis of DOA and polarization estimation. By utilizing the spherical vector wave expansion of the electromagnetic field to completely characterize the multiport antennas a general framework for modelling an antenna configuration based on measurements or computations including *e.g.*, mutual coupling is obtained. The array manifold can easily be expanded over a dense spatial grid to enable high-resolution DOA estimation without demanding further measurements of the antenna characteristics.

1 An Electromagnetic Model for Arbitrary Multiport Antennas

Consider an arbitrary multiport antenna. Let (r, θ, ϕ) denote the spherical coordinates, $k = \frac{\omega}{c} = \frac{2\pi}{\lambda}$ the wave number, $\omega = 2\pi f$ the angular frequency, λ the wave length and c and η the speed of light and the wave impedance of free space, respectively. Assume that the antenna is contained inside a sphere of radius $r = a$, and let $e^{i\omega t}$ be the time convention. Based on a *spherical vector waves expansion* [Han88] of the transmitted electric field, $\mathbf{E}(\mathbf{r})$, it can be shown that in the *far-field* when $r \rightarrow \infty$, $\mathbf{E}(\mathbf{r}) = \frac{e^{-ikr}}{kr} \mathbf{F}(\hat{\mathbf{r}})$ where $\mathbf{F}(\hat{\mathbf{r}})$ is

the *far-field amplitude* given by

$$\mathbf{F}(\hat{\mathbf{r}}) = \sum_{l=1}^L \sum_{m=-l}^l \sum_{\tau=1}^2 \mathbf{i}^{l+2-\tau} f_{\tau ml} \mathbf{A}_{\tau ml}(\hat{\mathbf{r}}). \quad (1)$$

In (1) $\mathbf{A}_{\tau ml}(\hat{\mathbf{r}})$ are the *spherical vector harmonics* [Han88] and $f_{\tau ml}$ are the expansion coefficients or multipole moments. Here $\tau = 1$ corresponds to a transversal electric (TE) wave and $\tau = 2$ corresponds to a transversal magnetic (TM) wave. The other indices are $l = 1, 2, \dots, L$ and $m = -l, \dots, l$ where l denotes the *order* of that mode. The maximum order L is determined by the electrical size and bandwidth of the antenna *cf.*, [Han88, NGL06]. Furthermore, it can also be shown that the total power P_s transmitted by the antenna is given by $P_s = \frac{1}{2\eta k^2} \sum_{l=1}^L \sum_{m=-l}^l \sum_{\tau=1}^2 |f_{\tau ml}|^2$.

Given that the far-field amplitude $\mathbf{F}(\hat{\mathbf{r}})$ of the antenna is available through some numerical or analytical means and utilizing orthonormality of the spherical vector harmonics [Han88], the multipoles can be calculated from the projections

$$f_{\tau ml} = \mathbf{i}^{-l-2+\tau} \int \mathbf{A}_{\tau ml}^*(\hat{\mathbf{r}}) \cdot \mathbf{F}(\hat{\mathbf{r}}) d\Omega \quad (2)$$

where $*$ denote the conjugate operation.

When calculating the multipoles (2) from spherical data it is convenient to employ the Fast Fourier Transform (FFT). Let $F^p(\hat{\mathbf{r}})$ denote the spherical components of the far-field amplitude $\mathbf{F}(\hat{\mathbf{r}})$ where $p = \theta, \phi$. Let $\tilde{F}_m^p(\theta)$ denote the Discrete Fourier transform (DFT) of the calculated (or measured) spherical components along the azimuthal coordinate ϕ such that

$$F^p(\hat{\mathbf{r}}) = \frac{1}{M} \sum_{m=-M/2+1}^{M/2} \tilde{F}_m^p(\theta) e^{\mathbf{i}m\phi} \quad (3)$$

where M is the number of azimuthal points and the size of the DFT, $M/2 > L$ and L is assumed to be sufficiently large so that the spatial aliasing in (3) can be neglected. The spherical vector harmonics $\mathbf{A}_{\tau ml}(\hat{\mathbf{r}})$ and their corresponding DFT's $\tilde{\mathbf{A}}_{\tau ml}(\theta)$ are defined so that $\mathbf{A}_{\tau ml}(\hat{\mathbf{r}}) = \tilde{\mathbf{A}}_{\tau ml}(\theta) e^{\mathbf{i}m\phi}$, see also [NGL06]. Hence, by the orthogonality of the periodic Fourier basis $e^{\mathbf{i}m\phi}$, the double integral in (2) can now be calculated conveniently by the single integrals

$$f_{\tau ml} = \frac{2\pi}{M} \mathbf{i}^{-l-2+\tau} \sum_{p=\theta, \phi} \int_0^\pi \tilde{\mathbf{A}}_{\tau ml}^{p*}(\theta) \cdot \tilde{F}_m^p(\theta) \sin \theta d\theta \quad (4)$$

where $\tilde{A}_{\tau ml}^p(\theta)$ denotes the spherical components of $\tilde{\mathbf{A}}_{\tau ml}(\theta)$.

Consider an arbitrary multiport antenna consisting of N ports. Let x_i^+ and x_i^- denote the corresponding incident and reflected voltages at the antenna waveguide connections for $i = 1, \dots, N$. These voltages are normalized so that the power delivered to a particular antenna port is $\frac{|x_i^+|^2}{2Z_g}$ and the corresponding reflected power is $\frac{|x_i^-|^2}{2Z_g}$ where Z_g is the impedance of the propagating waveguide mode. On transmission from the input terminals with incident voltage waves x_i^+ , the transmitted wave field f_α is given by

$$\begin{bmatrix} f_\alpha \\ k \end{bmatrix} = \mathbf{T} \mathbf{x}^+ \sqrt{\frac{\eta}{Z_g}} \quad (5)$$

where the multi-index $\alpha = (\tau, m, l)$ is used to simplify the notation, $\mathbf{T} = [T_{\alpha i}]$ is the properly scaled transmission matrix which maps the vector of incident voltages $\mathbf{x}^+ = [x_i^+]$ to propagated multipoles f_α . The $2L(L+2) \times N$ transmission matrix \mathbf{T} is obtained one column at a time by calculating the far-field and the corresponding multipoles (2) with the corresponding input connections energized one at a time. Now, considering one single incident wave x_i^+ , the antenna reciprocity theorem [DPG⁺98] yields

$$x_i^- x_i^+ = -i \frac{\lambda^2}{2\pi} \frac{Z_g}{\eta} \mathbf{F}(\hat{\mathbf{k}}_0) \cdot \mathbf{E}_0 \quad (6)$$

where \mathbf{E}_0 is the complex vector amplitude of a plane wave $\mathbf{E}_0 e^{-ik\hat{\mathbf{k}}_0 \cdot \mathbf{r}}$ coming from direction $\hat{\mathbf{k}}_0$ and x_i^- the corresponding received signal. Further, $\mathbf{F}(\hat{\mathbf{r}})$ is the far-field amplitude corresponding to the transmitted signal x_i^+ . Hence, by using (1) the received vector signal is obtained from the reciprocity theorem (6) as

$$\mathbf{x}^- = \sqrt{\frac{Z_g}{\eta}} \lambda \mathbf{R} \mathbf{A} \mathbf{E} \quad (7)$$

where $\mathbf{R} = \mathbf{T}^T$, \mathbf{A} is an $2L(L+2) \times 2$ matrix where each column corresponds to the spherical components of the spherical vector harmonics $i^{l+1-\tau} \mathbf{A}_\alpha(\hat{\mathbf{k}}_0)$, and \mathbf{E} is an 2×1 vector containing the corresponding signal components of the electric field \mathbf{E}_0 .

2 DOA Estimation Using a Multiport Antenna

Based on (7) we employ here the simple snapshot signal model [Tre02]

$$\mathbf{x} = \sqrt{\frac{Z_g}{\eta}} \lambda \mathbf{R} \mathbf{A} \mathbf{E} s + \mathbf{n}, \quad (8)$$

where the signal s and sensor noise \mathbf{n} are modelled as uncorrelated zero mean complex Gaussian variables with signal variance σ_s^2 , noise variance σ_n^2 and noise covariance matrix $\sigma_n^2 \mathbf{I}$. The received electric field is assumed to have unit magnitude $|\mathbf{E}_0| = 1$ and completely polarized. Hence,

$\mathbf{E} = [\cos \alpha \cos \beta + i \sin \alpha \sin \beta \cos \alpha \sin \beta - i \sin \alpha \cos \beta]^T$ where $-\pi/4 \leq \alpha \leq \pi/4$ and $0 \leq \beta \leq \pi$ are angular polarization parameters. Define the signal-to-noise ratio (SNR) as $\text{SNR} = \frac{\sigma_s^2 Z_g \lambda^2}{\sigma_n^2 \eta}$, the signal covariance matrix is given by

$$\mathbf{C}_{\mathbf{x}\mathbf{x}} = \sigma_n^2 (\text{SNR} \mathbf{R} \mathbf{A} \mathbf{E} \mathbf{E}^H \mathbf{A}^H \mathbf{R}^H + \mathbf{I}). \quad (9)$$

Here, we employ Capon and MUSIC, see e.g. [Tre02], two well known high-resolution techniques for DOA estimation where the corresponding spatial spectrum functions are given by

$$P_C(\theta, \phi) = \frac{1}{\lambda_{\min} \{ \mathbf{A}^H(\theta, \phi) \mathbf{R}^H \mathbf{C}_{\mathbf{x}\mathbf{x}}^{-1} \mathbf{R} \mathbf{A}(\theta, \phi) \}} \quad (10)$$

and

$$P_M(\theta, \phi) = \frac{1}{\lambda_{\min} \{ \mathbf{A}^H(\theta, \phi) \mathbf{R}^H \mathbf{Q}_n \mathbf{Q}_n^H \mathbf{R} \mathbf{A}(\theta, \phi) \}}, \quad (11)$$

respectively, where \mathbf{Q}_n is the $N \times (N - 1)$ noise subspace eigenvector matrix obtained from the eigenvalue decomposition of $\mathbf{C}_{\mathbf{x}\mathbf{x}} = \mathbf{Q} \mathbf{\Lambda} \mathbf{Q}^H$ and $\lambda_{\min} \{ \cdot \}$ denotes the minimum eigenvalue of the enclosed matrix. With reference to (10) and (11), it is observed that in order to increase the sampling density of the spatial spectrums we simply compute $\mathbf{A}(\theta, \phi)$ on a more dense grid. No further measurements of the antenna properties are needed. When calculating $\mathbf{A}(\theta, \phi)$ the following formulas can be applied to decrease the computational demand,

$$\tilde{A}_{2ml}^\theta(\theta) = -\tilde{A}_{1ml}^\phi(\theta), \quad (12)$$

$$\tilde{A}_{2ml}^\phi(\theta) = \tilde{A}_{1ml}^\theta(\theta), \quad (13)$$

$$\tilde{A}_{1ml}^\theta(\tilde{\theta}) = (-1)^{l+m} \tilde{A}_{1ml}^\theta(\theta), \quad (14)$$

$$\tilde{A}_{1ml}^\phi(\tilde{\theta}) = (-1)^{l+m+1} \tilde{A}_{1ml}^\phi(\theta), \quad (15)$$

where $\tilde{\theta} = \pi - \theta$, $\pi/2 < \tilde{\theta} \leq \pi$. Defining $\Delta\theta$ and $\Delta\phi$ as the spatial resolution we also observe that $\mathbf{A}_{\tau ml}(\theta, \phi + \Delta\phi) = \mathbf{A}_{\tau ml}(\theta, \phi)e^{im\Delta\phi}$.

3 Numerical Examples

Consider a single tetrahedron antenna array consisting of six half-wave dipoles centred on and organized as the edges in a tetrahedron where the total length of one edge is one wave-length. Utilizing a Method of Moments based electromagnetic simulation software, to obtain the far-field amplitude $\mathbf{F}(\hat{\mathbf{r}})$ for 64×128 points of θ and ϕ , (a spatial grid of size 64×128) and following the method outlined in section 1 with $L = 10$ and $M = 128$ we obtain $\mathbf{R} = \mathbf{T}^T$ of size 240×6 . This enables DOA estimation over the complete 2D DOA-space but for computational simplicity we let $\theta \in [1 \ 40]$ and $\phi \in [1 \ 100]$. Let the DOA of s be $\theta = 10.5^\circ$, $\phi = 30.5^\circ$, $\alpha = 13^\circ$, $\beta = 7^\circ$ and $\text{SNR} = 40$ dB. Using (9) in (10) and (11), we obtain the normalized spatial spectrum in Fig. 1.

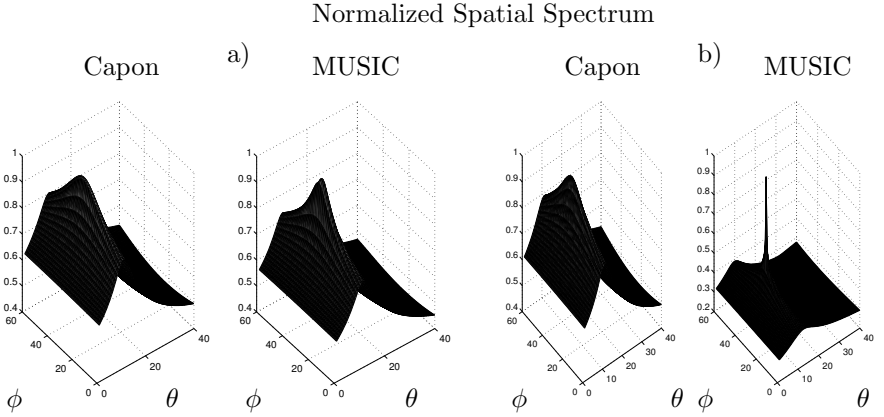


Figure 1: Normalized spatial spectrum function using a DOA-grid of a) 40×100 points and b) 80×200 points. The peak indicate a signal present.

In Fig. 1 a) the spatial grid is 40×100 points, $\Delta\theta = 1^\circ$ and $\Delta\phi = 1^\circ$, and in Fig Fig. 1 b) the spatial grid is 80×200 points, $\Delta\theta = 0.5^\circ$ and $\Delta\phi = 0.5^\circ$. The accuracy is improved, especially for MUSIC, since the computations of $\mathbf{A}(\theta, \phi)$ over a more dense grid includes the calculation of the response vector corresponding to the incoming signal.

Let $\tilde{\mathbf{R}} = \tilde{\mathbf{T}}^T$ be the transmission matrix obtained by modelling one dipole at a time, a simplification where the antenna elements are assumed to have no interaction. We can thereafter compare the results of the DOA estimation when $\tilde{\mathbf{R}}$ is used in (10) and (11) instead of \mathbf{R} . In Fig. 2 a), the spatial spectrum estimate using \mathbf{R} is depicted and in Fig. 2 b) using $\tilde{\mathbf{R}}$. A poor result is seen when the antenna is modelled using the assumption that no mutual coupling exists between the antenna elements.

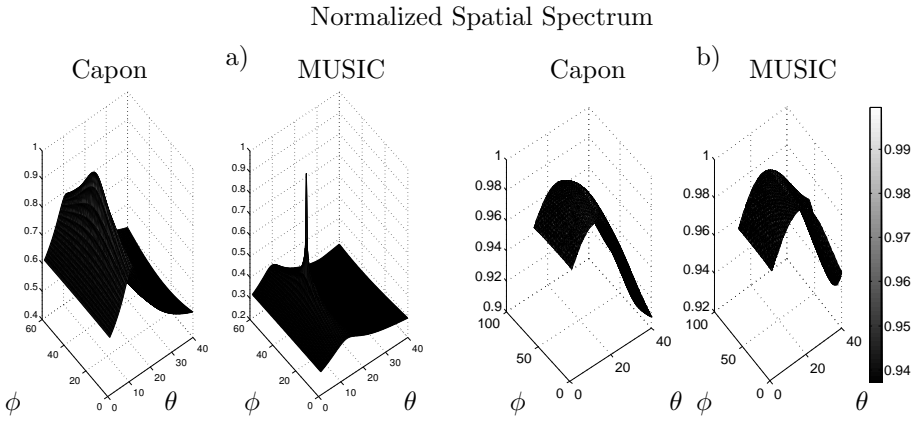


Figure 2: Normalized spatial spectrum function using a spatial grid of 80×200 points. In a) is the spatial spectrum estimate using the complete antenna model and in b), the spatial spectrum estimate for the case where each antenna element is modelled separately.

4 Conclusions

Using the generic model of multiport antennas based on spherical vector waves, we have obtained a general framework for modelling an arbitrary antenna system. Properties such as *e.g.*, mutual coupling are accounted for, which if not included can cause deterioration in the DOA estimation. Increasing the resolution of DOA estimation techniques is easily done by computations of the array manifold on a dense spatial grid, no further measurements

of the antenna properties are required.

References

- [DPG⁺98] S. Drabowitch, A. Papiernik, H. Griffiths, J. Encinas, and B. L. Smith. *Modern Antennas*. Chapman & Hall, 1998.
- [Han88] J. E. Hansen, editor. *Spherical Near-Field Antenna Measurements*. Number 26 in IEE electromagnetic waves series. Peter Peregrinus Ltd., Stevenage, UK, 1988. ISBN: 0-86341-110-X.
- [NGL06] S. Nordebo, M. Gustafsson, and J. Lundbäck. Fundamental limitations for DOA and polarization estimation with applications in array signal processing. *IEEE Transactions on Signal Processing*, 54(10):4055–4061, 2006.
- [Tre02] H. L. Van Trees. *Optimum Array Processing*. John Wiley & Sons, Inc., New York, 2002.
- [WLZ04] K. T. Wong, L. Li, and M. D. Zoltowski. Root-MUSIC-based direction-finding and polarization estimation using diversely polarized possibly collocated antennas. *IEEE Antennas & Wireless Propagation Letters*, 3(8):129–132, 2004.

PART II

Fundamental Limitations for DOA and Polarization Estimation with Applications in Array Signal Processing

Part II is published as:

S. Nordebo, M. Gustafsson and J. Lundbäck, "Fundamental Limitations for DOA and Polarization Estimation with Applications in Array Signal Processing", *IEEE Transactions on Signal Processing*, vol. 54, no. 10, pp. 4055-4061, October 2006.

Fundamental Limitations for DOA and Polarization Estimation with Applications in Array Signal Processing

S. Nordebo, M. Gustafsson and J. Lundbäck

Abstract

Using a generic electromagnetic model based on the spherical vector harmonics, we provide the Cramér–Rao lower bound (CRB) for DOA and polarization estimation with arbitrary multiport antennas. By reciprocity, the receiving multiport antenna is characterized in terms of the transmission matrix from incident voltage waves to multipole coefficients of the outgoing spherical vector waves. Explicit results of the CRB for the Gaussian case is given in terms of the transmission matrix, the spherical vector harmonics and its spatial derivatives. Numerical examples are included to illustrate the results.

1 Introduction

The Direction of Arrival (DOA) estimation using antenna arrays has been the topic for research in array and statistical signal processing over several decades and comprises now well developed modern techniques such as maximum likelihood and subspace methods, see *e.g.*, [KV96, VSO97, SN90] and the references therein. In recent years, there has been an increased interest in incorporating properties of electromagnetic wave propagation with the statistical signal estimation techniques used for sensor array processing and there are many papers dealing with direction finding and polarization estimation using electromagnetic vector sensors and diversely polarized antenna arrays, tripole arrays, etc., see *e.g.*, [RTS04, WZ00, Li93, SV93, HTT98, WF93, LS94, HN95, HTT97, HTN99, WLZ04, Won01]. However, most papers assume ideal electromagnetic vector sensors, and does not take into account the actual performance of a real antenna system, mutual coupling effects, etc., see *e.g.*,

[QQS05].

The classical theory of radiation Q uses spherical vector modes and equivalent circuits to analyze the properties of a hypothetical antenna inside a sphere, see *e.g.*, [Han81, CR64, McL96, GJQ00]. An antenna with a high Q factor has electromagnetic fields with large amounts of stored energy around it, and hence, typically low bandwidth and high losses [Han81]. From a radiation point of view, the high-order vector modes give the high-resolution aspects of the radiation pattern. As is well known, any attempt to accomplish supergain will result in high currents and near fields, thereby setting a practical limit to the gain available from an antenna of a given size, see also [Kar04]. The classical theory of broadband matching shows how much power that can be transmitted between a transmission line and a given load [Fan50], i.e. the antenna. Hence, by considering an antenna of a given size and bandwidth, together with the Q factors which are computable for each vector mode [CR64], the broadband Fano-theory [Fan50] can be used to estimate the maximum useful multipole order, and to calculate an upper bound for the transmission coefficient of any particular vector mode, see also [GN04, NG05, NG06]. However, when the antenna system is given, it is straightforward to assess the maximum useful multipole order simply by inspection of the multipole coefficients obtained from direct calculations.

In this paper, we demonstrate that the combination of statistical signal processing and electromagnetic theory yields simple and very useful tools for analyzing fundamental physical limitations associated with DOA and polarization estimation using arbitrary multiport antennas. In particular, we provide the Cramér–Rao bound (CRB) for DOA and polarization estimation with arbitrary multiport antennas by employing a generic electromagnetic model based on the spherical vector harmonics.

2 An Electromagnetic Signal Model for Arbitrary Multiport Receiving Antennas

In order to develop a general signal model for a receiving multiport antenna, or antenna array we start by considering the electromagnetic fields associated with arbitrary antennas in the transmit mode, and then apply the reciprocity theorem to obtain the properties of the corresponding antennas in the receive mode.

Consider an arbitrary multiport antenna in the transmit mode. Let (r, θ, ϕ)

denote the spherical coordinates, $k = \frac{\omega}{c} = \frac{2\pi}{\lambda}$ the wave number, $\omega = 2\pi f$ the angular frequency, λ the wave length and c and η the speed of light and the wave impedance of free space, respectively. Assume that the antenna is contained inside a sphere of radius $r = a$, and let $e^{i\omega t}$ be the time convention. The transmitted electric field, $\mathbf{E}(\mathbf{r})$, can then be expanded in *outgoing spherical vector waves* $\mathbf{u}_{\tau ml}(k\mathbf{r})$ for $r > a$ as [AW01, Jac75, Han88]

$$\mathbf{E}(\mathbf{r}) = \sum_{l=1}^L \sum_{m=-l}^l \sum_{\tau=1}^2 f_{\tau ml} \mathbf{u}_{\tau ml}(k\mathbf{r}) \quad (1)$$

where $f_{\tau ml}$ are the multipole coefficients. Here $\tau = 1$ corresponds to a transversal electric (TE) wave and $\tau = 2$ corresponds to a transversal magnetic (TM) wave. The other indices are $l = 1, 2, \dots, L$ and $m = -l, \dots, l$ where l denotes the *order* of that mode. For further details about the spherical vector mode representation we refer to the appendix and [AW01, Jac75, Han88].

In principle, the summation in (1) is infinite ($L = \infty$). However, for all practical purposes the maximum useful order L of any real antenna system is finite and can be estimated as described in *e.g.*, [CR64, GN04, NG05, NG06]. Hence, by considering a hypothetical mode-coupled antenna inserted inside a sphere of radius a , a given electrical size ka , fractional bandwidth B (normalized to the center frequency), and the Q -factors which are computable for each mode order l [CR64], the Fano-theory [Fan50] can be used to calculate the following upper bound for the transmission coefficient t_l for a particular mode, *cf.*, *e.g.*, [Fan50, GN04, NG05]

$$|t_l| \leq \sqrt{1 - e^{-\frac{2\pi}{Q_l} \frac{1-B^2/4}{B}}}. \quad (2)$$

However, when the antenna system is given, it is straightforward to assess L simply by inspection of the multipole coefficients obtained from direct calculations as described below.

It can be shown that in the *far-field* when $r \rightarrow \infty$, the electric field is given by $\mathbf{E}(\mathbf{r}) = \frac{e^{-ikr}}{kr} \mathbf{F}(\hat{\mathbf{r}})$ where $\mathbf{F}(\hat{\mathbf{r}})$ is the *far-field amplitude* given by

$$\mathbf{F}(\hat{\mathbf{r}}) = \sum_{l=1}^L \sum_{m=-l}^l \sum_{\tau=1}^2 i^{l+2-\tau} f_{\tau ml} \mathbf{A}_{\tau ml}(\hat{\mathbf{r}}) \quad (3)$$

and where $\mathbf{A}_{\tau ml}(\hat{\mathbf{r}})$ are the *spherical vector harmonics* [AW01, Jac75, Han88], see the appendix for the definition used here. The power carried by each mode is given by $P_{\tau ml} = \frac{1}{2\eta k^2} |f_{\tau ml}|^2$.

Given that the far-field amplitude $\mathbf{F}(\hat{\mathbf{r}})$ of the antenna is available through some measurements, or through some numerical or analytical means, the multipole coefficients can be calculated from the projections

$$f_{\tau ml} = i^{-l-2+\tau} \int \mathbf{A}_{\tau ml}^*(\hat{\mathbf{r}}) \cdot \mathbf{F}(\hat{\mathbf{r}}) d\Omega \quad (4)$$

where we have employed the orthonormality of the spherical vector harmonics [AW01, Jac75, Han88].

When calculating the multipole coefficients (4) from spherical data it is convenient to employ the Fast Fourier Transform (FFT). Let $F^p(\hat{\mathbf{r}})$ denote the spherical components of the far-field amplitude $\mathbf{F}(\hat{\mathbf{r}})$ where $p = \theta, \phi$. Let $\tilde{F}_m^p(\theta)$ denote the Discrete Fourier Transform (DFT) of the spherical components along the azimuthal coordinate ϕ such that

$$F^p(\hat{\mathbf{r}}) = \frac{1}{M} \sum_{m=-M/2+1}^{M/2} \tilde{F}_m^p(\theta) e^{im\phi} \quad (5)$$

where M is the number of azimuthal points and the size of the DFT, $M/2 > L$ and L is assumed to be sufficiently large so that the spatial aliasing in (5) can be neglected.

The spherical vector harmonics $\mathbf{A}_{\tau ml}(\hat{\mathbf{r}})$ and their corresponding DFT's $\tilde{\mathbf{A}}_{\tau ml}(\theta)$ are defined so that $\mathbf{A}_{\tau ml}(\hat{\mathbf{r}}) = \tilde{\mathbf{A}}_{\tau ml}(\theta) e^{im\phi}$, see the appendix. Hence, by the orthogonality of the periodic Fourier basis $e^{im\phi}$, the double integral in (4) can now be calculated conveniently by the single integrals

$$f_{\tau ml} = \frac{2\pi}{M} i^{-l-2+\tau} \sum_{p=\theta, \phi} \int_0^\pi \tilde{A}_{\tau ml}^{p*}(\theta) \cdot \tilde{F}_m^p(\theta) \sin \theta d\theta \quad (6)$$

where $\tilde{A}_{\tau ml}^p(\theta)$ denotes the spherical components of $\tilde{\mathbf{A}}_{\tau ml}(\theta)$.

Consider an arbitrary multiport antenna consisting of N ports. Let x_j^+ and x_j^- denote the corresponding incident and reflected voltages at the antenna waveguide connections for $j = 1, \dots, N$. These voltages are normalized so that the power delivered to a particular antenna port is $\frac{|x_j^+|^2}{2Z_g}$ and the corresponding reflected power is $\frac{|x_j^-|^2}{2Z_g}$ where Z_g is the impedance of the propagating waveguide mode.

On transmission from the input terminals with incident voltage waves x_j^+ ,

the transmitted wave field f_i is given by

$$\begin{bmatrix} \frac{f_i}{k} \end{bmatrix} = \mathbf{T}\mathbf{x}^+ \sqrt{\frac{\eta}{Z_g}} \quad (7)$$

where the multi-index $i = (\tau, m, l)$ is used to simplify the notation, $\mathbf{T} = [T_{ij}]$ is the properly scaled transmission matrix which maps the vector of incident voltage waves $\mathbf{x}^+ = [x_j^+]$ to the multipole coefficients f_i of the propagated outgoing spherical vector waves. The $2L(L+2) \times N$ transmission matrix \mathbf{T} is obtained one column at a time by calculating the far-field and the corresponding multipole coefficients (4) with the corresponding input connections energized one at a time. The reflected voltages are given by $\mathbf{x}^- = \mathbf{\Gamma}\mathbf{x}^+$ where $\mathbf{\Gamma}$ is the reflection matrix. Conservation of total power yields the relationship $\mathbf{\Gamma}^H\mathbf{\Gamma} + \mathbf{T}^H\mathbf{T} \leq \mathbf{I}$ where equality holds for lossless antennas.

Now, considering one single incident wave x_j^+ , the antenna reciprocity theorem [DPG⁺98] yields

$$x_j^- x_j^+ = -i \frac{\lambda^2}{2\pi} \frac{Z_g}{\eta} \mathbf{F}(\hat{\mathbf{k}}_0) \cdot \mathbf{E}_0 \quad (8)$$

where \mathbf{E}_0 is the complex vector amplitude of a plane wave $\mathbf{E}_0 e^{-ik\hat{\mathbf{k}}_0 \cdot \mathbf{r}}$ coming from direction $\hat{\mathbf{k}}_0$ and x_j^- the corresponding received signal. Further, $\mathbf{F}(\hat{\mathbf{r}})$ is the far-field amplitude corresponding to the transmitted signal x_j^+ . Hence, by using (3) the received vector signal is obtained from the reciprocity theorem (8) as

$$\mathbf{x}^- = \sqrt{\frac{Z_g}{\eta}} \lambda \mathbf{R} \mathbf{A} \mathbf{E} \quad (9)$$

where $\mathbf{R} = \mathbf{T}^T$, \mathbf{A} is an $2L(L+2) \times 2$ matrix where each column corresponds to the spherical components of the spherical vector harmonics $i^{l+1-\tau} \mathbf{A}_{\tau ml}(\hat{\mathbf{k}}_0)$, and \mathbf{E} is an 2×1 vector containing the corresponding signal components of the electric field \mathbf{E}_0 .

3 Cramér–Rao Bound for DOA and Polarization Estimation

Based on (9) we consider here the simple snapshot signal model [Tre02]

$$\mathbf{x} = \sqrt{\frac{Z_g}{\eta}} \lambda \mathbf{R} \mathbf{A} \mathbf{E} + \mathbf{n} \quad (10)$$

where the sensor noise \mathbf{n} is zero mean white complex Gaussian noise [Tre02] with variance σ_n^2 and covariance matrix $\sigma_n^2 \mathbf{I}$. We may consider either of the following three models for the received base band vector signal \mathbf{E} .

(1): Assume that \mathbf{E} is constant and thus completely polarized. The field \mathbf{E} can then be modeled as

$$\mathbf{E} = A \begin{pmatrix} \cos \alpha \cos \beta + i \sin \alpha \sin \beta \\ \cos \alpha \sin \beta - i \sin \alpha \cos \beta \end{pmatrix} \quad (11)$$

where A is a complex amplitude, $-\pi/4 \leq \alpha \leq \pi/4$ and $0 \leq \beta \leq \pi$ are angular polarization parameters corresponding to the Stoke's parameters $s_1 = s_0 \cos 2\alpha \cos 2\beta$, $s_2 = s_0 \cos 2\alpha \sin 2\beta$ and $s_3 = s_0 \sin 2\alpha$ for the Poincare sphere [Han88] where $s_0 = |A|^2$. Denote by $\boldsymbol{\xi} = [\theta \ \phi \ \alpha \ \beta]^T$ the vector of DOA and polarization parameters of interest and define the signal-to-noise ratio SNR as

$$\text{SNR} = \frac{Z_g \lambda^2}{\eta} \frac{s_0}{\sigma_n^2}. \quad (12)$$

The *Fisher information matrix* $\mathcal{I}(\boldsymbol{\xi})$ for this situation is given by [Kay93]

$$[\mathcal{I}(\boldsymbol{\xi})]_{ij} = 2\text{SNR} \text{Re} \{ \mathbf{p}_i^H \mathbf{p}_j \} \quad (13)$$

where $\mathbf{p}_i = \mathbf{R} \frac{\partial}{\partial \xi_i} \{ \mathbf{A} \mathbf{E} \}$.

(2): Assume that \mathbf{E} is complex Gaussian and partially polarized. The covariance (coherence) matrix for \mathbf{E} is then given by

$$\mathbf{C}_s = \mathcal{E} \{ \mathbf{E} \mathbf{E}^H \} = \frac{1}{2} \begin{pmatrix} s_0 + s_1 & s_2 + i s_3 \\ s_2 - i s_3 & s_0 - s_1 \end{pmatrix} \quad (14)$$

where \mathcal{E} denotes the expectation operator and s_0, \dots, s_3 denotes the Stoke's parameters [Han88]. Denote by $\boldsymbol{\xi} = [\theta \ \phi \ s_0 \ s_1 \ s_2 \ s_3]^T$ the vector of DOA and polarization parameters of interest and let the signal-to-noise ratio SNR be given by (12). The Fisher information matrix $\mathcal{I}(\boldsymbol{\xi})$ for this situation is given by [Kay93]

$$[\mathcal{I}(\boldsymbol{\xi})]_{ij} = \text{tr} \left\{ \mathbf{C}^{-1} \frac{\partial \mathbf{C}}{\partial \xi_i} \mathbf{C}^{-1} \frac{\partial \mathbf{C}}{\partial \xi_j} \right\} \quad (15)$$

where \mathbf{C} is the covariance matrix for the measurements,

$$\mathbf{C} = \mathcal{E} \{ \mathbf{x} \mathbf{x}^H \} = \sigma_n^2 \left(\text{SNR} \frac{1}{s_0} \mathbf{R} \mathbf{A} \mathbf{C}_s \mathbf{A}^H \mathbf{R}^H + \mathbf{I} \right). \quad (16)$$

(3): Assume that \mathbf{E} is complex Gaussian and completely polarized. Here \mathbf{E} is given by (11) where the amplitude A is zero mean complex Gaussian with variance $s_0 = \mathcal{E}\{|A|^2\}$. The covariance matrix for \mathbf{E} is again given by (14) where $s_1 = s_0 \cos 2\alpha \cos 2\beta$, $s_2 = s_0 \cos 2\alpha \sin 2\beta$ and $s_3 = s_0 \sin 2\alpha$. Denote by $\boldsymbol{\xi} = [\theta \ \phi \ s_0 \ \alpha \ \beta]^T$ the vector of DOA and polarization parameters of interest and let the signal-to-noise ratio SNR be given by (12). The Fisher information matrix $\mathcal{I}(\boldsymbol{\xi})$ for this situation is again given by (15).

When calculating the Fisher information according to either (13) or (15) we need to calculate the derivatives $\frac{\partial \mathbf{A}}{\partial \theta}$ and $\frac{\partial \mathbf{A}}{\partial \phi}$ of the spherical vector harmonics. Denoting the $2L(L+2) \times 2$ matrix \mathbf{A} by

$$\mathbf{A} = [\mathbf{i}^{l+1-\tau} \tilde{A}_{\tau ml}^\theta(\theta) e^{im\phi}, \quad \mathbf{i}^{l+1-\tau} \tilde{A}_{\tau ml}^\phi(\theta) e^{im\phi}] \quad (17)$$

we have

$$\begin{aligned} \frac{\partial \mathbf{A}}{\partial \theta} &= [\mathbf{i}^{l+1-\tau} \frac{\partial \tilde{A}_{\tau ml}^\theta(\theta)}{\partial \theta} e^{im\phi}, \quad \mathbf{i}^{l+1-\tau} \frac{\partial \tilde{A}_{\tau ml}^\phi(\theta)}{\partial \theta} e^{im\phi}] \\ \frac{\partial \mathbf{A}}{\partial \phi} &= [\mathbf{i}^{l+1-\tau} im \tilde{A}_{\tau ml}^\theta(\theta) e^{im\phi}, \quad \mathbf{i}^{l+1-\tau} im \tilde{A}_{\tau ml}^\phi(\theta) e^{im\phi}] \end{aligned} \quad (18)$$

where

$$\begin{aligned} \frac{\partial \tilde{A}_{1ml}^\theta(\theta)}{\partial \theta} &= \frac{\partial \tilde{A}_{2ml}^\phi(\theta)}{\partial \theta} = \\ &= \frac{(-1)^m}{\sqrt{2\pi l(l+1)} \sin^2(\theta)} im \left(\frac{\partial \bar{P}_l^m(\cos \theta)}{\partial \theta} \sin \theta - \bar{P}_l^m(\cos \theta) \cos \theta \right) \\ \frac{\partial \tilde{A}_{1ml}^\phi(\theta)}{\partial \theta} &= -\frac{\partial \tilde{A}_{2ml}^\theta(\theta)}{\partial \theta} = \frac{-(-1)^m}{\sqrt{2\pi l(l+1)}} \frac{\partial^2 \bar{P}_l^m(\cos \theta)}{\partial \theta^2} \end{aligned} \quad (19)$$

are obtained from (28) and $\frac{\partial \bar{P}_l^m(\cos \theta)}{\partial \theta}$ and $\frac{\partial^2 \bar{P}_l^m(\cos \theta)}{\partial \theta^2}$ by repeated use of (27).

4 Numerical Examples

4.1 Polarization estimation with an ideal tripole antenna array

In Fig. 1 is shown the optimum transmission coefficients $|t_l|^2$ from (2) with Q -factors corresponding to the first 3 mode orders $l = 1, 2, 3$, *cf.*, [CR64], as the electrical size ka as well as the fractional bandwidth B is varied. The

figure illustrates the difficulty to match higher order modes, as well as the fact that all modes will ultimately become useful (useless) as the electrical size increases (decreases), or as the bandwidth decreases (increases).

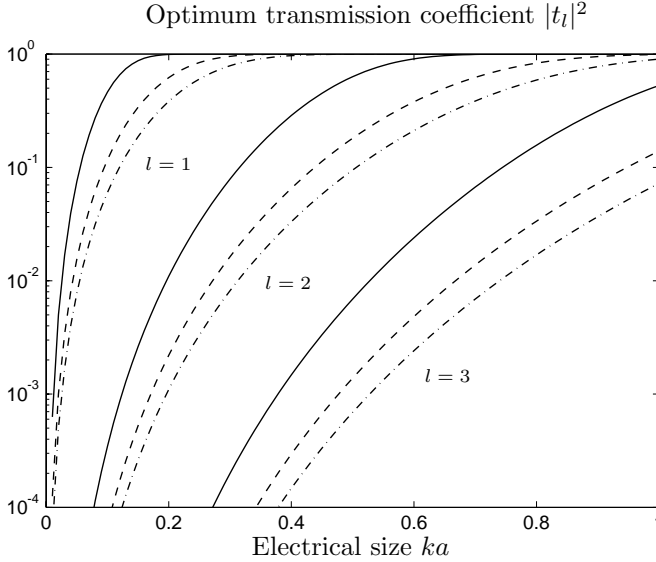


Figure 1: Optimum transmission coefficient $|t_l|^2$ as a function of electrical size ka for the first 3 mode orders $l = 1, 2, 3$. Fractional bandwidth is $B = 1, 5, 10$ %.

Consider now a single, ideal tripole antenna array with

$$\mathbf{A} = \sqrt{\frac{3}{8\pi}} \begin{pmatrix} \cos \theta \cos \phi & -\sin \phi \\ \cos \theta \sin \phi & \cos \phi \\ -\sin \theta & 0 \end{pmatrix} \quad (20)$$

corresponding to the three fundamental TM modes of lowest order $l = 1$, or equivalently, the three ideal electrical dipoles in the cartesian base vector directions $\hat{\mathbf{x}}, \hat{\mathbf{y}}, \hat{\mathbf{z}}$.

In Fig. 2 is shown the Cramér–Rao bound for the polarization parameters s_0, s_1, s_2 and s_3 versus electrical size ka in a situation where the unknown parameters are $\boldsymbol{\xi} = [s_0 \ s_1 \ s_2 \ s_3 \ \sigma_n^2]^T$. The diagonal elements of $\mathcal{I}^{-1}(\boldsymbol{\xi})$ are based on (15) with the optimum transmission coefficients $\mathbf{T} = \text{diag}\{t_l\}$ calculated as in (2) with $B = 5$ % and $Q = \frac{1}{ka} + \frac{1}{(ka)^3}$, cf., [CR64]. The

Stoke's parameters are parameterized as

$$\begin{aligned} s_1 &= P s_0 \cos(2\alpha) \cos(2\beta) \\ s_2 &= P s_0 \cos(2\alpha) \sin(2\beta) \\ s_3 &= P s_0 \sin(2\alpha) \end{aligned} \quad (21)$$

where $0 \leq P \leq 1$ is the *degree of polarization*. The signal-to-noise ratio (12) was chosen to 50 dB. In this example we have chosen a situation with circular polarization with $s_0 = 1$, $s_1 = 0$, $s_2 = 0$ and $s_3 = 1$. The solid, dashed-dotted, dashed and dotted lines correspond to $P = 0, 0.9, 0.99$ and 1, respectively. The result in Fig. 2 is invariant to the directional parameters θ and ϕ but depends strongly on polarization. In particular, only s_1 and s_2 can be efficiently estimated in this example, and the performance improves drastically as the degree of polarization P approaches unity. It should be noted that we employ here a one snapshot signal model and that the performance will naturally improve by employing several signal samples of (10).

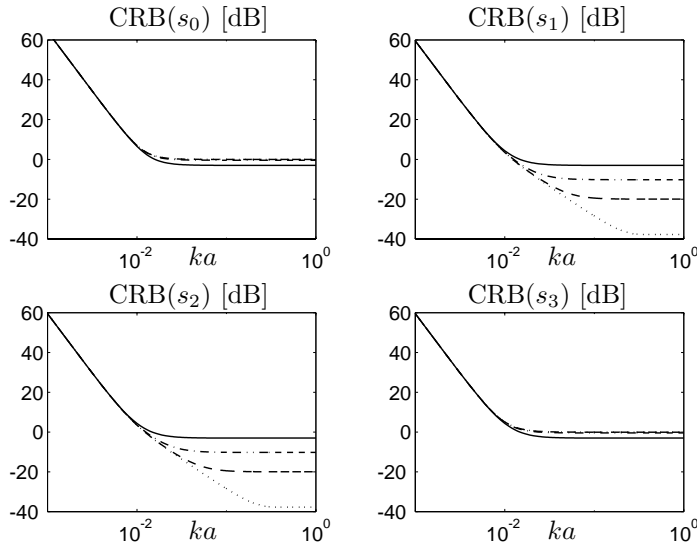


Figure 2: Cramér-Rao bound for the polarization parameters s_0 , s_1 , s_2 and s_3 versus electrical size ka . Circular polarization with $s_0 = 1$, $s_1 = 0$, $s_2 = 0$ and $s_3 = 1$. The solid, dashed-dotted, dashed and dotted lines correspond to $P = 0, 0.9, 0.99$ and 1, respectively. SNR is 50 dB and $B = 5\%$.

Although the result above should be expected, it can be better understood by performing a principal parameter analysis. We define the principal parameters $\boldsymbol{\eta}$ to be the linear transformation

$$\boldsymbol{\eta} = \mathbf{U}^H \boldsymbol{\xi} \quad (22)$$

where \mathbf{U} are the left singular vectors from the Singular Value Decomposition (SVD) of the Fisher information, $\mathcal{I}(\boldsymbol{\xi}) = \mathbf{U} \boldsymbol{\Sigma} \mathbf{V}^H$. The principal parameters η_i are uncoupled, and their corresponding Cramér–Rao bounds are the reciprocal of the singular values σ_i^{-1} .

Fig. 3 a) shows the Cramér–Rao bounds σ_i^{-1} for the principal parameters η_i , as well as $-\log \det \mathcal{I}$ plotted as a function of the degree of polarization P . Fig. 3 b) shows the corresponding results for the original parameters ξ_i . The parameter situation is the same as above, except now SNR is 30 dB and $ka = 1$.

Note that the performance results for the principal parameters in Fig. 3 a) are invariant not only to the directional parameters θ and ϕ , but are also invariant to the polarization parameters α and β . In other words, the performance of the principal parameters η_i depends only on the degree of polarization P , whereas the performance of the original parameters ξ_i depends also on the actual situation with polarization parameters α and β .

In this example with circular polarization, it is concluded that the relevant parameters to measure are s_1 and s_2 whereas s_0 and s_3 cannot be measured as efficiently. By studying the left singular vectors in \mathbf{U} , we can identify the principal parameters as linear combinations of the original parameters. The “best” parameter η_1 corresponds directly to the noise parameter σ_n^2 which is thus a relevant parameter to measure. Further, $\eta_2 \sim s_3 - s_0$ and $\eta_5 \sim s_3 + s_0$ are “good” and “poor” parameters to estimate, respectively. It is furthermore “appropriate” to estimate s_1 and s_2 since (s_1, s_2) belongs to the subspace spanned by the singular vectors corresponding to the two principal parameters η_3 and η_4 sharing the same singular value (and hence the same Cramér–Rao bound). It should also be noted that the SVD produces here a decomposition which has a direct physical significance. Thus, $\eta_2 \sim s_3 - s_0$ and $\eta_5 \sim s_3 + s_0$ correspond also to the power in the left and right circularly polarized components, respectively, see *e.g.*, [Han88]. Hence, given that the wave is right circularly polarized (as in our example), the (absolute) performance of estimating the power of a weak left circularly polarized signal component is much better than for estimating the power of the dominating right circularly polarized signal component.

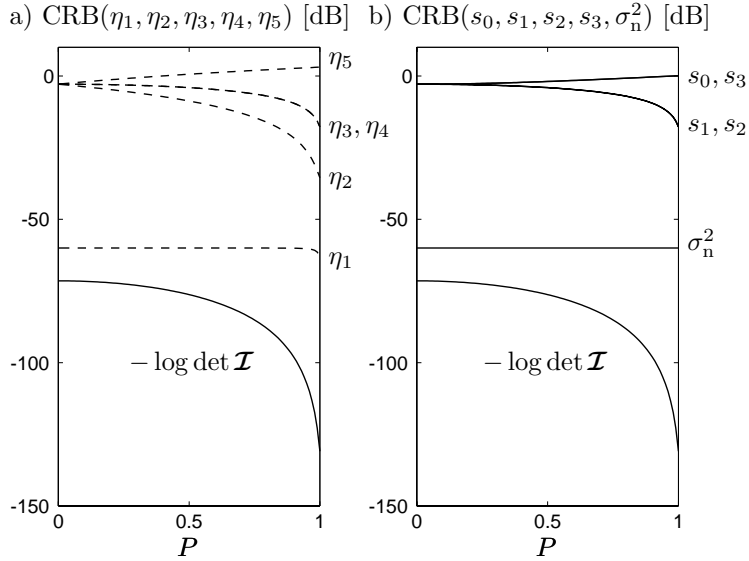


Figure 3: a) Cramér–Rao bound for the principal parameters $\eta_1, \eta_2, \eta_3, \eta_4, \eta_5$ versus degree of polarization P . b) Cramér–Rao bound for the polarization parameters s_0, s_1, s_2, s_3 and σ_n^2 versus degree of polarization P . Circular polarization with $s_0 = 1, s_1 = 0, s_2 = 0$ and $s_3 = 1$. SNR is 30 dB, $ka = 1$ and $B = 5\%$.

In conclusion, the study shows that the estimation performance of the tripole antenna as measured by the functional $\log \det \mathcal{I}(\xi)$ is invariant to the directional parameters θ and ϕ as well as to the polarization parameters α and β . However, the functional $\log \det \mathcal{I}(\xi)$ depends strongly on the degree of polarization P , as well as on the electrical size ka of the antenna and the bandwidth B of the system. The principal parameter analysis is a useful technique to investigate the significance of different parameters.

4.2 DOA estimation with a non-ideal tetrahedron array

We consider now an array of antennas consisting of six half wave dipoles centered on the edges of a tetrahedron where each edge has the length of one wave, see Fig. 4. We have utilized SuperNec[©] 2.9¹, a Method of Moments

¹SuperNec 2.9 is a product of the Poynting Group. www.supernec.com

based electromagnetic simulation software to obtain the far-field amplitude $\mathbf{F}(\hat{\mathbf{r}})$ used in (4). The far-field amplitude $F^\theta(\hat{\mathbf{r}})$ for the six elements are shown in Fig. 5 using $L = 10$ and hence $2L(L + 2) = 240$ multipole coefficients.

In Fig. 6 is shown the Cramér–Rao lower bound (CRB) [Kay93] for DOA estimation based on (13) when the polarization is given by $\alpha = \beta = 0$ (linear $\hat{\boldsymbol{\theta}}$ -polarization) which is assumed to be known. The signal to noise ratio is $\text{SNR} = 0$ dB. Fig. 6 a) and b) show the CRB when all six elements of the array is used. Fig. 6 c) and d) show the corresponding results using only the two elements no. 2 and 3, a situation which is more easily related to the responses shown in Fig. 5. Note also the higher levels and dynamics of the CRB when only two elements are used.

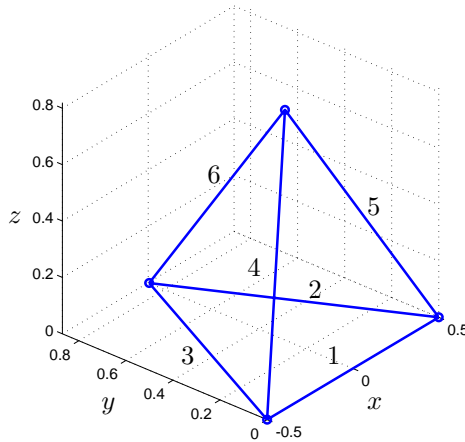


Figure 4: Geometry for the six element tetrahedron array.

5 Summary

Fundamental physical limitations associated with DOA and polarization estimation using arbitrary antennas or antenna arrays are analyzed. By using spherical vector modes as a generic model for the transmission, we show how the corresponding Cramér–Rao bounds can be calculated for any real antenna system. The electromagnetic model is rather complex, but is straightforward, generally applicable and complete in the sense that it incorporates all electromagnetic properties of the antenna system such as mutual coupling effects, etc. The spherical vector modes and their associated equivalent circuits and

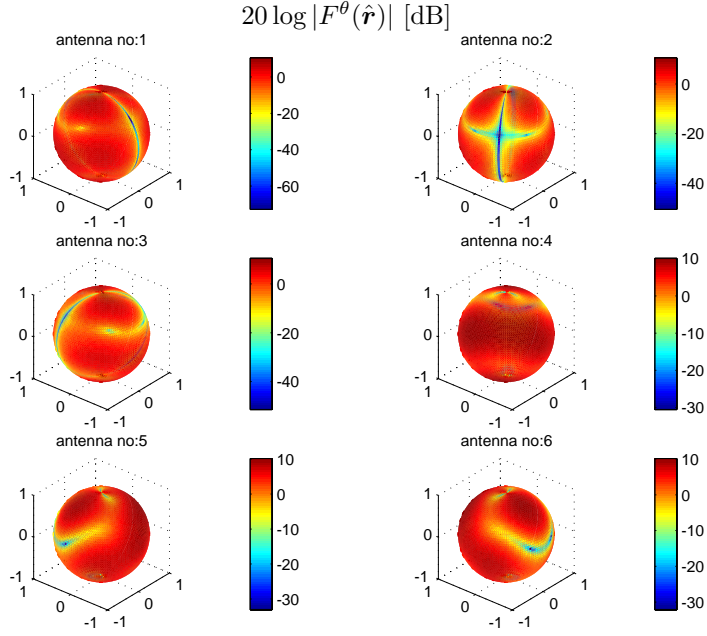


Figure 5: Far-field amplitude $F^\theta(\hat{\mathbf{r}})$ for the six antennas in the array.

Q factor approximations are used together with the broadband Fano theory as a general framework for analyzing electrically small multiport antennas. A principal parameter analysis using the SVD of the Fisher information matrix is employed to evaluate the performance of an ideal tripole antenna array with respect to its ability to estimate the state of polarization of a partially polarized plane wave coming from a given direction. As an example of an arbitrary multiport antenna we employ the non-ideal tetrahedron array (with mutual coupling) and analyze its performance with respect to the Cramér–Rao bound for DOA estimation.

Future work includes an investigation about possible estimation algorithms, such as those mentioned in *e.g.*, [RTS04, WZ00, Li93, SV93, HTT98, WF93, LS94, HN95, HTT97, HTN99, WLZ04, Won01] that could exploit and take advantage of the presented generic model.

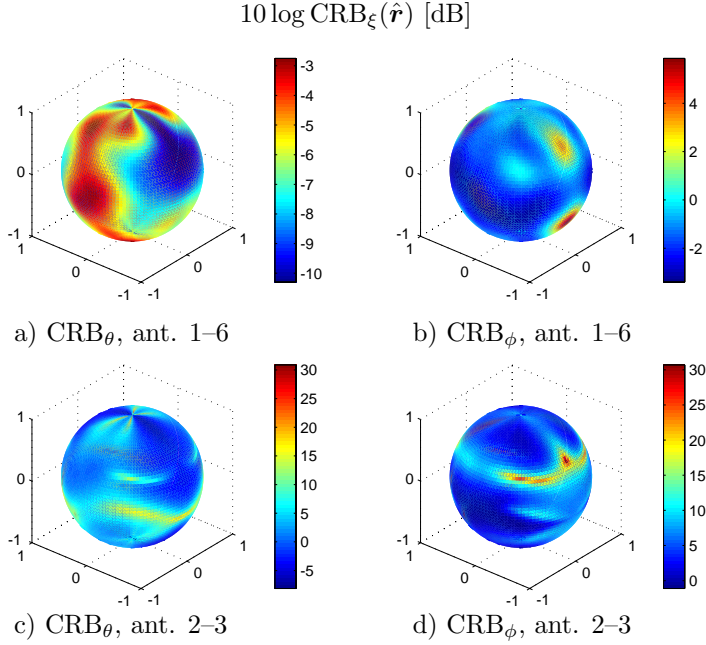


Figure 6: Cramér–Rao lower bound $\text{CRB}_\xi(\hat{\mathbf{r}})$ for DOA estimation. a) CRB_θ : antenna 1–6, b) CRB_ϕ : antenna 1–6, c) CRB_θ : antenna 2–3, d) CRB_ϕ : antenna 2–3.

Acknowledgement

The authors gratefully acknowledge the financial support by the Swedish Research Council.

A Spherical Vector Waves

The outgoing spherical vector waves are given by

$$\begin{aligned}
 \mathbf{u}_{1ml}(k\mathbf{r}) &= h_l^{(2)}(kr) \mathbf{A}_{1ml}(\hat{\mathbf{r}}) \\
 \mathbf{u}_{2ml}(k\mathbf{r}) &= \frac{1}{k} \nabla \times \mathbf{u}_{1ml}(k\mathbf{r}) = \\
 &= \frac{(kr h_l^{(2)}(kr))'}{kr} \mathbf{A}_{2ml}(\hat{\mathbf{r}}) + \sqrt{l(l+1)} \frac{h_l^{(2)}(kr)}{kr} \mathbf{A}_{3ml}(\hat{\mathbf{r}})
 \end{aligned} \tag{23}$$

where $\mathbf{A}_{\tau ml}(\hat{\mathbf{r}})$ are the *spherical vector harmonics* and $h_l^{(2)}(x)$ the *spherical Hankel functions of the second kind*, see [AW01, Jac75, Han88].

The spherical vector harmonics $\mathbf{A}_{\tau ml}(\hat{\mathbf{r}})$ are given by

$$\begin{aligned}\mathbf{A}_{1ml}(\hat{\mathbf{r}}) &= \frac{1}{\sqrt{l(l+1)}} \nabla \times (\mathbf{r} Y_{ml}(\hat{\mathbf{r}})) \\ \mathbf{A}_{2ml}(\hat{\mathbf{r}}) &= \hat{\mathbf{r}} \times \mathbf{A}_{1ml}(\hat{\mathbf{r}}) \\ \mathbf{A}_{3ml}(\hat{\mathbf{r}}) &= \hat{\mathbf{r}} Y_{ml}(\hat{\mathbf{r}})\end{aligned}\quad (24)$$

where $Y_{ml}(\hat{\mathbf{r}})$ are the scalar *spherical harmonics* given by

$$Y_{ml}(\theta, \phi) = (-1)^m \sqrt{\frac{2l+1}{4\pi}} \sqrt{\frac{(l-m)!}{(l+m)!}} P_l^m(\cos \theta) e^{im\phi} \quad (25)$$

and where $P_l^m(x)$ are the *associated Legendre functions* [AW01].

For convenience, we introduce also the *normalized* associated Legendre functions

$$\bar{P}_l^m(x) = \sqrt{\frac{2l+1}{2}} \sqrt{\frac{(l-m)!}{(l+m)!}} P_l^m(x) \quad (26)$$

so that $Y_{ml}(\hat{\mathbf{r}}) = (-1)^m \bar{P}_l^m(\cos \theta) \frac{1}{\sqrt{2\pi}} e^{im\phi}$. The following relations for $\bar{P}_l^m(x)$ are useful for numerical calculations [AW01, Han88]

$$\begin{aligned}\bar{P}_l^{-m}(x) &= (-1)^m \bar{P}_l^m(x) \\ \frac{\partial}{\partial \theta} \bar{P}_l^m(\cos \theta) &= \frac{1}{2} \sqrt{(l+m)(l-m+1)} \bar{P}_l^{m-1}(\cos \theta) \\ &\quad - \frac{1}{2} \sqrt{(l+m+1)(l-m)} \bar{P}_l^{m+1}(\cos \theta).\end{aligned}\quad (27)$$

Note also that $\bar{P}_l^m(x) = 0$ for $m > l$.

Now, from (24) the spherical vector harmonics may be derived as

$$\begin{aligned}\mathbf{A}_{1ml}(\hat{\mathbf{r}}) &= \tilde{\mathbf{A}}_{1ml}(\theta) e^{im\phi} = \\ &= \frac{(-1)^m}{\sqrt{l(l+1)}} \left(\hat{\boldsymbol{\theta}} \frac{im}{\sin \theta} \bar{P}_l^m(\cos \theta) - \hat{\boldsymbol{\phi}} \frac{\partial}{\partial \theta} \bar{P}_l^m(\cos \theta) \right) \frac{1}{\sqrt{2\pi}} e^{im\phi} \\ \mathbf{A}_{2ml}(\hat{\mathbf{r}}) &= \tilde{\mathbf{A}}_{2ml}(\theta) e^{im\phi} = \\ &= \frac{(-1)^m}{\sqrt{l(l+1)}} \left(\hat{\boldsymbol{\theta}} \frac{\partial}{\partial \theta} \bar{P}_l^m(\cos \theta) + \hat{\boldsymbol{\phi}} \frac{im}{\sin \theta} \bar{P}_l^m(\cos \theta) \right) \frac{1}{\sqrt{2\pi}} e^{im\phi} \\ \mathbf{A}_{3ml}(\hat{\mathbf{r}}) &= \tilde{\mathbf{A}}_{3ml}(\theta) e^{im\phi} = \hat{\mathbf{r}} (-1)^m \bar{P}_l^m(\cos \theta) \frac{1}{\sqrt{2\pi}} e^{im\phi}\end{aligned}\quad (28)$$

where the *Fourier transformed* spherical vector harmonics $\tilde{\mathbf{A}}_{\tau ml}(\theta)$ are defined so that

$$\mathbf{A}_{\tau ml}(\hat{\mathbf{r}}) = \tilde{\mathbf{A}}_{\tau ml}(\theta) e^{im\phi}. \quad (29)$$

Note that $\tilde{\mathbf{A}}_{rml}(\theta)$ is defined as the Fourier transform only with respect to the respective spherical r, θ, ϕ components. As a vector field $\tilde{\mathbf{A}}_{rml}(\theta)$ still depend on the ϕ coordinate via the basis vectors $\hat{\mathbf{r}}, \hat{\boldsymbol{\theta}}, \hat{\boldsymbol{\phi}}$.

References

- [AW01] G. B. Arfken and H. J. Weber. *Mathematical Methods for Physicists*. Academic Press, New York, fifth edition, 2001.
- [CR64] R. E. Collin and S. Rothschild. Evaluation of antenna Q. *IEEE Transactions on Antennas and Propagation*, 12:23–27, January 1964.
- [DPG⁺98] S. Drabowitch, A. Papiernik, H. Griffiths, J. Encinas, and B. L. Smith. *Modern Antennas*. Chapman & Hall, 1998.
- [Fan50] R. M. Fano. Theoretical limitations on the broadband matching of arbitrary impedances. *Journal of the Franklin Institute*, 249(1,2):57–83 and 139–154, Jan/Feb 1950.
- [GJQ00] W. Geyi, P. Jarmuszewski, and Y. Qi. The Foster reactance theorem for antennas and radiation Q. *IEEE Transactions on Antennas and Propagation*, 48(3):401–408, March 2000.
- [GN04] M. Gustafsson and S. Nordebo. On the spectral efficiency of a sphere. Technical Report LUTEDX/(TEAT-7127)/1–24/(2004), Lund Institute of Technology, Department of Electrosience, P.O. Box 118, S-211 00 Lund, Sweden, 2004.
- [Han81] R. C. Hansen. Fundamental limitations in antennas. *Proceedings. IEEE*, 69(2):170–182, 1981.
- [Han88] J. E. Hansen, editor. *Spherical Near-Field Antenna Measurements*. Number 26 in IEE electromagnetic waves series. Peter Peregrinus Ltd., Stevenage, UK, 1988. ISBN: 0-86341-110-X.
- [HN95] B. Hochwald and A. Nehorai. Polarimetric modeling and parameter estimation with applications to remote sensing. *IEEE Transactions on Signal Processing*, 43(8):1923–1935, August 1995.

- [HTN99] K-C Ho, K-C Tan, and A. Nehorai. Estimating directions of arrival of completely and incompletely polarized signals with electromagnetic vector sensors. *IEEE Transactions on Signal Processing*, 47(10):2845–2852, October 1999.
- [HTT97] K-C Ho, K-C Tan, and B. T. G. Tan. Efficient method for estimating directions-of-arrival of partially polarized signals with electromagnetic vector sensors. *IEEE Transactions on Signal Processing*, 45(10):2485–2498, October 1997.
- [HTT98] K-C Ho, K-C Tan, and B. T. G. Tan. Linear dependence of steering vectors associated with tripole arrays. *IEEE Transactions on Antennas and Propagation*, 46(11):1705–1711, November 1998.
- [Jac75] J. D. Jackson. *Classical Electrodynamics*. John Wiley & Sons, New York, second edition, 1975.
- [Kar04] A. Karlsson. Physical limitations of antennas in a lossy medium. *IEEE Transactions on Antennas and Propagation*, 52(8):2027–2033, 2004.
- [Kay93] S. M. Kay. *Fundamentals of Statistical Signal Processing, Estimation Theory*. Prentice-Hall, Inc., NJ, 1993.
- [KV96] H. Krim and M. Viberg. Two decades of array signal processing research: the parametric approach. *IEEE Signal Processing Magazine*, 13(4):67–94, July 1996.
- [Li93] J. Li. Direction and polarization estimation using arrays with small loops and short dipoles. *IEEE Transactions on Antennas and Propagation*, 41(3):379–387, March 1993.
- [LS94] J. Li and P. Stoica. Efficient parameter estimation of partially polarized electromagnetic waves. *IEEE Transactions on Signal Processing*, 42(11):3114–3125, November 1994.
- [McL96] J. S. McLean. A re-examination of the fundamental limits on the radiation Q of electrically small antennas. *IEEE Transactions on Antennas and Propagation*, 44(5):672–676, May 1996.
- [NG05] S. Nordebo and M. Gustafsson. Multichannel broadband Fano theory for arbitrary lossless antennas with applications in DOA

- estimation. In *2005 IEEE International Conference on Acoustics, Speech, and Signal Processing*. IEEE Signal Processing Society, 2005.
- [NG06] S. Nordebo and M. Gustafsson. Statistical signal analysis for the inverse source problem of electromagnetics. *IEEE Transactions on Signal Processing*, 54(6):2357–2362, 2006.
- [QQS05] Y. Qiaowei, C. Qiang, and K. Sawaya. Accurate DOA estimation using array antenna with arbitrary geometry. *IEEE Transactions on Antennas and Propagation*, 53(4):1352–1358, 2005.
- [RTS04] D. Rahamim, J. Tabrikian, and R. Shavit. Source localization using vector sensor array in a multipath environment. *IEEE Transactions on Signal Processing*, 52(11):3096–3103, 2004.
- [SN90] P. Stoica and A. Nehorai. MUSIC, maximum likelihood, and Cramér-Rao bound: further results and comparisons. *IEEE Transactions on Acoustics, Speech, and Signal Processing*, 38(12):2140–2150, December 1990.
- [SV93] A. Swindlehurst and M. Viberg. Subspace fitting with diversely polarized antenna arrays. *IEEE Transactions on Antennas and Propagation*, 41(12):1687–1694, December 1993.
- [Tre02] H. L. Van Trees. *Optimum Array Processing*. John Wiley & Sons, Inc., New York, 2002.
- [VSO97] M. Viberg, P. Stoica, and B. Ottersten. Maximum likelihood array processing in spatially correlated noise fields using parameterized signals. *IEEE Transactions on Signal Processing*, 45(4):996–1004, April 1997.
- [WF93] A. J. Weiss and B. Friedlander. Maximum likelihood signal estimation for polarization sensitive arrays. *IEEE Transactions on Antennas and Propagation*, 41(7):918–925, July 1993.
- [WLZ04] K. T. Wong, L. Li, and M. D. Zoltowski. Root-MUSIC-based direction-finding and polarization estimation using diversely polarized possibly colocated antennas. *IEEE Antennas & Wireless Propagation Letters*, 3(8):129–132, 2004.

- [Won01] K. T. Wong. Direction finding/polarization estimation – dipole and/or loop triad(s). *IEEE Transactions on Aerospace and Electronic Systems*, 37(2):679–684, April 2001.
- [WZ00] K. T. Wong and M. D. Zoltowski. Closed-form direction finding and polarization estimation with arbitrarily spaced electromagnetic vector-sensors at unknown locations. *IEEE Transactions on Antennas and Propagation*, 48(5):671–681, May 2000.

PART III

**On the Design of Optimal
Cylindrical Antenna
Near-Field Measurements**

Part III is published as:

J. Lundbäck, "On the Design of Optimal Cylindrical Antenna Near-Field Measurements", *Research Report 07043*, ISSN 1650-2647, VXU/MSI/EL/R/-07043/-SE, Växjö University, Sweden, March 2007.

To be submitted.

On the Design of Optimal Cylindrical Antenna Near-Field Measurements

J. Lundbäck

Abstract

In this report, the theory of optimal experiments is applied to cylindrical antenna near-field measurements. A D-optimal formulation based on the Fisher information of the multipole coefficients in the spherical wave expansion of the electrical field is considered. The solution to the semi-definite optimization problem results in optimal measurement points. Using the optimal measurement points, the inverse source problem is solved by a least-square based method. The properties of the estimation of the multipole coefficients, the corresponding electric field and the optimization formulation are studied using numerical examples and singular value analysis.

1 Introduction

Many applications involving antennas require knowledge of the antenna properties that are obtained from antenna measurements. Antenna parameters to be determined include *e.g.*, gain and antenna far-field pattern. Depending on the antenna construction and frequency of operation, either far-field or near-field measurements are employed. The far-field measurement demand a large and expensive out-door range making this method disadvantageous [Han88].

The near-field measurement can be constructed indoor, and in a more compact space, enabling a more attractive measurement configuration. Using the spherical vector wave expansion of the electromagnetic field, the antenna properties can be calculated once the multipole coefficients have been estimated and systematic errors have been removed via the probe calibration, see *e.g.*, [RS04, Lai05, PG05, NG06b, NGP07].

Consider the antenna measurement as an optimal experiment [EN98]. The objective of an optimal experiment is to adjust the experiment parameters so that a suitable measure of optimality is maximized *e.g.*, [WGF06, Fed72, AD92]. The parameters of the experiment and the measure of optimality vary in different applications *e.g.*, in system identification, the parameter that define the input signal should be optimum in the sense that the corresponding output signal of the unidentified system provides maximum information to the identification process, see *e.g.*, [LSL02]. Beside the antenna near-field measurement, other applications that have benefited from the optimal experiment design are measurement intensive applications involving several experiment parameters *e.g.*, Tomography and Ground Penetrating Radar [XC04, PLP93, SXC05, ACM06, NG06a].

Here, based on the cylindrical measurement configuration, the experiment parameters are the measurement positions of the near-field measurement. The optimal measurement positions are obtained from the solution to a semi-definite optimization formulation where the determinant of the Fisher information matrix [Kay93] is maximized, which is termed a D-optimal experiment [VBW98, VB99]. Generally, the formulation of the optimal experiment depends on the unknown parameters that should be estimated using the data obtained from optimal experiment [Hja05].

The electrical field of the antenna under test is constructed of generated multipole coefficients. At the optimal measurement points, samples of two polarizations of the electrical field are used to solve the inverse source problem based on a least-square method. The near-field estimation of the electric field follows after the estimation of the multipole coefficients in the spherical vector wave expansion of the electrical field [Han88].

The report is organized as follows. In part 2, the electric near-field is described using the spherical vector wave expansion in a cylindrical measurement configuration. The Fisher information matrix of the multipole coefficients is given and the solution method to the inverse problem is described. Next, in part 3 the optimal measurement formulation is given, along with the measures of the estimation performance. Numerical examples are included in part 4.

2 Antenna Near-Field Estimation Based on Cylindrical Data

We consider the antenna near-field estimation problem based on cylindrical data. Let (r, θ, ϕ) and (ρ, ϕ, z) denote the spherical and cylindrical coordinates, respectively. Further, let $k = \omega/c$ denote the wave number, $\omega = 2\pi f$ the angular frequency, and c and η the speed of light and the wave impedance of free space, respectively.

Assume that all sources are contained inside a sphere of radius $r = a$, and let $e^{i\omega t}$ be the time-convention. The transmitted electric field, $\mathbf{E}(\mathbf{r})$, can then be expanded in *outgoing spherical vector waves* $\mathbf{u}_{\tau ml}(k\mathbf{r})$ for $r > a$ as [AW01, Jac75, Han88]

$$\mathbf{E}(\mathbf{r}) = \sum_{l=1}^{\infty} \sum_{m=-l}^l \sum_{\tau=1}^2 f_{\tau ml} \mathbf{u}_{\tau ml}(k\mathbf{r}) \quad (1)$$

where $f_{\tau ml}$ are the multipole coefficients. Here $\tau = 1$ corresponds to a transversal electric (TE) wave and $\tau = 2$ corresponds to a transversal magnetic (TM) wave. The other indices are $l = 1, 2, \dots, \infty$ and $m = -l, \dots, l$ where l denotes the *order* of that mode. In principle, the sum in (1) is infinite. However, for all practical purposes the maximum useful order L is finite and is physically restricted by the electrical size ka of the sphere as well as the bandwidth of the antenna, see *e.g.*, [Han88, NG05].

We consider now the inverse, linear estimation problem of determining the multipole coefficients $f_{\tau ml}$ based on an observation of the electric near field, $\mathbf{E}(\mathbf{r})$, as it is measured on the cylindrical surface $\{\rho = \rho_0, z_1 \leq z \leq z_2\}$. We assume that the measurement is corrupted by additive and spatially uncorrelated complex Gaussian noise $\mathbf{N}(\mathbf{r})$ with zero mean and dyadic covariance function $\mathcal{E}\{\mathbf{N}(\mathbf{r})\mathbf{N}^*(\mathbf{r}')\} = \sigma_n^2 \delta(\mathbf{r} - \mathbf{r}') \mathbf{I}$ where $\mathcal{E}\{\cdot\}$ denotes the expectation operator, σ_n^2 the noise variance, $\delta(\mathbf{r})$ the impulse function and \mathbf{I} the identity dyad. Note that since the data is discrete, $\delta(\cdot)$ denotes the discrete impulse function with $\delta(0) = 1$.

When we wish to estimate the near field at a sphere of radius $r = a$, the linear equations in (1) are first regularized by normalizing with the vector norm $\|\mathbf{u}_{\tau ml}(k\mathbf{r})\| = (\int |\mathbf{u}_{\tau ml}(k\mathbf{r})|^2 d\Omega)^{1/2}$ where $d\Omega$ is the differential solid angle. By the orthonormality of the spherical vector harmonics [AW01, Jac75,

Han88], we have

$$\begin{aligned}\|\mathbf{u}_{1ml}(k\mathbf{r})\|_{r=a}^2 &= \left| h_l^{(2)}(ka) \right|^2 \\ \|\mathbf{u}_{2ml}(k\mathbf{r})\|_{r=a}^2 &= \left| \frac{(ka h_l^{(2)}(ka))'}{ka} \right|^2 + l(l+1) \left| \frac{h_l^{(2)}(ka)}{ka} \right|^2\end{aligned}\quad (2)$$

which are independent of the azimuthal m -index.

Consider first a situation where we have arbitrary measurement points \mathbf{r}_j for $j = 1, \dots, n$. The Fisher information matrix [Kay93] for estimating the normalized multipole coefficients $f_{\tau ml}$ is then given by

$$\begin{aligned}[\mathcal{I}]_{\tau ml, \tau' m' l'} &= \frac{1}{\sigma_n^2} \sum_{j=1}^n \frac{\partial \mathbf{E}^*(\mathbf{r}_j)}{\partial f_{\tau ml}^*} \cdot \frac{\partial \mathbf{E}(\mathbf{r}_j)}{\partial f_{\tau' m' l'}} \\ &= \frac{1}{\sigma_n^2} \sum_{j=1}^n \frac{\mathbf{u}_{\tau ml}^*(k\mathbf{r}_j)}{\|\mathbf{u}_{\tau ml}(k\mathbf{r})\|_{r=a}} \cdot \frac{\mathbf{u}_{\tau' m' l'}(k\mathbf{r}_j)}{\|\mathbf{u}_{\tau' m' l'}(k\mathbf{r})\|_{r=a}}.\end{aligned}\quad (3)$$

Now, assume that we have a cylindrical measurement using M azimuthal points ϕ equally spaced in $[0, 2\pi]$, and n vertical positions z_j with spherical coordinates (r_j, θ_j) . The Fisher information (3) then becomes

$$[\mathcal{I}]_{\tau ml, \tau' m' l'} = \frac{M}{\sigma_n^2} \sum_{j=1}^n \frac{\tilde{\mathbf{u}}_{\tau ml}^*(r_j, \theta_j)}{\|\mathbf{u}_{\tau ml}(k\mathbf{r})\|_{r=a}} \cdot \frac{\tilde{\mathbf{u}}_{\tau' m' l'}(r_j, \theta_j)}{\|\mathbf{u}_{\tau' m' l'}(k\mathbf{r})\|_{r=a}} \delta(m - m'), \quad (4)$$

where we have employed the orthogonality of the Discrete Fourier Transform (DFT) and the azimuthal Fourier transform $\tilde{\mathbf{u}}_{\tau ml}(r, \theta)$ of the spherical vector waves $\mathbf{u}_{\tau ml}(k\mathbf{r}) = \tilde{\mathbf{u}}_{\tau ml}(r, \theta) e^{im\phi}$.

The Fisher information matrix (4) is decoupled over the m -index and can hence be organized as a block diagonal matrix with diagonal blocks \mathcal{I}_m with $[\mathcal{I}_m]_{\tau l, \tau' l'} = [\mathcal{I}]_{\tau ml, \tau' m' l'}$ for $-L \leq m \leq L$ where $\tau, \tau' = 1, 2$ and $l, l' = \max\{|m|, 1\}, \dots, L$. The corresponding Cramér-Rao lower bound (CRB) [Kay93] for the near-field estimation is now given by

$$\mathcal{E} \{ |\mathbf{E}^e(\mathbf{r}) - \mathbf{E}(\mathbf{r})|^2 \} \geq \sum_{m=-L}^L \sum_{\tau, \tau'=1}^2 \sum_{l, l'=\max\{|m|, 1\}}^L \frac{\tilde{\mathbf{u}}_{\tau ml}^*(r, \theta) \cdot [\mathcal{I}_m^{-1}]_{\tau l, \tau' l'} \tilde{\mathbf{u}}_{\tau' m' l'}(r, \theta)}{\|\mathbf{u}_{\tau ml}(k\mathbf{r})\|_{r=a} \|\mathbf{u}_{\tau' m' l'}(k\mathbf{r})\|_{r=a}}, \quad (5)$$

where $\mathbf{E}^e(\mathbf{r})$ denotes the estimated field. Note that the CRB in (5) is independent of the azimuthal coordinate ϕ , and depends only on (r, θ) . Let

$E^P(\mathbf{r}) = \hat{\mathbf{p}}(\mathbf{r}) \cdot \mathbf{E}(\mathbf{r})$ be an observation of the electrical field for a given polarization $\hat{\mathbf{p}}(\mathbf{r})$. Applying the DFT on the input data over the azimuthal direction so that

$$E^P(\mathbf{r}) = \frac{1}{M} \sum_{m=-M/2}^{M/2} \tilde{E}_m^P(\rho, z) e^{im\phi}. \quad (6)$$

We obtain a complex linear system of equations for each index m of the DFT,

$$\frac{1}{M} \tilde{E}_m^P(\rho, z) = \sum_{\tau=1}^2 \sum_{l=\max\{|m|, 1\}}^L f_{\tau ml} \tilde{\mathbf{u}}_{\tau ml}(r, \theta). \quad (7)$$

Here, $\hat{\mathbf{p}}$ provide two measurements of the electrical field at each point in space. Each complex linear system of equations consists of $2n$ measurement points and $2(L - \max\{|m|, 1\} + 1)$ multipole coefficients, resulting in an overdetermined system of equations if $2n \geq 2L$. Based on (7) and for each m , let \mathbf{E}_m be the matrix representation of the electrical field at the measurement points, \mathbf{U}_m the matrix representation of the normalized spherical vector waves and \mathbf{f}_m the unknown multipole coefficients. Then, the matrix representation of (7) is

$$\mathbf{E}_m = \mathbf{U}_m \mathbf{f}_m, \quad (8)$$

which is solved using the Penrose inverse of \mathbf{U}_m for each m . Observe that \mathbf{U}_m is dependent on a due to the normalization. For regularization of the system of equations, the Penrose inverse can be calculated after the singular values of \mathbf{U}_m with values below a certain tolerance level are set to zero [GL96]. The tolerance level is determined based on the noise level etc., and can be set to a value close to zero if *e.g.*, the noise level is low and many measurement points are used. From the CRB theory of a linear model and (4), the Fisher information matrix \mathcal{I}_m corresponding to \mathbf{f}_m reads

$$\frac{\sigma_n^2}{M} \mathcal{I}_m = \mathbf{U}_m^H \mathbf{U}_m. \quad (9)$$

It is clear from (9) that the singular values of \mathbf{U}_m equals the square root of the eigenvalues of $\frac{\sigma_n^2}{M} \mathcal{I}_m$.

3 Optimal Measurement Formulation

We consider designing an optimal measurement for the antenna near-field estimation. The approach is based on the theory of optimal experiments, see *e.g.*, [AD92]. In the design of the optimal measurement considered here, the measurement points \mathbf{r}_j are considered as the experiment parameters. The measurement points that are obtained from the optimization formulation are optimal in the sense that a functional of the Fisher information matrix of the multipole coefficients is maximized *i.e.*, using the optimal measurement points, the variance of the estimates of the multipole coefficients should be minimized.

Hence, we determine a set of optimal observation points by defining a constrained convex functional of the Fisher information matrix, see *e.g.*, [VPPR00]. The most common used functional is the determinant and further functionals are *e.g.*, the trace and the minimum eigenvalue [EN98]. In general, the choice of a particular functional is not obvious but some properties of functionals are given in [EN98]. Here, we employ the determinant as a first approach, which corresponds to a semi-definite optimization formulation.

Assume that there are n possible spatial observation points \mathbf{r}_j and assign to each point the probability measure $x_j \geq 0$ for $j = 1, \dots, n$. The corresponding vector decision variable is denoted $\mathbf{x} \in \mathbb{R}^n$. Let $\mathbf{G}(\mathbf{x})$ denote the Fisher information matrix corresponding to a specific measurement constellation \mathbf{x} , $\boldsymbol{\xi} \in \mathbb{C}^\nu$ the vector of complex parameters to be estimated, ν the number of parameters and $\frac{\partial \mathbf{E}(\mathbf{r}_j)}{\partial \boldsymbol{\xi}}$ the corresponding sensitivity vector, see *e.g.*, the previous model (3). Other parameters of the measurement configuration are assumed to be known *e.g.*, k and L .

The corresponding convex optimization problem of maximizing the determinant of the Fisher information matrix is then given by

$$(P1) \quad \begin{cases} \min_{\mathbf{x} \in \mathbb{R}^n} -\log \det \mathbf{G}(\mathbf{x}) \\ \mathbf{G}(\mathbf{x}) = \sum_{j=1}^n x_j \frac{\partial \mathbf{E}^*(\mathbf{r}_j)}{\partial \boldsymbol{\xi}^*} \cdot \frac{\partial \mathbf{E}(\mathbf{r}_j)}{\partial \boldsymbol{\xi}^T} \\ \mathbf{x} \geq \mathbf{0} \\ \sum_{j=1}^n x_j \leq 1 \end{cases} \quad (10)$$

We will refer to this optimization formulation as (P1). Observe that the multipole coefficients do not affect the measurement design since they appear

linearly in the optimization formulation. In a general optimal experiment design, the optimization depend on the unknown parameters of interest [Hja05].

For implementation purpose, the diagonal structure of $\mathbf{G}(\mathbf{x})$ can be utilized. Note that,

$$\frac{\partial \mathbf{E}^*(\mathbf{r}_j)}{\partial \boldsymbol{\xi}^*} \cdot \frac{\partial \mathbf{E}(\mathbf{r}_j)}{\partial \boldsymbol{\xi}^T} = \text{diag} [\mathcal{I}_{-L} \dots \mathcal{I}_0 \dots \mathcal{I}_L], \quad (11)$$

where $\mathcal{I}_m = \mathcal{I}_m(\mathbf{r}_j)$, cf., (4). The objective function in the optimization formulation then reads

$$-\log \det \mathbf{G}(\mathbf{x}) = - \sum_{m=-L}^L \log \det \mathbf{G}_m(\mathbf{x}), \quad (12)$$

where $\mathbf{G}_m(\mathbf{x}) = \sum_{j=1}^n x_j \mathcal{I}_m(\mathbf{r}_j)$.

Consider also the following formulation, referred to as (P2),

$$(P2) \left\{ \begin{array}{l} \min_{\mathbf{x} \in \mathbb{R}^n} -\log \det \mathbf{G}(\mathbf{x}) \\ \mathbf{G}(\mathbf{x}) = \sum_{j=1}^n x_j \frac{\partial \mathbf{E}^*(\mathbf{r}_j)}{\partial \boldsymbol{\xi}^*} \cdot \frac{\partial \mathbf{E}(\mathbf{r}_j)}{\partial \boldsymbol{\xi}^T} \\ \mathbf{0} \leq \mathbf{x} \leq \mathbf{1}/\gamma \\ \sum_{j=1}^n x_j \leq 1 \end{array} \right. \quad (13)$$

where γ can be used to specify the minimum number of optimal measurement points. Both P1 and P2 use the determinant of the Fisher information matrix as the objective functional. This type of formulation is termed *D-optimal* experiment design. Observe that the term M/σ_n^2 is removed from the Fisher information matrix (4) in the optimization formulations since it does not affect the solution, rather the numerical stability. Therefore, the optimal measurement points are independent of the noise power and consequently the signal-to-noise ratio. Note that if $\gamma = 1$, then P1 and P2 are essentially the same optimization problem.

We will refer to optimal measurement points (OMP) as the spatial positions \mathbf{r}_j where the corresponding $x_j \neq 0$. If a measurement point is determined optimal, a sample of the electric field is taken at this point in space.

3.1 Measurement configuration

We consider the cylindrical measurement (CM) configuration. The CM is the classic configuration where measurements of the electrical field are obtained at measurement points that describe a cylindrical surface (along the z-axis) surrounding the antenna under test (AUT). Further, we consider the extended cylindrical measurement (ECM). Here, possible measurement points are located on three different measurement surfaces, the cylinder (parallel to the z-axis) and the bottom and top of the cylinder (parallel to the ρ -axis).

For the CM and ECM, the z and the ϕ components of the electrical field (1) is calculated at the measurement points. In the CM, the measurement points are $\mathbf{r}_j = (\rho_0, z_j)$, where $|z_j| \leq z_{\max}$. For the ECM, the possible measurement points are $\mathbf{r}_j = (\rho_0, z_j)$, on the cylinder surface and $\mathbf{r}_j = (\rho_j, -z_{\max})$ and $\mathbf{r}_j = (\rho_j, z_{\max})$, on the bottom and top surfaces, respectively. The number of measurement points in the ϕ direction is $M = 120$.

The AUT is confined within a sphere of radius a , where the center of the sphere is located at $\mathbf{r} = (0, 0, 0)$ in the coordinate system used to describe the electrical field (1). For simplicity, the measurement configuration is chosen for symmetry between measurement points below and above $z = 0$.

The electrical field is constructed by synthetization of the multipole coefficients up to order L . Each coefficient $f_{\tau ml}$ is a random number obtained from a normalized complex white Gaussian distribution. The corresponding power is $P_T = \frac{1}{2\eta k^2} \sum_{\alpha} |f_{\alpha}|^2$, where $\alpha = (\tau, m, l)$ is a multi-index. Using the multipole coefficients, the corresponding electrical field is calculated and complex zero mean Gaussian noise is added. The inverse problem is solved for $a = 3\lambda, \dots, 15\lambda$, where λ is the wavelength.

As a quantitative instrument we define the error function

$$e_f(a) = \frac{1}{K} \sum_{k=1}^K \frac{\|\mathbf{f}_k - \hat{\mathbf{f}}_k(a)\|_2^2}{\|\mathbf{f}_k\|_2^2}, \quad (14)$$

where \mathbf{f}_k is the vector representation of the simulated multipole coefficients, $\hat{\mathbf{f}}_k(a)$ is the estimate of the former quantity and K is the total number of realizations used for the simulation. The error function measures the accuracy of the multipole estimation for each value of a .

Using $\hat{\mathbf{f}}_k(a)$ we can estimate the electrical field $\mathbf{E}_k^e(\mathbf{r})$ and form the error function

$$e_E(\mathbf{r}) = \frac{1}{K} \sum_{k=1}^K \frac{|\mathbf{E}_k^e(\mathbf{r}) - \mathbf{E}_k(\mathbf{r})|^2}{|\mathbf{E}_k(\mathbf{r})|^2} \quad (15)$$

where $\mathbf{r} = (a, \theta, \phi)$. Due to the symmetry in the ϕ direction of the measurement configuration and the electric field corresponding to random multipole coefficients, we can arbitrary choose $\phi = 0^\circ$ in (15). Observe that for each realization k , new multipole coefficients are obtained. The random multipole coefficients is used to model the uncertainty regarding the radiation properties of the AUT and to decrease the possibility of obtaining a simulated electrical field that is not measurable by the probe. Also, we define the signal-to-noise ratio (SNR) as

$$\text{SNR} = \frac{\max_j \{|\mathbf{E}(\mathbf{r}_j)|^2\}}{\sigma_n^2}. \quad (16)$$

As a measure of the difference in information between two measurement strategies, the optimal value of the two corresponding objective functions are used. The two measurement strategies could *e.g.*, be the OMP and the equidistant measurement points along the z-axis. The number of measurement points is N and for each equidistant measurement point the corresponding probability measure is $\mathbf{x}_L = \mathbf{1}/N$. Hence, the information measure between the OMP and the equidistant measurement points is

$$\frac{\det(\mathbf{G}(\mathbf{x}_C))}{\det(\mathbf{G}(\mathbf{x}_L))}, \quad (17)$$

where \mathbf{x}_L and \mathbf{x}_C corresponds to the probability measure vector for the equidistant measurement points and the OMP, respectively. Observe that when (17) is depicted in dB, a higher value than 0 dB corresponds to more information gained from the OMP compared to the equidistant measurement points.

Finally, since \mathcal{I} is blockdiagonal (4) and each blockmatrix \mathcal{I}_m is related to \mathbf{U}_m according to (9), the square root of the eigenvalues of $\frac{\sigma_n^2}{M}\mathcal{I}$ corresponds to the singular values of \mathbf{U}_m for all m given a . The optimization can be analyzed by comparing the singular values of \mathbf{U}_m for all m using the OMP and equidistant measurement points given a . This will also illustrate how the chosen tolerance of the Penrose inverse used in (8) affect the solution to the inverse problem of each measurement strategy.

4 Numerical Examples

In the following section we provide numerical examples that illustrate properties of the optimization and the corresponding OMP. The error functions are

presented using both OMP and equidistant measurement points as two different measurement strategies. The equidistant distribution of measurement points is a simple measurement strategy that can be easily applied. In each simulation, $K = 20$ or larger to decrease the variance of the error functions. The optimization problem is solved using YALMIP [Lof04] and SDTP3 4.0 [TTT04].

4.1 Cylindrical measurements based on P1

First, from the solution of P1 it is observed that for a given L and ρ_0 , z_{\max} can be chosen so that increasing z_{\max} further would not alter the solution of P1. The number of OMP N resulting from the solutions of P1 for different L is given in table 1. Here, we choose $z_{\max} = 40\lambda$ and $\rho_0 = 5\lambda$ so that increasing z_{\max} would not affect the result of table 1.

L	1	2	3	4	5	6	7	8	9	10	11	12	13	14	15
N	1	2	4	5	6	7	8	10	11	12	13	14	15	16	17

Table 1: The number of OMP for each order L .

Further, in the numerical experiments, we note that the number of OMP given L are equal to L , $L + 1$ or $L + 2$ depending on the settings of z_{\max} and ρ_0 . For each m , the linear system of equations (8) consists of $2(L - \max\{|m|, 1\} + 1)$ multipole coefficients, corresponding to $2N$ measurements, where we consider using measurements of two polarizations of the electrical field. The maximum number of unknown coefficients is then $2L$, (for $m = 0, \pm 1$), which is less than or equal to $2N$ as seen in table 1. Hence, number of OMP is sufficient to solve the inverse problem.

In the left figure of Fig. 1 is shown the OMP for $L = 10$, $z_{\max} = 20\lambda$ and $\rho_0 = 5\lambda$. By altering ρ_0 , the distance between the AUT and the probe is changed. The OMP at $\mathbf{r}_j = (r_j, \theta_j)$, $j = 1, \dots, N$ are invariant in θ if ρ_0 and z_{\max} are changed so that θ_j still belongs to the set of possible measurement positions. From the solution of P1 it is observed that the OMP are approximately equidistant distributed in θ . This could be expected in a spherical antenna measurement configuration but not obvious in a cylindrical configuration. Hence, further knowledge of the measurement configuration is provided by the optimization.

Let the spatial coverage in θ of the OMP along the z-axis be $\max\{\theta_j\} - \min\{\theta_j\}$. Increasing L , the spatial coverage of the OMP along the measure-

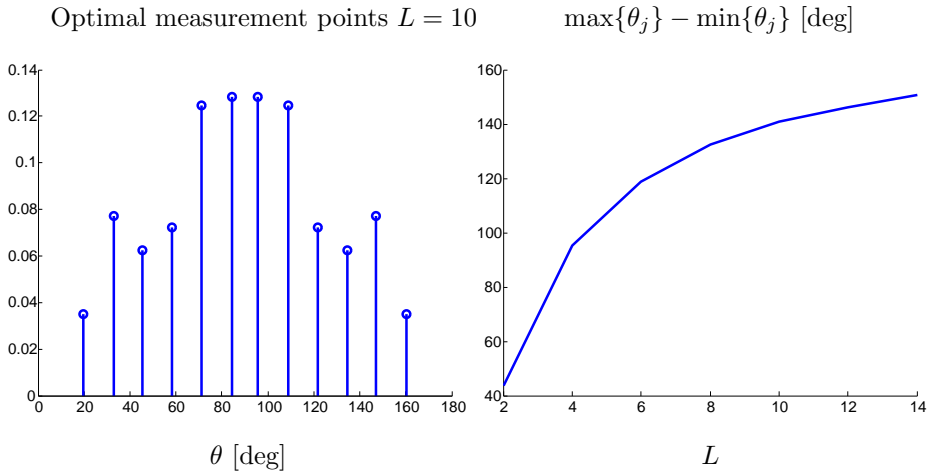


Figure 1: The left figure depicts the OMP for $L = 10$. The symmetry of the OMP around $z = 0$ and the equidistant distribution in θ is seen. The right figure depicts the spatial coverage $\max\{\theta_j\} - \min\{\theta_j\}$ as function of L .

ment axis increases. Using the OMP, $\max\{\theta_j\} - \min\{\theta_j\}$ is depicted as function of L in the right figure of Fig. 1.

Consider the near-field estimation problem using both measurement strategies. Let $z_{\max} = 20\lambda$, $\rho_0 = 5\lambda$, $\text{SNR} = 50$ dB and $L = 10$ if nothing else is stated. In the left figure of Fig. 2, e_f is depicted as function of the SNR for $a = 5\lambda, 10\lambda$ and 15λ . The solid curves correspond to the equidistant measurement points and the dashed curves correspond to the OMP.

The better result using the OMP is visible, except for $a = 5\lambda$. In this case, the corresponding curves are equal. Neither measurement strategy result in a good estimation of the multipole coefficients. Consider the singular values depicted in the right figure of Fig. 2. The horizontal dashed-dotted line indicate the tolerance level of the Penrose inverse used to solve (8). The level of the remaning error, visual in e_f for $\text{SNR} = 25$ dB and above, depend on the tolerance level.

For $a = 5\lambda$, neither measurement strategy provides singular values above the tolerance level resulting in a poor estimation performance. Although, note that the singular values corresponding to the OMP are larger. As can be seen by comparing the singular values for both measurement strategies for $a = 10\lambda$

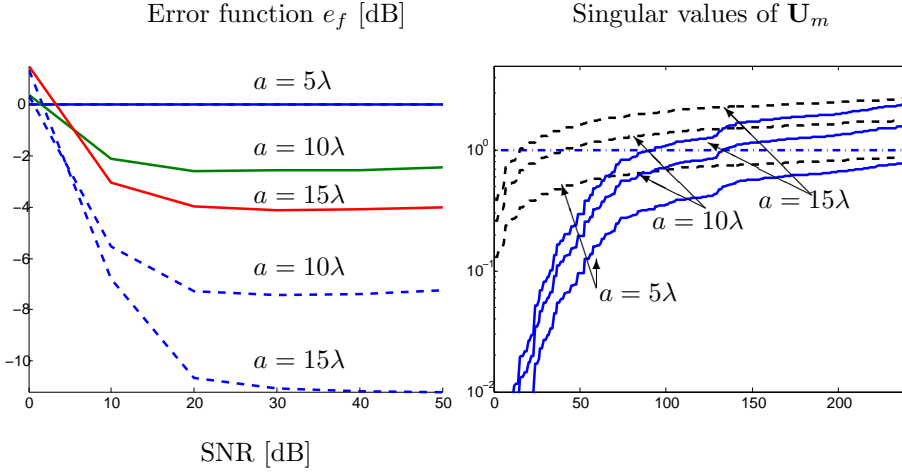


Figure 2: In the left figure, e_f is depicted as function of SNR. In the right figure, the singular values of \mathbf{U}_m for all m are depicted. Here, SNR = 50 dB and the dashed dotted vertical line corresponds to the tolerance level of the Penrose inverse. In both figures, solid curves correspond to the equidistant measurement points and dashed curves correspond to the OMP.

and $a = 15\lambda$, the OMP results in more singular values above the tolerance level and a better performance compared to the equidistant measurement points.

We point out the relation that $\log \det \mathcal{I}$ equals the sum of the logarithms of the singular values (scaled with $2\sigma_n^2/M$) of \mathbf{U}_m for all m . Hence, note that the area under respective curve in Fig. 2 is proportional to $\log \det \mathcal{I}$. The OMP increases the singular values of Fisher information matrix compared the equidistant measurement points. Hence, the optimization of the measurement configuration corresponds to deploying measurement points where maximum information regarding the parameters to be estimated can be obtained.

In the example, the SNR is high and no other errors, random or systematic, is present. Therefore, the tolerance of the Penrose inverse could be set to lower value. Here, it is not the intention to evaluate the optimal tolerance level but to analyze the properties of the optimization and the OMP. However, the tolerance level is important and is used for regularization of the inverse problem when needed, *e.g.*, for lower SNR. For clarification, if the tolerance level is set close to zero, the quality of the solution to the inverse source problem using the OMP is only dependent on the SNR.

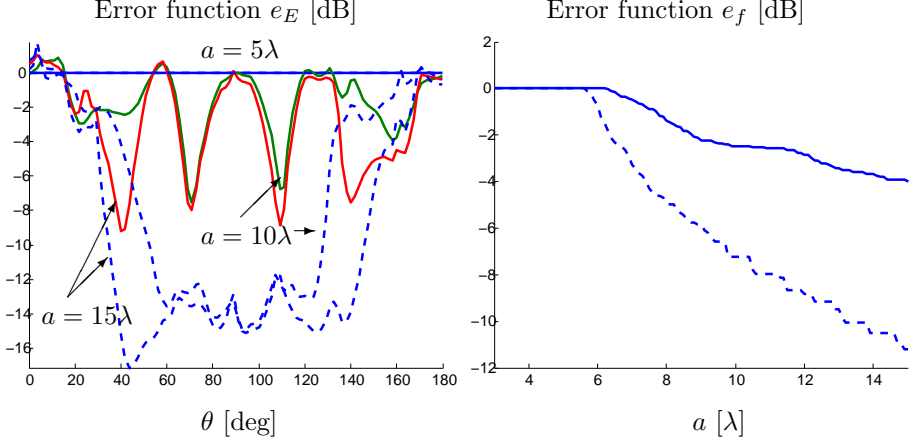


Figure 3: The left figure depicts e_E as function of θ and the right figure depicts e_f as function of a . Here, $z_{\max} = 20\lambda$, $\rho_0 = 5\lambda$, $\text{SNR} = 50$ dB and $L = 10$. In both figures, the solid curves correspond to the equidistant measurement points and the dashed curves correspond to the OMP. In the left figure, for $a = 5\lambda$ the two curves are equal.

The singular values depicted in Fig. 2 are dependent on the optimal measurement points and therefore independent of the SNR. Also, based on the CRB theory of a linear model, the variance of the estimated electrical field is close to the CRB when the tolerance level is such that no singular values are set to zero when the Penrose inverse is calculated.

In Fig. 3, the result of the near-field estimation is provided. The number of OMP and equidistant measurement points is $N = 12$, and are shown in Fig. 1. The estimation result is predicted by the analysis of the singular values in Fig. 2, *e.g.*, for $a = 5\lambda$ neither measurement strategy provide an acceptable solution since the tolerance level is set too high. A proper setting of the tolerance level could be 0.1 in this case.

4.2 Extended cylindrical measurement based on P1

As a final example, consider an extension to the CM, where two additional measurement surfaces are added *i.e.*, a top and a bottom surface is added to the CM configuration to obtain the ECM.

Consider a measurement configuration where $z_{\max} = \rho_0$ since if $z_{\max} \gg \rho_0$ there is little to gain from the ECM compared to the CM. Also, let the SNR = 30 dB.

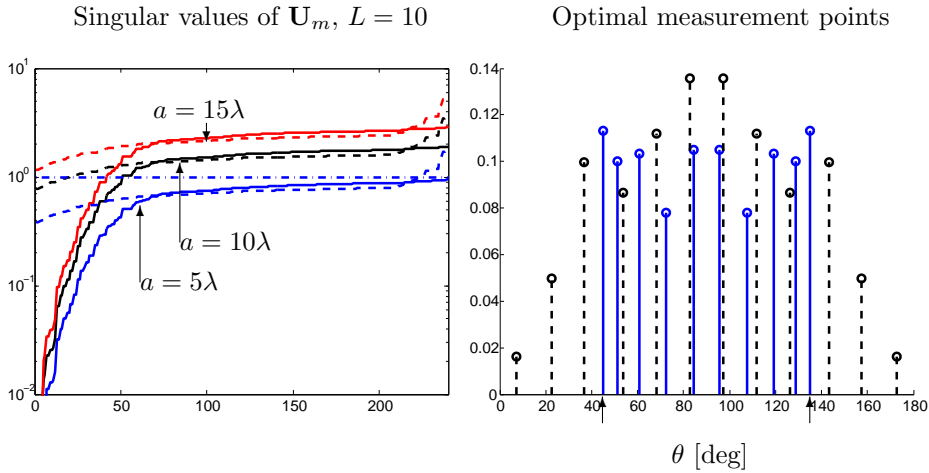


Figure 4: The singular values of \mathbf{U}_m for all m is depicted in the left figure. The corresponding OMP for CM and ECM are depicted in the right figure. In both figures, the solid and dashed curves correspond to CM and ECM, respectively. In the left figure, the horizontal dashed dotted line corresponds to the tolerance level. In the right figure, the vertical arrows indicate the separation between the measurement surfaces. In both figures $z_{\max} = \rho_0 = 5\lambda$.

In the left figure of Fig. 4 is shown the singular values of \mathbf{U}_m for all m . The corresponding OMP for the ECM and the CM are depicted in the right figure of Fig. 4. In both figures, the solid curves correspond to the CM and the dashed curves correspond to the ECM. Observe in the left figure, the OMP of the ECM results in increased singular values. For $\rho_0 = 5\lambda$ and $a = 10\lambda, 15\lambda$, the gain of the ECM is due to the number of singular values

above the tolerance level compared to the CM. Specifically, for $\rho_0 = 5\lambda$ and $a = 15\lambda$ all singular values are above the tolerance level. The OMP of the ECM are approximately equidistant distributed in θ and three measurement points are located on the bottom and top surface, respectively.

For $\rho_0 = 5\lambda$, the corresponding error functions are depicted in Fig. 5.

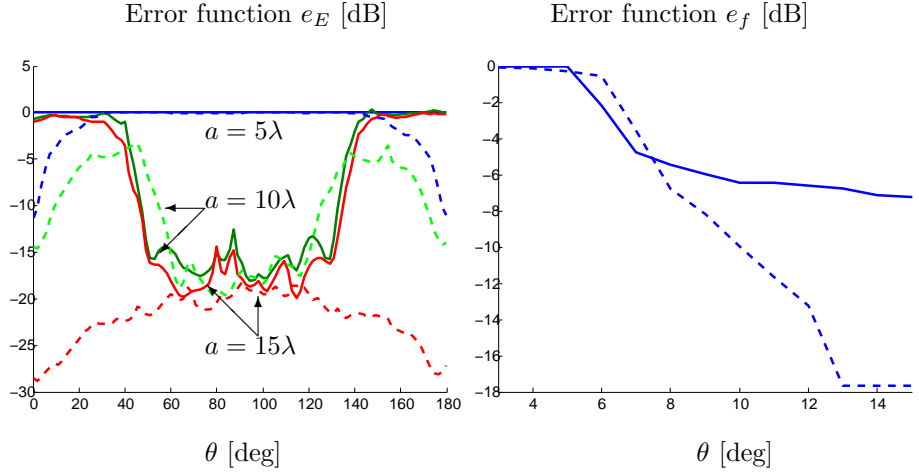


Figure 5: The left figure depict e_E as function of θ for CM and ECM. The right figure depict e_f as function of a . In both figures, the solid curves and the dashed curves correspond to the CM and the ECM, respectively

In the left figure of Fig. 5 is e_E depicted for $a = 5\lambda, 10\lambda, 15\lambda$. Observe that for ECM and $a = 15\lambda$, the error is seen to be very small, which is consistent with all singular values above the tolerance level. In this situation, due to the OMP the tolerance level has no effect on the solution.

In Fig. 6, the mean-square error of the estimated electric field is depicted. The mean-square error corresponds to e_E (15) without the normalization. For the ECM and $a = 15\lambda$, the corresponding CRB is depicted (dashed dotted curve).

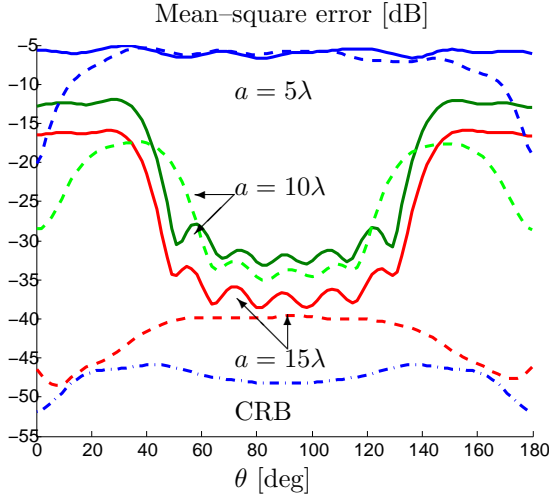


Figure 6: Mean-square error of the estimated electrical field and the corresponding CRB for the ECM when $a = 15\lambda$. The solid and dashed curves correspond to the CM and the ECM, respectively.

4.3 Cylindrical measurements based on P2

The optimization formulation P2 is an alternative formulation to P1 that adds some control of the number of measurement points that should be obtained. While P1 is formulated without constraints on the number of measurement points and return almost a minimum number of OMP, P2 has the parameter γ that can be used to control the minimum number of OMP. It will be illustrated here that although the number of OMP increases, the difference in performance between the two measurement strategies is decreased. Here, $z_{\max} = 20\lambda$ and $\rho_0 = 10\lambda$. In the left figure of Fig. 7, (17) is depicted for different values of N . Also, the corresponding plot of (17) using P1 is included for comparison. As N increases the information measure of (17) decreases. In the right figure of Fig. 7, e_f is depicted. Due to the increased number of measurement points, the differences in e_f between the two measurement strategies are less prominent, compare to the left figure of Fig. 2 in the case of P1. Here, the threshold SNR is approximately 10 – 15 dB, a lower value than in the case P1 since here more measurement points are used.

An example of a near-field estimation follows. Consider $z_{\max} = 20\lambda$, $\rho_0 = 10\lambda$, SNR = 50 dB and $L = 10$ if nothing else is stated. The estimation is

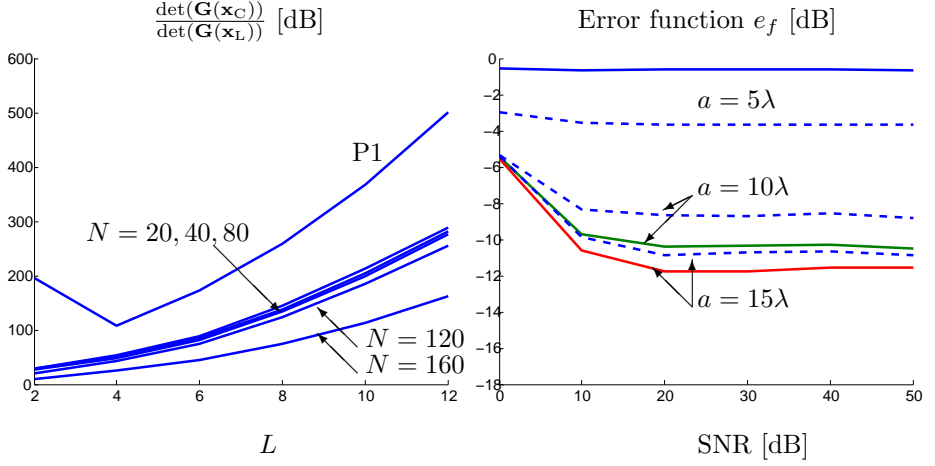


Figure 7: In the left figure, (17) is depicted as function of L . In the right figure, e_f is depicted as function of SNR for equidistant measurement points (solid curves) and OMP (dashed curves) for $N = 80$.

made using 80 measurement points. For comparison, the OMP are depicted in Fig 8 for both P1 (left figure) and P2 (right figure). Observe that for $z_{\max} = 20\lambda$ and $\rho_0 = 10\lambda$, the number of OMP $N = 11$ in P1. Observe the concentration of OMP in P2 (right figure) around the positions of the OMP in P1.

Next, in Fig. 9, e_E is depicted for $a = 5\lambda, 10\lambda, 15\lambda$ (left figure) and the corresponding e_f (right figure). The solid curves correspond to equidistant measurement points and the dashed curves correspond to the OMP. Note that for $a = 5\lambda$, the OMP improves the result of the inverse problem compared to the equidistant measurement points, see left figure of e_E . For higher values of a the two measurement strategies have similar performance. In the right figure of Fig. 9, the error function e_f corresponding to the OMP is larger than the error function of the equidistant measurement points for a larger than 6λ . The value of a , for which the two measurement strategies have equal value of e_f depends on the number of measurement points. Less measurement points would move the crossing to higher values of a .

Consider the singular values in Fig. 10. For $a = 5\lambda$, the OMP corresponds to more singular values above the tolerance level. Hence, the estimation per-

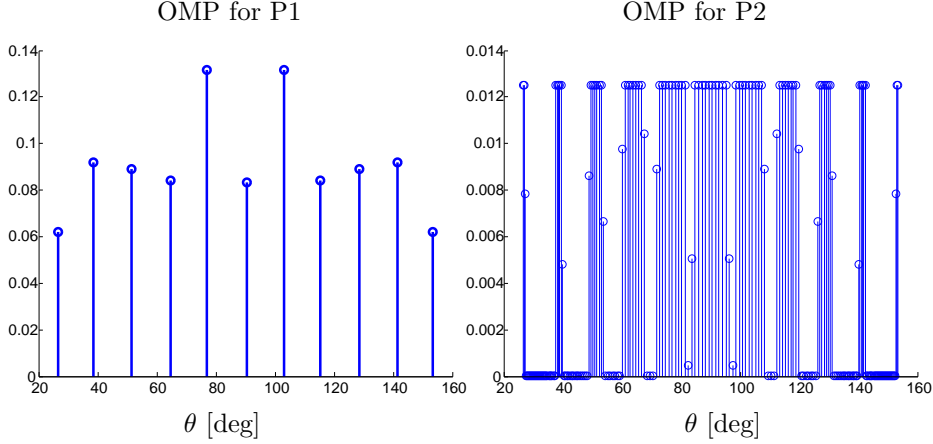


Figure 8: Optimal measurement points for $L = 10$, $z_{\max} = 20\lambda$ and $\rho_0 = 10\lambda$. In the left figure is shown the OMP for P1 and in the right figure, the OMP for P2 when $N = 80$.

formance using the OMP is improved over the equidistant measurement points as is seen in Fig. 8. For the two remaining a , the OMP corresponds to less singular values above the tolerance level although some of the singular values are larger than the corresponding singular values for the equidistant measurement points. Comparing the area below each of the curves, the OMP provides a slightly larger area compared to the equidistant points. This indicates that the determinant of the Fisher information matrix is larger for the OMP.

The solution to the inverse source problem is strongly dependent on the number of singular values above the tolerance level. Hence, in this case, the requirement of more OMP might not be an appropriate formulation for the quality of the solution to the inverse problem. Since many measurement points are to be used, the gain of the optimization P2 and the corresponding OMP will diminish. Simply using the equidistant measurement points might therefore be the appropriate measurement strategy when the number of measurement points are large.

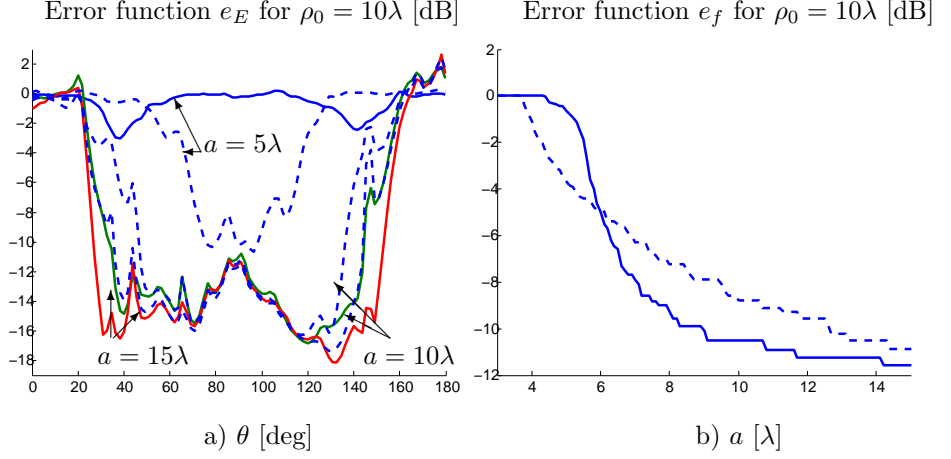


Figure 9: In the left figure, e_E is depicted for the equidistant measurement points (solid curves) and the OMP (dashed curves). In the right figure, the corresponding e_f is depicted as function of a .

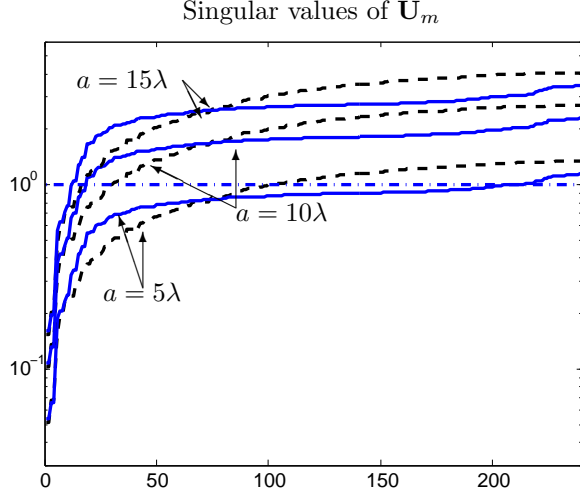


Figure 10: The singular values of \mathbf{U}_m for all m . The solid curves correspond to equidistant measurement points, the dashed curves correspond to the OMP and the dashed dotted vertical line indicate the tolerance level of the Penrose inverse.

Consider increasing the number of optimal measurement points N at the cost of increased noise. The noise variance is proportional to the number of measurement points used, $\sigma_n^2 = N \frac{\max_j \{|\mathbf{E}(r_j)|^2\}}{\text{SNR}}$. In Fig. 11, e_f is depicted as function of N for $z_{\max} = 20\lambda$, $\rho_0 = 10\lambda$ and $\text{SNR} = 30$ dB. Here, $a = 5\lambda$ and

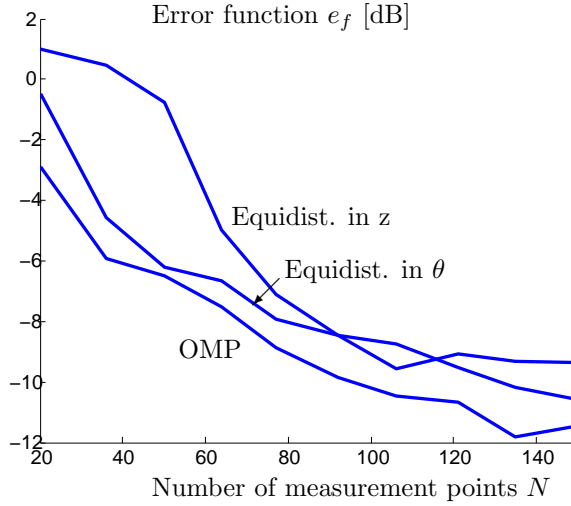


Figure 11: The figure depicts e_f as function of N when the applied noise is proportional to the number of measurement points.

the OMP will therefore produce a better result compared to the equidistant measurement points. Increasing the number of measurement points improves the result of the estimation to a certain degree. Using the scaling of the noise variance enables comparison of e_f for different values of N . For comparison, equidistant measurement points in θ is included. This measurement strategy corresponds well to the OMP strategy. (For a given level of e_f , *e.g.*, -6 dB, the OMP corresponds to $N \approx 40$ compared to $N \approx 80$ for equidistant measurement points.)

5 Summary and Conclusions

Cylindrical antenna near-field measurements have been designed as optimal experiments. We have formulated the optimal measurement configuration based on the Fisher information matrix that provides details regarding the estimation performance of the multipole coefficients. The optimal measurement points are obtained from the solution of two separate semi-definite optimization formulations, respectively. Properties of the solution to the inverse problem have been studied for both the optimal measurement points and equidistant measurement points.

The first optimization formulation P1 provides close to a minimum number of measurement points sufficient to solve the inverse problem. In the second optimization formulation P2, the number of measurement points are increased resulting in a decrease in estimation performance using the optimal measurement points compared to the equidistant measurement points.

A singular value analysis is used to interpret the result of the optimization and the properties of the solution to the inverse problem. Numerical examples include an extended cylindrical measurement where a complete measurement of the electrical field can be obtained.

References

- [ACM06] M. Alam, V. Cevher, and J.H. McClellan. Optimal experiments with seismic sensors. In *IEEE International Conference on Acoustics, Speech and Signal Processing*, volume 4, pages IV–1145–IV–1148, 2006.
- [AD92] A. Atkinson and A. Doner. *Optimum Experiment Design*. Clarendon Press, Oxford, 1992.
- [AW01] G. B. Arfken and H. J. Weber. *Mathematical Methods for Physicists*. Academic Press, New York, fifth edition, 2001.
- [EN98] A. F. Emery and A. V. Nenarokomov. Optimal experiment design. *Measurement Science and Technology*, 9(6):864–876, 1998.
- [Fed72] V. Fedorov. *Theory of Optimal Experiments*. Academic Press, New York, 1972.
- [GL96] G. H. Golub and C. F. Van Loan. *Matrix Computations*. The John Hopkins University Press, 1996.

-
- [Han88] J. E. Hansen, editor. *Spherical Near-Field Antenna Measurements*. Number 26 in IEE electromagnetic waves series. Peter Peregrinus Ltd., Stevenage, UK, 1988. ISBN: 0-86341-110-X.
- [Hja05] H. Hjalmarsson. From experiment design to closed-loop control. *Automatica*, 41(3):393–438, 2005.
- [Jac75] J. D. Jackson. *Classical Electrodynamics*. John Wiley & Sons, New York, second edition, 1975.
- [Kay93] S. M. Kay. *Fundamentals of Statistical Signal Processing, Estimation Theory*. Prentice-Hall, Inc., NJ, 1993.
- [Lai05] T. Laitinen. *Advanced Spherical Antenna Measurements*. Ph.d. thesis, Helsinki University of Technology, Finland, 2005.
- [Lof04] J. Lofberg. YALMIP : a toolbox for modeling and optimization in MATLAB. In *IEEE International Symposium on Computer Aided Control Systems Design*, pages 284–289, 2004.
- [LSL02] T. Long, Z. Sun, and C. Li. Optimal experiment design for wavelet-based system identification. *Proceedings of the 4th World Congress on Intelligent Control and Automation, 2002*, 1:89–93, 2002.
- [NG05] S. Nordebo and M. Gustafsson. Multichannel broadband Fano theory for arbitrary lossless antennas with applications in DOA estimation. In *2005 IEEE International Conference on Acoustics, Speech, and Signal Processing*. IEEE Signal Processing Society, 2005.
- [NG06a] S. Nordebo and M. Gustafsson. On the design of optical measurements for antenna near-field imaging problems. In *AIP Conference Proceeding, 2nd Conference on Mathematical Modelling of Wave Phenomena*, volume 834, pages 234–249, 2006.
- [NG06b] S. Nordebo and M. Gustafsson. Statistical signal analysis for the inverse source problem of electromagnetics. *IEEE Transactions on Signal Processing*, 54(6):2357–2362, 2006.
- [NGP07] S. Nordebo, M. Gustafsson, and K. Persson. Sensitivity analysis for antenna near-field imaging. *IEEE Transactions on Signal Processing*, 55(1):94–102, 2007.

- [PG05] K. Persson and M. Gustafsson. Reconstruction of equivalent currents using a near-field data transformation - with radome applications. *Progress in Electromagnetics Research*, 54:179–198, 2005.
- [PLP93] K. Paulson, W. Lionheart, and M. Pidcock. Optimal experiments in electrical impedance tomography. *IEEE Transactions on Medical Imaging*, 12(4):681–686, 1993.
- [RS04] G.F. Ricciardi and W.L. Stutzman. A near-field to far-field transformation for spheroidal geometry utilizing an eigenfunction expansion. *IEEE Transactions on Antennas and Propagation*, 52(12):3337–3349, 2004.
- [SXC05] J. Shihao, L. Xuejun, and L. Carin. Adaptive multiaspect target classification and detection with hidden markov models. *IEEE Sensors Journal*, 5(5):1035–1042, 2005.
- [TTT04] K.C. Toh, R.H. Tutuncu, and M.J. Todd. On the implementation of SDPT3 (version 3.1) - a MATLAB software package for semidefinite-quadratic-linear programming. In *IEEE International Symposium on Computer Aided Control Systems Design*, pages 290–296, 2004.
- [VB99] L. Vandenberghe and S. Boyd. Applications of semidefinite programming. *Applied Numerical Mathematics*, 29(3):283–299, 1999.
- [VBW98] L. Vandenberghe, S. Boyd, and S. Wu. Determinant maximization with linear matrix inequality constraints. *SIAM Journal on Matrix Analysis and Applications*, 19(2):499–534, 1998.
- [VPPR00] A. Vande Wouwer, N. Point, S. Porteman, and M. Remy. An approach to the selection of optimal sensor locations in distributed parameter systems. *Journal of Process Control*, 10(4):291–300, 2000.
- [WGF06] J. S. Welsh, G. C. Goodwin, and A. Feuer. Evaluation and comparison of robust optimal experiment design criteria. In *American Control Conference, 2006*, 2006.
- [XC04] L. Xuejun and L. Carin. Application of the theory of optimal experiments to adaptive electromagnetic-induction sensing of buried targets. *IEEE Transactions on Pattern Analysis and Machine Intelligence*, 26(08):961–972, 2004.

PART IV

**Statistical Analysis of a
Digital Directional Coupler
for Transmission Line
Measurements**

Part IV is submitted as:

J. Lundbäck and S. Nordebo, "Statistical Analysis of a Digital Directional Coupler for Transmission Line Measurements", submitted to *IEEE Transactions on Circuits and Systems I*.

Statistical Analysis of a Digital Directional Coupler for Transmission Line Measurements

J. Lundbäck and S. Nordebo

Abstract

This paper describes the fundamental properties of a Digital Directional Coupler (DDC) that separates forward and backward propagating waves on a transmission line. The DDC is based on two independent wide-band measurements of voltage and current and a frequency domain digital wave splitting using the FFT. A practical procedure is described for calibration of the digital processor with respect to the particular transmission line and the voltage and current sensors that is employed. The Cramér-Rao lower bound is used as a statistical tool to analyze the fundamental performance of the DDC. Important parameters are identified and investigated *e.g.*, the signal-to-noise ratio in the calibration procedure, the characteristic impedance of the transmission line and the frequency transfer functions of the voltage and current sensors. In order to illustrate the wave splitting ability of the DDC, an experiment has been conducted where a DDC has been implemented and tested and the experimental results are compared with the theoretical models.

1 Introduction

Wave splitting or separation of forward and backward propagating waves is incorporated in many applications *e.g.*, as a part of a vector network analyzer [Poz98]. The wave splitting is commonly achieved by a directional coupler designed as a hardware module whose properties are directly linked to the electromagnetic coupling effects within the module. However, these coupling effects are usually very difficult to control and it is a non-trivial task to design a directional coupler that maintains high performance (isolation and directivity) over an appreciable bandwidth, see *e.g.*, [Poz98, MYJ80].

There are several applications that could benefit from the functionality of a directional coupler for transmissions lines *e.g.*, fault localization and partial

discharge (PD) monitoring on power lines, see *e.g.*, [PSH⁺99, Vee05]. Another interesting application area is with the transient based protection techniques for power transmission systems [Bo00]. However, installing a separate device on a transmission line could be difficult or hazardous, especially for medium-voltage or high-voltage power lines. A more easy and accessible way is to install and utilize conventional current and voltage sensors and perform the wave splitting by digital means.

The ongoing research on on-line PD diagnostics has produced several apparatus that has been commercially available *e.g.* [SHV91, Mas00]. The use of advanced signal processing has been extensively applied, especially since the cost of processing power has decreased. Continuous monitoring combined with a long-term history can provide early warnings and indications of degradations in the power cable system. Clearly, a directional coupler for power lines with good isolation properties can be very useful for discriminating between transients, pulses, PD phenomena etc., which are emanating from different locations in the power cable network [PSH⁺99].

Noise and interference mitigation is another fundamental problem in any PD monitoring or transient based protection system, see *e.g.*, [SSS00, LPP03]. As the interference includes many components of different nature *e.g.*, wide-band background noise, narrowband interference and pulse-shaped disturbances, see *e.g.* [LPP03, BD00, And98], many different noise reduction techniques have been proposed including filtering, spectral analysis and wavelets analysis, see *e.g.*, [VW03, AS98, KG05]. Clearly, a directional coupler for power lines with good isolation properties can be very useful for efficient reduction of any exterior noise emanating from locations other than that under investigation.

A Fisher information analysis and the Cramér-Rao lower bound [Kay93] provides a very useful instrument for sensitivity analysis of various wave propagation phenomena, and which facilitates valuable physical interpretations, see *e.g.*, [DT91, TD91, NB99, DN01, Col05, Smi05, NG06, GN06].

In this paper, we describe a statistical signal analysis of a Digital Directional Coupler (DDC) that separates forward and backward propagating waves on a transmission line. In the literature, we have found only one reference to a Digital Directional Coupler (DDC) in the context of digital optical switches [Sym92]. However, the theory and application in [Sym92] is not similar to the work done herein. The Digital Directional Coupler (DDC) considered here is based on two independent wide-band measurements of voltage and current on a transmission line, and a frequency domain digital wave splitting using the FFT. A practical procedure is described for calibration of the

digital processor with respect to the particular transmission line and the voltage and current sensors that are employed. A similar technique is given in [PE03] for measurement of the propagation constant of a power cable.

A statistical model for the calibration and operation of the DDC is given. The Cramér-Rao lower bound is used as a statistical tool to analyze the corresponding isolation and directivity [Poz98] properties in terms of the sensor signal quality. Important parameters are identified and investigated *e.g.*, the signal-to-noise ratio in the calibration procedure, the characteristic impedance of the transmission line and the frequency transfer functions of the voltage and current sensors.

An experiment has been conducted in order to illustrate the calibration process of the DDC and to show that a DDC can be designed to operate over an appreciable bandwidth using very simple and low cost sensors. The rest of the paper is outlined as follows. In section 2 the digital directional coupler is introduced and the calibration procedure is described. In section 3 a statistical analysis of the performance of the DDC is provided. In section 4 an experiment is described where a DDC has been designed and implemented using a standard coaxial antenna cable. The resulting performance of the DDC is compared to the performance predicted by the statistical analysis.

2 The Digital Directional Coupler

2.1 Wave propagation model

The one-dimensional electric voltage $V(x)$ and current $I(x)$ on a single-mode transmission line can be represented by

$$\begin{cases} V(x) = V^+ e^{-\gamma x} + V^- e^{\gamma x} \\ I(x) = \frac{V^+}{Z} e^{-\gamma x} - \frac{V^-}{Z} e^{\gamma x} \end{cases} \quad (1)$$

where V^+ and V^- are the complex amplitudes associated with forward and backward propagating waves, γ the complex propagation constant, x the length dimension and Z the characteristic impedance of the transmission line, see *e.g.*, [Poz98]. Note that all wave parameters are here described in the frequency domain. The mapping between the total voltage $V = V(0)$ and current $I = I(0)$ and the wave amplitudes V^+ and V^- at the transmission

line input is then given by

$$\begin{pmatrix} V^+ \\ V^- \end{pmatrix} = \begin{pmatrix} \frac{1}{2} & \frac{1}{2}Z \\ \frac{1}{2} & -\frac{1}{2}Z \end{pmatrix} \begin{pmatrix} V \\ I \end{pmatrix}. \quad (2)$$

Assume now that two decoupled sensors are available measuring the voltage V and current I as

$$\begin{cases} u = AV \\ v = BI \end{cases} \quad (3)$$

where A and B are the corresponding sensor frequency functions, *cf.*, also Fig. 1. Then there is a linear, one-to-one relationship between the measured signals u and v and the wave amplitudes V^+ and V^- given by

$$\begin{pmatrix} V^+ \\ V^- \end{pmatrix} = \begin{pmatrix} a & b \\ a & -b \end{pmatrix} \begin{pmatrix} u \\ v \end{pmatrix} \quad (4)$$

where $a = \frac{1}{2A}$ and $b = \frac{Z}{2B}$.

2.2 Calibration procedure

Consider the calibration set-up in Fig. 1. The device under test (DUT) is an open ended transmission line of length l_1 , characteristic impedance Z and complex propagation constant γ . Two sensors are applied to the left side of the DUT measuring the voltage $u = AV$ and current $v = BI$ on the cable input. The calibration set-up consists further of a pulse generator with voltage \mathcal{E}_g and generator resistance R , a matched power splitter with transmission coefficient T and auxiliary coaxial cables of length l_0 and l with characteristic impedance R and propagation constant $\gamma_0 = i\omega/c_0$ where c_0 is the speed of wave propagation. A measurement voltage V_m is obtained over the load resistance R via the power splitter as depicted in Fig. 1. The voltage reflections and transmissions at the indicated reference plane in Fig. 1 is given by the scattering formulation

$$\begin{pmatrix} V_1^- \\ V_2^+ \end{pmatrix} = \begin{pmatrix} \Gamma^+ & 1 - \Gamma^+ \\ 1 + \Gamma^+ & -\Gamma^+ \end{pmatrix} \begin{pmatrix} V_1^+ \\ V_2^- \end{pmatrix} \quad (5)$$

where

$$\Gamma^+ = \frac{Z - R}{Z + R}. \quad (6)$$

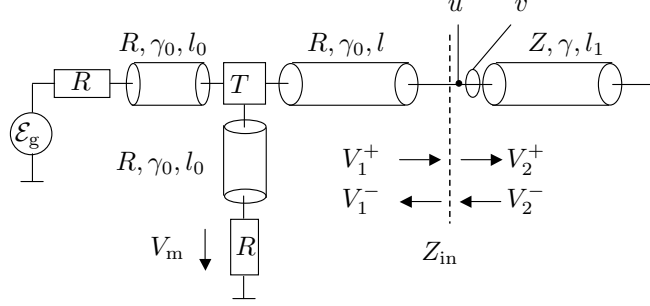


Figure 1: Calibration set-up with open ended transmission line.

The total input impedance of the open ended transmission line as seen from the left at the reference plane is $Z_{in} = Z \coth \gamma l$ and the corresponding reflection coefficient is hence given by

$$\Gamma = \frac{Z_{in} - R}{Z_{in} + R} = \frac{\Gamma^+ + e^{-\gamma 2l}}{1 + e^{-\gamma 2l} \Gamma^+} = \Gamma^+ + e^{-\gamma 2l} (1 - \Gamma^{+2}) + \dots \quad (7)$$

yielding the reflected voltage $V_1^- = V_1^+ \Gamma$. The incident wave at the reference plane is given by

$$V_1^+ = \frac{\mathcal{E}_g}{2} e^{-\gamma_0(l+l_0)} T \quad (8)$$

and the corresponding first order pulses are hence given by

$$\begin{cases} V_1^{-(1)} = V_1^+ \Gamma^+ \\ V_2^{+(1)} = V_1^+ (1 + \Gamma^+). \end{cases} \quad (9)$$

The observed pulses at the measurement resistor are given by

$$\begin{cases} V_m^{(0)} = \frac{\mathcal{E}_g}{2} e^{-\gamma_0 2l_0} T \\ V_m^{(1)} = V_1^{-(1)} e^{-\gamma_0(l+l_0)} T \end{cases} \quad (10)$$

and it is found that $V_1^+ = V_m^{(0)} e^{-\gamma_0(l-l_0)}$. The reflection coefficient Γ^+ can be obtained from a short circuit measurement where $V_1^{-(s)} = -V_1^+$ and $V_m^{(s)} =$

$V_1^{-(s)} e^{-\gamma_0(l+l_0)} T$, and hence

$$\Gamma^+ = \frac{V_1^{-(1)}}{V_1^+} = -\frac{V_1^{-(1)}}{V_1^{-(s)}} = -\frac{V_m^{(1)}}{V_m^{(s)}}. \quad (11)$$

The parameters a and b are obtained from the calibration equations

$$\begin{cases} V_2^{+(1)} &= au^{(1)} + bv^{(1)} \\ 0 &= au^{(1)} - bv^{(1)} \end{cases} \quad (12)$$

with the straightforward solution

$$\begin{cases} a = \frac{V_2^{+(1)}}{2u^{(1)}} \\ b = \frac{V_2^{+(1)}}{2v^{(1)}} \end{cases} \quad (13)$$

where $u^{(1)}$ and $v^{(1)}$ correspond to the first pulses of u and v , respectively. See also Fig. 2 which shows a timing diagram for the calibration procedure. Note that the assumption $u^{(1)} = AV = AV_2^{+(1)}$ and $v^{(1)} = BI = BI_2^{+(1)} = BV_2^{+(1)}/Z$ yields the correct answer $a = \frac{1}{2A}$ and $b = \frac{Z}{2B}$. The calibration procedure can now be summarized by the following operations

$$\begin{cases} \Gamma^+ &= -\frac{V_m^{(1)}}{V_m^{(s)}} \\ V_2^{+(1)} &= V_m^{(0)} e^{-\gamma_0(l-l_0)} (1 + \Gamma^+) \\ a &= \frac{V_2^{+(1)}}{2u^{(1)}} \\ b &= \frac{V_2^{+(1)}}{2v^{(1)}}. \end{cases} \quad (14)$$

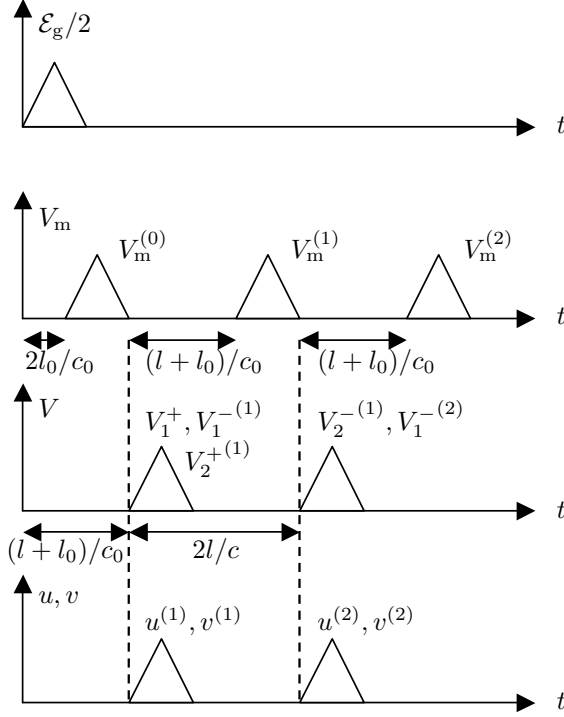


Figure 2: Timing diagram for the calibration procedure. Note that it is only the first order pulses that are employed in the calibration.

3 Statistical Analysis

Let \hat{a} and \hat{b} denote estimates of the parameters a and b according to the measurement model given in (4). The estimated wave amplitudes are thus given by

$$\begin{pmatrix} \hat{V}^+ \\ \hat{V}^- \end{pmatrix} = \begin{pmatrix} \hat{a} & \hat{b} \\ \hat{a} & -\hat{b} \end{pmatrix} \begin{pmatrix} u \\ v \end{pmatrix}. \quad (15)$$

Using (2) and (3) with $A = \frac{1}{2a}$ and $B = \frac{Z}{2b}$, the estimation (15) is given by

$$\begin{cases} \hat{V}^+ = \left(\hat{a} \frac{1}{2a} + \hat{b} \frac{1}{2b} \right) V^+ + \left(\hat{a} \frac{1}{2a} - \hat{b} \frac{1}{2b} \right) V^- \\ \hat{V}^- = \left(\hat{a} \frac{1}{2a} - \hat{b} \frac{1}{2b} \right) V^+ + \left(\hat{a} \frac{1}{2a} + \hat{b} \frac{1}{2b} \right) V^- \end{cases} \quad (16)$$

The cross-coupling V_{cc} is given by

$$V_{cc} = \hat{a} \frac{1}{2a} - \hat{b} \frac{1}{2b} = \Delta a \frac{1}{2a} - \Delta b \frac{1}{2b} \quad (17)$$

and the coupling V_c

$$V_c = \hat{a} \frac{1}{2a} + \hat{b} \frac{1}{2b} = \Delta a \frac{1}{2a} + \Delta b \frac{1}{2b} + 1 \quad (18)$$

where $\Delta a = \hat{a} - a$ and $\Delta b = \hat{b} - b$.

Using standard definitions from microwave technology [Poz98], the *coupling*, *directivity* and *isolation* (in dB) can be obtained for the DDC,

$$C = -20 \log(|V_c|), \quad (19)$$

$$D = 20 \log \left(\left| \frac{V_c}{V_{cc}} \right| \right), \quad (20)$$

$$I = -20 \log(|V_{cc}|), \quad (21)$$

respectively, where $I = D + C$. An ideal directional coupler has infinite isolation and directivity corresponding to $V_{cc} = 0$ and perfect coupling, *i.e.*, $V_c = 1$. Furthermore, for unbiased estimators it is readily seen that $\mathcal{E}\{V_{cc}\} = 0$ and $\mathcal{E}\{V_c\} = 1$ where $\mathcal{E}\{\cdot\}$ denotes the expectation operator.

Based on (14), the following non-linear statistical measurement model is now introduced

$$\begin{cases} x_1 = V_m^{(1)} + n_1 = -V_m^{(s)} \Gamma^+ + n_1 \\ x_2 = V_m^{(s)} + n_2 \\ x_3 = V_m^{(0)} + n_3 \\ x_4 = u^{(1)} + n_4 = \frac{1}{2a} V_m^{(0)} e^{-\gamma_0(l-l_0)} (1 + \Gamma^+) + n_4 \\ x_5 = v^{(1)} + n_5 = \frac{1}{2b} V_m^{(0)} e^{-\gamma_0(l-l_0)} (1 + \Gamma^+) + n_5 \end{cases} \quad (22)$$

where the five unknown and independent variables are a , b , Γ^+ , $V_m^{(0)}$ and $V_m^{(s)}$ and n_i denotes uncorrelated zero mean complex Gaussian noise with variance

$\sigma_1^2 = \sigma_2^2 = \sigma_3^2 = \sigma^2$, σ_4^2 and σ_5^2 for $i = 1, \dots, 5$. Assuming that there is no noise present, we can see that the solution to (22) is given by

$$\begin{cases} V_m^{(s)} &= x_2 \\ \Gamma^+ &= -\frac{x_1}{V_m^{(s)}} \\ V_m^{(0)} &= x_3 \\ a &= \frac{1}{2x_4} V_m^{(0)} e^{-\gamma_0(l-l_0)} (1 + \Gamma^+) \\ b &= \frac{1}{2x_5} V_m^{(0)} e^{-\gamma_0(l-l_0)} (1 + \Gamma^+). \end{cases} \quad (23)$$

We consider two different statistical models related to (22).

Deterministic excitation. The excitation variables $V_m^{(0)}$ and $V_m^{(s)}$ are independent deterministic parameters. The unknown parameter vector is denoted $\boldsymbol{\theta} = [a \ b \ \Gamma^+ \ V_m^{(0)} \ V_m^{(s)}]^T$. The cross-coupling is given by $V_{cc} = \boldsymbol{\eta}_1^H (\hat{\boldsymbol{\theta}} - \boldsymbol{\theta})$ and the coupling is $V_c - 1 = \boldsymbol{\eta}_2^H (\hat{\boldsymbol{\theta}} - \boldsymbol{\theta})$ where $\boldsymbol{\eta}_1^H = [\frac{1}{2a} \ -\frac{1}{2b} \ 0 \ 0 \ 0]$ and $\boldsymbol{\eta}_2^H = [\frac{1}{2a} \ \frac{1}{2b} \ 0 \ 0 \ 0]$. The Cramér-Rao lower bounds (CRB) [Kay93] for V_{cc} and V_c are given by

$$\mathcal{E} \{|V_{cc}|^2\} \geq \boldsymbol{\eta}_1^H \boldsymbol{\mathcal{I}}^{-1}(\boldsymbol{\theta}) \boldsymbol{\eta}_1, \quad (24)$$

$$\mathcal{E} \{|V_c - 1|^2\} \geq \boldsymbol{\eta}_2^H \boldsymbol{\mathcal{I}}^{-1}(\boldsymbol{\theta}) \boldsymbol{\eta}_2, \quad (25)$$

where $\boldsymbol{\mathcal{I}}(\boldsymbol{\theta})$ is the Fisher information matrix given by

$$\boldsymbol{\mathcal{I}}(\boldsymbol{\theta}) = \frac{\partial \boldsymbol{\mu}^H}{\partial \boldsymbol{\theta}^*} \mathbf{R}^{-1} \frac{\partial \boldsymbol{\mu}}{\partial \boldsymbol{\theta}^T} \quad (26)$$

where $(\cdot)^*$ denotes complex conjugation, $(\cdot)^T$ transpose, $(\cdot)^H$ Hermitian transpose, $\boldsymbol{\mu} = \mathcal{E}\{\mathbf{x}\}$, $\mathbf{R} = \mathcal{E}\{(\mathbf{x} - \boldsymbol{\mu})(\mathbf{x} - \boldsymbol{\mu})^H\} = \text{diag}\{\sigma_i^2\}$, and where the elements of \mathbf{x} and $\boldsymbol{\mu}$, x_i and $\mu_i = \mathcal{E}\{x_i\}$ are given by (22). Explicit expressions for the derivatives used in (26) are given in the appendix.

Stochastic excitation. The excitation variables $V_m^{(0)}$ and $V_m^{(s)}$ are independent zero mean complex Gaussian random variables with variances σ_0^2 and $\sigma_s^2 = \sigma_0^2 T^2$, respectively. The unknown parameter vector is denoted $\boldsymbol{\theta} = [a \ b \ \Gamma^+]^T$. The Cramér-Rao lower bounds for V_{cc} and V_c are given by (24) and (25), respectively, where $\boldsymbol{\eta}_1^H = [\frac{1}{2a} \ -\frac{1}{2b} \ 0]$, $\boldsymbol{\eta}_2^H = [\frac{1}{2a} \ \frac{1}{2b} \ 0]$ and where $\boldsymbol{\mathcal{I}}(\boldsymbol{\theta})$ is the Fisher information matrix given by

$$\mathcal{I}_{ij}(\boldsymbol{\theta}) = \text{tr} \left\{ \frac{\partial \mathbf{R}}{\partial \theta_i^*} \mathbf{R}^{-1} \frac{\partial \mathbf{R}}{\partial \theta_j} \mathbf{R}^{-1} \right\} \quad (27)$$

where $\text{tr}\{\cdot\}$ denotes the trace operator, $\mathbf{R} = \mathcal{E}\{\mathbf{x}\mathbf{x}^H\}$, and where the elements of \mathbf{x} , x_i are given by (22). Explicit expressions for the derivatives used in (27) are given in the appendix. It can be shown¹ that both statistical models described above yield the same analytical solution when phrased in terms of the signal-to-noise ratios related to the measurement equations in (22). Hence, the CRB for each parameter in $\boldsymbol{\theta}$ is obtained as,

$$\mathcal{E}\left\{|\hat{\theta}_i - \theta_i|^2\right\} \geq [\mathcal{I}^{-1}(\boldsymbol{\theta})]_{ii} \quad (28)$$

and given explicitly, including the CRB for V_{cc} and V_c , as

$$\frac{\mathcal{E}\left\{|\hat{a} - a|^2\right\}}{|a|^2} \geq \frac{1 + |\Gamma^+|^2}{|1 + \Gamma^+|^2 T^2 \text{SNR}} + \frac{1}{\text{SNR}} + \frac{1}{|1 + \Gamma^+|^2 \text{SNR}_a}, \quad (29)$$

$$\frac{\mathcal{E}\left\{|\hat{b} - b|^2\right\}}{|b|^2} \geq \frac{1 + |\Gamma^+|^2}{|1 + \Gamma^+|^2 T^2 \text{SNR}} + \frac{1}{\text{SNR}} + \frac{1}{|1 + \Gamma^+|^2 \text{SNR}_b}, \quad (30)$$

$$\mathcal{E}\left\{|\hat{\Gamma}^+ - \Gamma^+|^2\right\} \geq \frac{1 + |\Gamma^+|^2}{T^2 \text{SNR}}, \quad (31)$$

$$\mathcal{E}\left\{|V_{cc}|^2\right\} \geq \left(\frac{1}{4\text{SNR}_a} + \frac{1}{4\text{SNR}_b}\right) \frac{1}{|1 + \Gamma^+|^2}, \quad (32)$$

$$\mathcal{E}\left\{|V_c - 1|^2\right\} \geq \frac{1 + |\Gamma^+|^2}{|1 + \Gamma^+|^2 T^2 \text{SNR}} + \frac{1}{\text{SNR}} + \left(\frac{1}{4\text{SNR}_a} + \frac{1}{4\text{SNR}_b}\right) \frac{1}{|1 + \Gamma^+|^2}, \quad (33)$$

¹The symbolic functions of Matlab or Mathematica can be used to find the inverse Fisher information matrices.

where

$$\text{SNR} = \frac{|V_m^{(0)}|^2}{\sigma^2} = \frac{\sigma_0^2}{\sigma^2}, \quad (34)$$

$$\text{SNR}_a = \frac{|V_m^{(0)}|^2}{4|a|^2\sigma_4^2} = \frac{\sigma_0^2}{4|a|^2\sigma_4^2}, \quad (35)$$

$$\text{SNR}_b = \frac{|V_m^{(0)}|^2}{4|b|^2\sigma_5^2} = \frac{\sigma_0^2}{4|b|^2\sigma_5^2}, \quad (36)$$

and where the right-hand side applies to the stochastic excitation model described above.

The statistical analysis based on the Cramér-Rao lower bound provides a very useful instrument for sensitivity analysis of the DDC which facilitates physical interpretations. A few examples are given as follows. In Fig. 3 is shown the Cramér-Rao lower bounds for the cross-coupling V_{cc} (32) and the coupling V_c (33) as functions of the signal-to-noise ratio SNR_a with $\text{SNR}_b = \text{SNR}_a$, and for different values of SNR. It is observed that the CRB for the cross-coupling V_{cc} (32) is independent of the estimation of Γ^+ and depends solely on the quality of the measurement channels u and v , *i.e.*, SNR_a and SNR_b . This observation is consistent with the noise-free situation when $\text{SNR}_a = \text{SNR}_b = +\infty$ and $V_{cc} = 0$ regardless of the quality of $\hat{\Gamma}^+$. To see this, note that the calibration equation (12) implies that $\hat{a}A - \hat{b}\frac{B}{Z} = 0$. As should be expected, the CRB for the coupling V_c (33) depends on SNR_a and SNR_b as well as of SNR.

In Fig. 4 is shown the Cramér-Rao lower bounds for the cross-coupling V_{cc} (32) and the coupling V_c (33) as functions of the reflection coefficient Γ^+ . The Cramér-Rao bounds are plotted against the complex domain $|\Gamma^+| \leq 1$ which is shown as a Smith chart at the bottom of the figures. Evidently, the expressions (32) and (33) become singular when $\Gamma^+ = -1$, a situation when there is no energy delivered to the transmission line under test and estimation becomes meaningless.

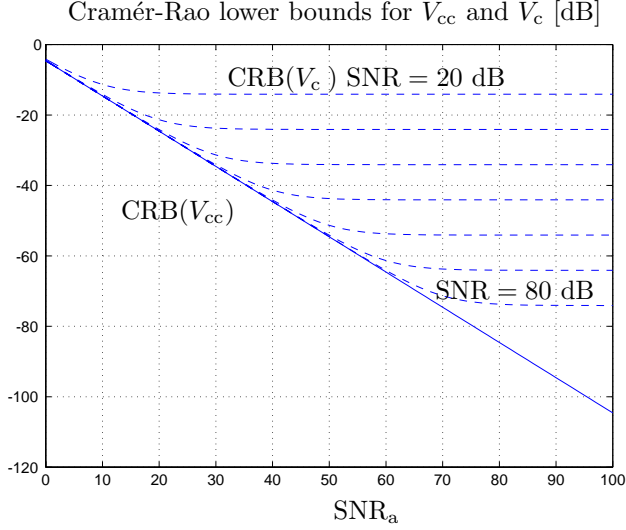


Figure 3: Cramér-Rao lower bounds for the cross-coupling V_{cc} (solid line) and the coupling V_c (dashed lines) as functions of the signal-to-noise ratio SNR_a with $\text{SNR}_b = \text{SNR}_a$. The coupling $\text{CRB}(V_c)$ (dashed lines) is plotted for $\text{SNR} = 20, 30, 40, 50, 60, 70, 80$ dB. Here, $\Gamma^+ = 0.2$ and $T = 0.5$.

4 Experiments

An experiment with coaxial cables was arranged according to the illustration in Fig. 1. The pulses were obtained from a 100 MHz function generator with amplitude $\mathcal{E}_g = 8$ V, and the measurement cables were RG-58 coaxial cables with characteristic impedance $R = 50 \Omega$. The tested transmission line was a 50 m long standard coaxial antenna cable with characteristic impedance $Z = 75 \Omega$. The shield was removed at the pulse insertion point so that the current sensor could be mounted around the inner conductor. The current sensor was designed as a Rogowski coil [ZYJZ05] using a toroidal ferrite core, 4 turns of wire and a measuring resistance of 220Ω . The capacitive voltage sensor was a probe belonging to a 2 GS/s digital oscilloscope. The required frequency functions were obtained using a zero padded 4096 point FFT at a sampling rate of 400 MS/s. The forward and backward traveling waves \hat{V}^+

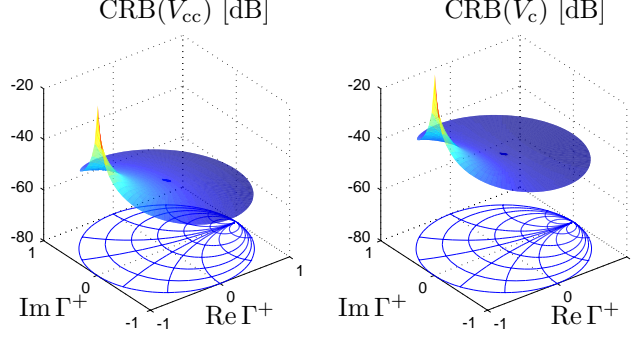


Figure 4: Cramér-Rao lower bounds for the cross-coupling V_{cc} (left figure) and the coupling V_c (right figure) as functions of the reflection coefficient Γ^+ . Here, $\text{SNR} = \text{SNR}_a = \text{SNR}_b = 50$ dB and $T = 0.5$.

and \hat{V}^- were calculated in the frequency domain and then transformed back to the time domain using the IFFT.

In the upper left figure of Fig. 6 is shown the recorded signals that was used in the calibration procedure. Each pulse is labeled according to the corresponding frequency function. In Fig. 5 is shown the estimates \hat{a} and \hat{b} as functions of frequency together with the estimated signal-to-noise ratio $\frac{|V_2^{+(1)}|^2}{\hat{\sigma}^2} = \frac{|V_m^{(0)}|^2 |1 + \hat{\Gamma}^+|^2}{\hat{\sigma}^2}$ related to the propagating pulse $V_2^{+(1)}$. The noise variance $\hat{\sigma}^2$ was estimated from data records with noise only. The bandwidth of the oscilloscope is 500 MHz which is large enough to render \hat{a} relatively stable in the frequency range 0–100 MHz. The current sensor has a ferrite core designed for frequencies higher than 20 MHz and \hat{b} is therefore large for frequencies below this limit. For frequencies above 90 MHz, the signal-to-noise ratio is below 20 dB due to limitations in the pulse generator. The useful frequency band for estimation in this experiment is hence about 10–90 MHz.

The isolation and coupling properties of the calibrated DDC can be conveniently estimated from measured pulses as

$$I = 20 \log \left(\frac{|V_2^{+(1)}|}{|\hat{V}^-|} \right) \approx 20 \log \left(\frac{|V_m^{(0)}| |1 + \hat{\Gamma}^+|}{|\hat{V}^-|} \right) \quad (37)$$

and

$$C = 20 \log \left(\frac{|V_2^{+(1)}|}{|\hat{V}^+|} \right) \approx 20 \log \left(\frac{|V_m^{(0)}| |1 + \hat{\Gamma}^+|}{|\hat{V}^+|} \right) \quad (38)$$

where the transmission line is terminated with a matched load to avoiding reflections. In Fig. 5 is shown the estimated isolation I and coupling C together with the 95% confidence interval $2.45\sqrt{\text{CRB}\{V_{cc}\}}$ where $\text{CRB}\{V_{cc}\}$ (32) has been calculated using the estimated \hat{a} , \hat{b} , $\hat{\Gamma}^+$ and $\hat{\sigma}^2 = \hat{\sigma}_4^2 = \hat{\sigma}_5^2$. Hence, there is a 95% probability that a hypothetical minimum variance unbiased (MVU) estimator should produce better isolation, $\Pr\{|V_{cc}| \leq 2.45\sqrt{\text{CRB}\{V_{cc}\}}\} = 0.95$. It is noted that the isolation of the DDC is almost everywhere confined above this confidence interval except at an interval at low frequencies where the current sensor do not operate properly.

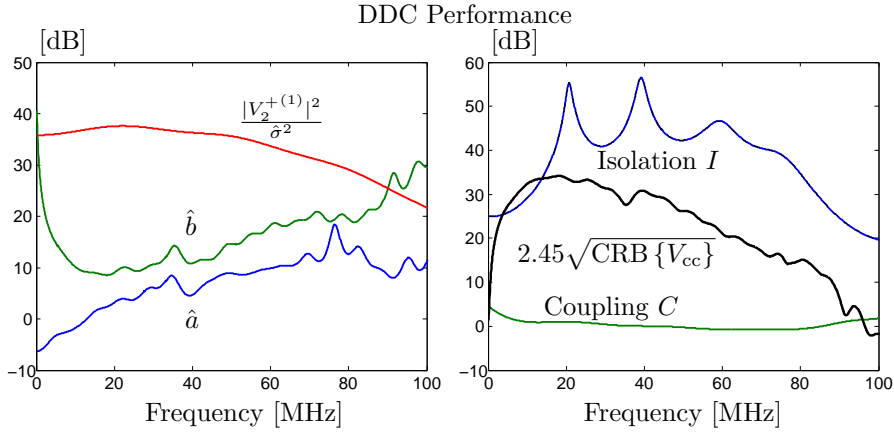


Figure 5: Measurements of the frequency functions \hat{a} , \hat{b} and the signal-to-noise ratio for the propagating pulse $V_2^{+(1)}$ (left figure) and estimated isolation I and coupling C together with the 95% confidence interval $2.45\sqrt{\text{CRB}\{V_{cc}\}}$ for the calibrated DDC (right figure).

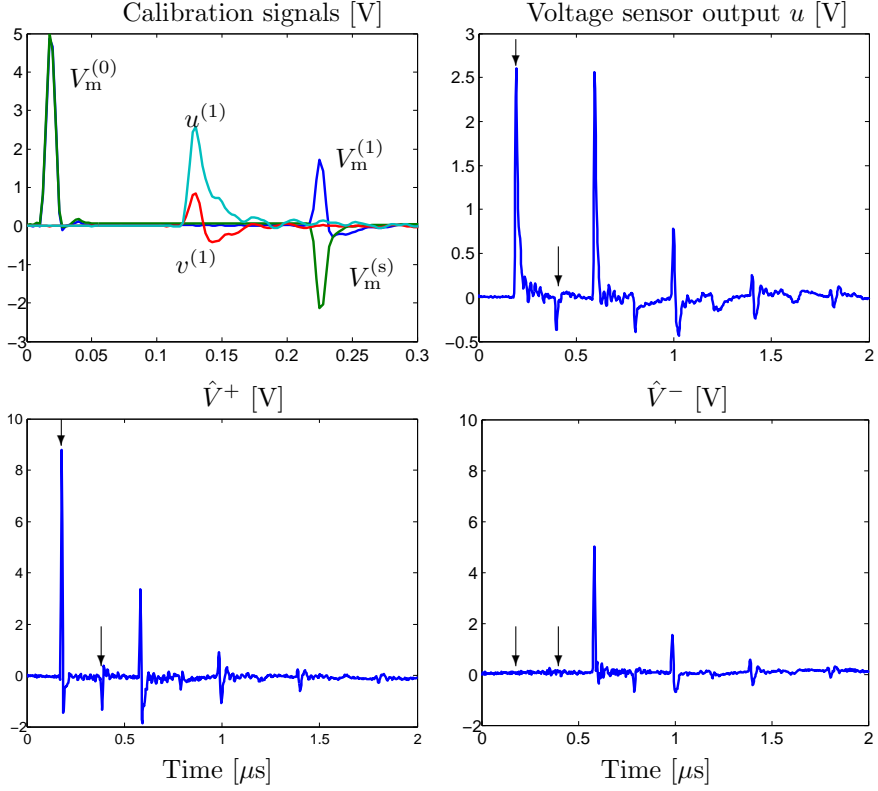


Figure 6: Signals used in the calibration (upper left figure) and time domain output of the DDC when two consecutive pulses are injected at the input of the open ended transmission line. The upper right figure shows the voltage sensor output and two lower figures shows the wave amplitudes of the forward and backward traveling waves, respectively. The timing of the injected pulses are marked by arrows.

In order to illustrate the wave splitting in the time domain, we conclude with an experiment where two consecutive pulses with different amplitudes are injected at the input of the open ended transmission line. In Fig. 6 is shown the voltage sensor output (upper right plot) and the output of the DDC (lower plots) where the timing of the injected pulses are marked by arrows. The first backward propagating pulse \hat{V}^- with significant amplitude corresponds to the first reflection at the open ended transmission line. The isolation property of the DDC is manifested by the apparent absence of the two

injected pulses in the estimated backward propagating waves \hat{V}^- (indicated by arrows). Note that the corresponding isolation in the frequency domain is shown in the right figure of Fig. 5. In conclusion, the resulting directivity $D = I - C$ of the DDC applied to the coaxial cable in this experiment is about 37 dB over a bandwidth of 20–80 MHz.

5 Summary and Conclusions

A Digital Directional Coupler (DDC) that separates forward and backward propagating waves on a transmission line has been presented. The DDC is based on two independent broad band measurements of voltage and current and a frequency domain digital wave splitting using the FFT. A practical procedure is described for calibration of the digital processor with respect to the particular transmission line and the voltage and current sensors that is employed. The Cramér-Rao lower bound is used as a statistical tool to analyze the fundamental performance of the DDC. Important parameters are identified and investigated *e.g.*, the signal-to-noise ratio in the calibration procedure, the characteristic impedance of the transmission line and the frequency transfer functions of the voltage and current sensors. Hence, the Cramér-Rao lower bound provides a very useful instrument for sensitivity analysis of the DDC which facilitates physical interpretations. An experiment has been conducted in order to illustrate the calibration process and to show that a DDC can be designed to operate over an appreciable bandwidth using very simple and low cost sensors. In the experiment, we have used a standard coaxial antenna cable and the resulting directivity (ratio between coupling and cross-coupling) was about 37 dB over a bandwidth of 20–80 MHz.

Acknowledgement

The authors gratefully acknowledge the financial support by the Swedish Knowledge Foundation.

A Explicit Derivatives for the Fisher Information

Explicit expressions for the derivatives associated with the Fisher information matrices employed in section 3 are given below. The differential operator which is used for a complex parameter $z = x + iy$ is defined by $\frac{\partial}{\partial z} = \frac{1}{2} \left(\frac{\partial}{\partial x} - i \frac{\partial}{\partial y} \right)$ and $\frac{\partial}{\partial z^*} = \frac{1}{2} \left(\frac{\partial}{\partial x} + i \frac{\partial}{\partial y} \right)$. For the measurement model in (22) with deterministic excitation, the mean is given by

$$\boldsymbol{\mu} = \begin{pmatrix} -V_m^{(s)} \Gamma^+ \\ V_m^{(s)} \\ V_m^{(0)} \\ \frac{1}{2a} V_m^{(0)} d(1 + \Gamma^+) \\ \frac{1}{2b} V_m^{(0)} d(1 + \Gamma^+) \end{pmatrix}$$

where $d = e^{-\gamma_0(l-l_0)}$. Hence, the Fisher information (26) can be calculated using

$$\frac{\partial \boldsymbol{\mu}}{\partial \boldsymbol{\theta}^T} = \begin{pmatrix} 0 & 0 & -V_m^{(s)} & 0 & -\Gamma^+ \\ 0 & 0 & 0 & 0 & 1 \\ 0 & 0 & 0 & 1 & 0 \\ \frac{-V_m^{(0)} d(1 + \Gamma^+)}{2a^2} & 0 & \frac{V_m^{(0)} d}{2a} & \frac{d(1 + \Gamma^+)}{2a} & 0 \\ 0 & \frac{-V_m^{(0)} d(1 + \Gamma^+)}{2b^2} & \frac{V_m^{(0)} d}{2b} & \frac{d(1 + \Gamma^+)}{2b} & 0 \end{pmatrix}.$$

For the measurement model in (22) with stochastic excitation, the mean is zero and the covariance matrix is given by

$$\mathbf{R} = \begin{pmatrix} \mathbf{R}_1 & \mathbf{0}^T \\ \mathbf{0} & \mathbf{R}_2 \end{pmatrix}$$

where $\mathbf{0}$ is an 3×2 matrix with zeros,

$$\mathbf{R}_1 = \begin{pmatrix} \sigma_s^2 |\Gamma^+|^2 + \sigma^2 & -\sigma_s^2 \Gamma^+ \\ -\sigma_s^2 \Gamma^{+*} & \sigma_s^2 + \sigma^2 \end{pmatrix}$$

and

$$\mathbf{R}_2 =$$

$$\begin{pmatrix} \sigma_0^2 + \sigma^2 & \frac{\sigma_0^2 d^* (1+\Gamma^+)^*}{2a^*} & \frac{\sigma_0^2 d^* (1+\Gamma^+)^*}{2b^*} \\ \frac{\sigma_0^2 d(1+\Gamma^+)}{2a} & \frac{\sigma_0^2 |1+\Gamma^+|^2}{|2a|^2} + \sigma_4^2 & \frac{\sigma_0^2 |1+\Gamma^+|^2}{2a2b^*} \\ \frac{\sigma_0^2 d(1+\Gamma^+)}{2b} & \frac{\sigma_0^2 |1+\Gamma^+|^2}{2a^*2b} & \frac{\sigma_0^2 |1+\Gamma^+|^2}{|2b|^2} + \sigma_5^2 \end{pmatrix}.$$

Hence, the Fisher information (27) can be calculated using

$$\frac{\partial \mathbf{R}}{\partial a} =$$

$$\begin{pmatrix} 0 & 0 & 0 & 0 & 0 \\ 0 & 0 & 0 & 0 & 0 \\ 0 & 0 & 0 & 0 & 0 \\ 0 & 0 & \frac{-\sigma_0^2 d(1+\Gamma^+)}{2a^2} & \frac{-\sigma_0^2 |1+\Gamma^+|^2}{4a|a|^2} & \frac{-\sigma_0^2 |1+\Gamma^+|^2}{2a^2 2b^*} \\ 0 & 0 & 0 & 0 & 0 \end{pmatrix},$$

$$\frac{\partial \mathbf{R}}{\partial a^*} = \begin{pmatrix} 0 & 0 & 0 & 0 & 0 \\ 0 & 0 & 0 & 0 & 0 \\ 0 & 0 & 0 & \frac{-\sigma_0^2 d^* (1+\Gamma^+)^*}{2a^{*2}} & 0 \\ 0 & 0 & 0 & \frac{-\sigma_0^2 |1+\Gamma^+|^2}{4a^*|a|^2} & 0 \\ 0 & 0 & 0 & \frac{-\sigma_0^2 |1+\Gamma^+|^2}{2a^{*2} 2b} & 0 \end{pmatrix},$$

$$\frac{\partial \mathbf{R}}{\partial b} =$$

$$\begin{pmatrix} 0 & 0 & 0 & 0 & 0 \\ 0 & 0 & 0 & 0 & 0 \\ 0 & 0 & 0 & 0 & 0 \\ 0 & 0 & 0 & 0 & 0 \\ 0 & 0 & \frac{-\sigma_0^2 d(1+\Gamma^+)}{2b^2} & \frac{-\sigma_0^2 |1+\Gamma^+|^2}{2a^* 2b^2} & \frac{-\sigma_0^2 |1+\Gamma^+|^2}{4b|b|^2} \end{pmatrix},$$

$$\frac{\partial \mathbf{R}}{\partial b^*} = \begin{pmatrix} 0 & 0 & 0 & 0 & 0 \\ 0 & 0 & 0 & 0 & 0 \\ 0 & 0 & 0 & 0 & \frac{-\sigma_0^2 d^* (1+\Gamma^+)^*}{2b^{*2}} \\ 0 & 0 & 0 & 0 & \frac{-\sigma_0^2 |1+\Gamma^+|^2}{2a 2b^{*2}} \\ 0 & 0 & 0 & 0 & \frac{-\sigma_0^2 |1+\Gamma^+|^2}{4b^*|b|^2} \end{pmatrix},$$

$$\frac{\partial \mathbf{R}}{\partial \Gamma^+} = \begin{pmatrix} \sigma_s^2 \Gamma^{+*} & -\sigma_s^2 & 0 & 0 & 0 \\ 0 & 0 & 0 & 0 & 0 \\ 0 & 0 & 0 & 0 & 0 \\ 0 & 0 & \frac{\sigma_0^2 d}{2a} & \frac{\sigma_0^2 (1+\Gamma^+)^*}{|2a|^2} & \frac{\sigma_0^2 (1+\Gamma^+)^*}{2a2b^*} \\ 0 & 0 & \frac{\sigma_0^2 d}{2b} & \frac{\sigma_0^2 (1+\Gamma^+)^*}{2a^* 2b} & \frac{\sigma_0^2 (1+\Gamma^+)^*}{|2b|^2} \end{pmatrix},$$

and

$$\frac{\partial \mathbf{R}}{\partial \Gamma^{+*}} = \begin{pmatrix} \sigma_s^2 \Gamma^+ & 0 & 0 & 0 & 0 \\ -\sigma_s^2 & 0 & 0 & 0 & 0 \\ 0 & 0 & 0 & \frac{\sigma_0^2 d^*}{2a^*} & \frac{\sigma_0^2 d^*}{2b^*} \\ 0 & 0 & 0 & \frac{\sigma_0^2 (1+\Gamma^+)}{|2a|^2} & \frac{\sigma_0^2 (1+\Gamma^+)}{2a2b^*} \\ 0 & 0 & 0 & \frac{\sigma_0^2 (1+\Gamma^+)}{2a^* 2b} & \frac{\sigma_0^2 (1+\Gamma^+)}{|2b|^2} \end{pmatrix}.$$

References

- [And98] P. M. Anderson. *Power System Protection*. Wiley-IEEE Press, 1998.
- [AS98] N. H. Ahmed and N. N. Srinivas. On-line partial discharge detection in cables. *IEEE Transactions on Dielectrics and Electrical Insulation*, 5(2):181–188, April 1998.
- [BD00] S. Boggs and J. Densley. Fundamentals of partial discharge in the context of field cable testing. *IEEE Electrical Insulation Magazine*, 16(5):13–18, Sep./Okt. 2000.
- [Bo00] Z. Q. Bo. Transient based protection for power transmission system. In *IEEE Power Engineering Society Winter Meeting*, volume 3, pages 1832–1837, 2000.
- [Col05] S. L. Collier. Fisher information for a complex gaussian random variable: beamforming applications for wave propagation in a random medium. *IEEE Transactions on Signal Processing*, 53(11):4236–4248, 2005.

-
- [DN01] A. Dogandzic and A. Nehorai. Cramér–Rao bounds for estimating range, velocity, and direction with an active array. *IEEE Transactions on Signal Processing*, 49(6):1122–1137, June 2001.
- [DT91] A. J. Devaney and G. A. Tsihirintzis. Maximum likelihood estimation of object location in diffraction tomography. *IEEE Transactions on Signal Processing*, 39(3):672–682, March 1991.
- [GN06] M. Gustafsson and S. Nordebo. Characterization of MIMO antennas using spherical vector waves. *IEEE Transactions on Antennas and Propagation*, 54(9):2679–2682, 2006.
- [Kay93] S. M. Kay. *Fundamentals of Statistical Signal Processing, Estimation Theory*. Prentice-Hall, Inc., NJ, 1993.
- [KG05] A. Kyprianou and G. E. Georghiou. Wavelet packet denoising for on-line partial discharge detection in high voltage systems. In *Mediterranean Conference on Control and Automation*, pages 1184–1189, 2005.
- [LPP03] V. Latva-Pukkila and P. Pakonen. Disturbances occurring in on-site partial discharge measurements. In *Conference record of Nordic Insulation Symposium (NORDIS)*, pages 11–19, 2003.
- [Mas00] M. Mashikian. Partial discharge location as a diagnostics tool for power cables. In *Proceedings of the IEEE Power Engineering Society Winter Meeting*, volume 3, pages 1604–1608, 2000.
- [MYJ80] G. Matthaei, L. Young, and E. M. T. Jones. *Microwave filters, impedance matching networks, and coupling structures*. Artech House, Inc., 1980.
- [NB99] P. S. Naidu and A. Buvaneswari. A study of Cramér–Rao bounds on object shape parameters from scattered field. *IEEE Transactions on Signal Processing*, 47(5):1478–1481, May 1999.
- [NG06] S. Nordebo and M. Gustafsson. Statistical signal analysis for the inverse source problem of electromagnetics. *IEEE Transactions on Signal Processing*, 54(6):2357–2362, 2006.
- [PE03] R. Papazyan and R. Eriksson. Calibration for time domain propagation constant measurements on power cables. *IEEE Transactions on Instrumentation and Measurement*, 52(2):415–418, April 2003.

- [Poz98] David M. Pozar. *Microwave Engineering*. John Wiley & Sons, New York, 1998.
- [PSH⁺99] D. Pommerenke, T. Strehl, R. Heinrich, W. Kalkner, F. Schmidt, and W. Weissenberg. Discrimination between internal PD and other pulses using directional coupling sensors on HV cable systems. *IEEE Transactions on Dielectrics and Electrical Insulation*, 6(6):814–824, Dec. 1999.
- [SHV91] E. F. Steennis, E. Hetzel, and C. W. J. Verhoeven. Diagnostic medium voltage cable test at 0.1 Hz. In *Proceedings of the 3rd IEEE International Conference on Insulated Power Cables*, pages 408–414, 1991.
- [Smi05] S. T. Smith. Statistical resolution limits and the complexified Cramér-Rao bound. *IEEE Transactions on Signal Processing*, 53(5):1597–1609, 2005.
- [SSS00] I. Shim, J. J. Soraghan, and W. H. Siew. Digital signal processing applied to the detection of partial discharge: an overview. *IEEE Electrical Insulation Magazine*, 16(3):6–12, May/June 2000.
- [Sym92] R. R. A. Syms. The digital directional coupler: improved design. *IEEE Photonics Technology Letters*, 4(10):1135–1138, Oct. 1992.
- [TD91] G. A. Tsihirintzis and A. J. Devaney. Maximum likelihood estimation of object location in diffraction tomography, Part ii; strongly scattering objects. *IEEE Transactions on Signal Processing*, 39(6):1466–1470, June 1991.
- [Vee05] J. Veen. *On-line signal analysis of partial discharges in medium-voltage power cables*. Ph.d. thesis, Eindhoven University of Technology, the Netherlands, 2005.
- [VW03] J. Veen and P. C. J. M. van der Wielen. The application of matched filter to PD detection and localization. *IEEE Electrical Insulation Magazine*, 19(5):20–26, Sep./Okt. 2003.
- [ZYJZ05] J. Zhu, L. Yang, J. Jia, and Q. Zhang. The design of rogowski coil with wide band using for partial discharge measurements. In *Proceedings of 2005 International Symposium on Electrical Insulation*, pages 518–521, 2005.

PART V

**Partial Discharge
Measurement Using a
Digital Directional Coupler**

Part V is submitted as:

J. Lundbäck, S. Nordebo and T. Biro, "Partial Discharge Measurement Using a Digital Directional Coupler", submitted to *IEEE Transactions on Instrumentation and Measurements*.

Partial Discharge Measurements Using a Digital Directional Coupler

J. Lundbäck, S. Nordebo and T. Biro

Abstract

In this paper, we describe a Digital Directional Coupler (DDC) that separates forward and backward traveling waves on transmission lines. Based on two independent wide-band measurements of voltage and current and a frequency domain digital wave splitting using the FFT, the DDC is a versatile device for direction separation. A practical procedure is described for calibration of the digital processor with respect to the particular transmission line and the voltage and current sensors that are employed. A DDC has been designed and implemented on medium voltage equipment at a power distribution station using low cost wide-band sensors. The directional separation capabilities of the DDC are visualized by partial discharge measurements conducted on XLPE insulated power cables.

1 Introduction

There are several applications where wave splitting or separation of forward and backward propagating waves is incorporated *e.g.*, as a part of a vector network analyzer. Standard directional couplers are often designed as a hardware module whose properties are directly linked to the electromagnetic coupling effects within the module. However, these coupling effects are usually very difficult to control and it is a non-trivial task to design a directional coupler that maintains high performance (isolation and directivity) over an appreciable bandwidth, see *e.g.*, [Poz98, MYJ80].

Considering a directional coupler for transmission lines, several applications could benefit from its functionality *e.g.*, fault localization and partial discharge (PD) monitoring on power lines or transient based protection techniques for power transmission systems, see *e.g.*, [PSH⁺99, Vee05, Bo00, Sto05].

The ongoing research on on-line PD diagnostics has produced several apparatus that have been commercially available, see *e.g.*, [SHV91, Mas00, FS06]. Methods for PD diagnostics must include separation of individual PD signals and their direction. Clearly, a directional coupler for power lines with good isolation properties can be very useful for discriminating between transients, pulses, PD phenomena etc., which are emanating from different locations in the power cable network [PSH⁺99].

Noise and interference mitigation is another fundamental problem in any PD monitoring or transient based protection system, see *e.g.*, [SSS00, LPP03]. Based on advanced signal processing, many noise and interference reduction techniques have been reported, [Vee05, ZZK05]. As the interference includes many components of different nature *e.g.*, wide-band background noise, narrowband interference and pulse-shaped disturbances, see *e.g.*, [BD00, And98], a directional coupler for power lines with good isolation properties can be very useful for efficient reduction of any exterior noise emanating from locations other than that under investigation.

The Digital Directional Coupler (DDC) described here is based on two independent wide-band measurements of voltage and current on a transmission line, and a frequency domain digital wave splitting using the FFT. Both sensors are designed for wide-band measurements and built according to standard techniques to maintain a high degree of simplicity. Hence, the DDC can be designed to operate over an appreciable bandwidth by using conventional voltage and current sensors in connection with the digital wave splitting. Based on modern signal processing techniques and devices, the directional coupler is versatile and is easily incorporated into the existing power system.

A practical procedure is described that calibrates the DDC for the transmission line under test and the sensors that are employed. In essence, this is a calibration for identification of the linear mapping that exist between the measured voltage and current on the transmission line and the amplitudes of the propagating waves. A similar technique is given in [PE03] for measurement of the propagation constant of a power cable.

An experiment has been arranged at a power distribution station using high-voltage equipment where PD signals are created in cross-linked polyethylene (XLPE) insulated power cables. The configuration allowed multiple reflections to occur that were resolved by the DDC. The rest of the paper is outlined as follows. In section 2, the digital directional coupler is introduced and the calibration procedure is described. In section 3, an experiment is described where a DDC has been designed and implemented for measurements on a power cable in a power distribution station.

2 The Digital Directional Coupler

2.1 Wave propagation model

Consider the frequency domain representation of a single-mode transmission line, where the one-dimensional electric voltage $V(x)$ and current $I(x)$ are given as

$$\begin{cases} V(x) = V^+ e^{-\gamma x} + V^- e^{\gamma x} \\ I(x) = \frac{V^+}{Z} e^{-\gamma x} - \frac{V^-}{Z} e^{\gamma x} \end{cases} \quad (1)$$

where V^+ and V^- are the complex amplitudes associated with forward and backward propagating waves, γ the complex propagation constant, x the length dimension and Z the characteristic impedance of the transmission line, see *e.g.*, [Poz98]. The mapping between the total voltage $V = V(0)$ and current $I = I(0)$ and the wave amplitudes V^+ and V^- at the transmission line input is given by

$$\begin{pmatrix} V^+ \\ V^- \end{pmatrix} = \begin{pmatrix} \frac{1}{2} & \frac{1}{2}Z \\ \frac{1}{2} & -\frac{1}{2}Z \end{pmatrix} \begin{pmatrix} V \\ I \end{pmatrix}. \quad (2)$$

Assume now that two decoupled sensors are available measuring the voltage V and current I as

$$\begin{cases} u = AV \\ v = BI \end{cases} \quad (3)$$

where A and B are the corresponding sensor frequency functions, *cf.*, also Fig. 1. Then there is a linear, one-to-one relationship between the measured signals u and v and the wave amplitudes V^+ and V^- given by

$$\begin{pmatrix} V^+ \\ V^- \end{pmatrix} = \begin{pmatrix} a & b \\ a & -b \end{pmatrix} \begin{pmatrix} u \\ v \end{pmatrix} \quad (4)$$

where $a = \frac{1}{2A}$ and $b = \frac{Z}{2B}$.

2.2 Calibration procedure

Consider the calibration set-up in Fig. 1. The device under test (DUT) is an open ended transmission line of length l_1 , characteristic impedance Z and complex propagation constant γ . Two sensors are applied to the left side of the DUT measuring the voltage $u = AV$ and current $v = BI$ on the cable

input. The calibration set-up consists further of a pulse generator with voltage \mathcal{E}_g and generator resistance R , a matched power splitter with transmission coefficient T and auxiliary coaxial cables of length l_0 and l with characteristic impedance R and propagation constant $\gamma_0 = i\omega/c_0$ where c_0 is the speed of wave propagation. A measurement voltage V_m is obtained over the load resistance R via the power splitter as depicted in Fig. 1.

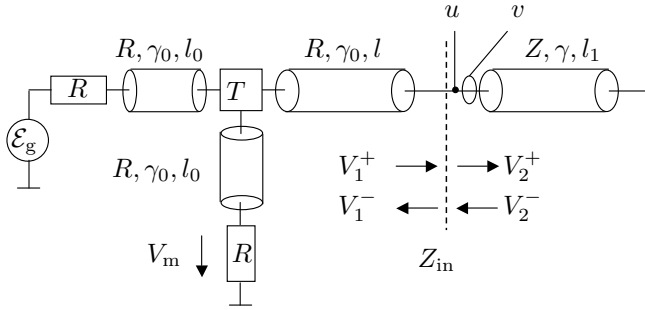


Figure 1: Calibration set-up with open ended transmission line.

The voltage reflections and transmissions at the indicated reference plane in Fig. 1 is given by the scattering formulation

$$\begin{pmatrix} V_1^- \\ V_2^+ \end{pmatrix} = \begin{pmatrix} \Gamma^+ & 1 - \Gamma^+ \\ 1 + \Gamma^+ & -\Gamma^+ \end{pmatrix} \begin{pmatrix} V_1^+ \\ V_2^- \end{pmatrix} \quad (5)$$

where

$$\Gamma^+ = \frac{Z - R}{Z + R}. \quad (6)$$

The total input impedance of the open ended transmission line as seen from the left at the reference plane is $Z_{in} = Z \coth \gamma l$ and the corresponding reflection coefficient is hence given by

$$\Gamma = \frac{Z_{in} - R}{Z_{in} + R} = \frac{\Gamma^+ + e^{-\gamma 2l}}{1 + e^{-\gamma 2l} \Gamma^+} = \Gamma^+ + e^{-\gamma 2l} (1 - \Gamma^{+2}) + \dots \quad (7)$$

yielding the reflected voltage $V_1^- = V_1^+ \Gamma$. The incident wave at the reference plane is given by

$$V_1^+ = \frac{\mathcal{E}_g}{2} e^{-\gamma_0(l+l_0)} T \quad (8)$$

and the corresponding first order pulses are hence given by

$$\begin{cases} V_1^{-(1)} = V_1^+ \Gamma^+ \\ V_2^{+(1)} = V_1^+ (1 + \Gamma^+). \end{cases} \quad (9)$$

The observed pulses at the measurement resistor are given by

$$\begin{cases} V_m^{(0)} = \frac{\mathcal{E}_g}{2} e^{-\gamma_0 2l_0} T \\ V_m^{(1)} = V_1^{-(1)} e^{-\gamma_0 (l+l_0)} T \end{cases} \quad (10)$$

and it is found that $V_1^+ = V_m^{(0)} e^{-\gamma_0 (l-l_0)}$. The reflection coefficient Γ^+ can be obtained from a short circuit measurement where $V_1^{-(s)} = -V_1^+$ and $V_m^{(s)} = V_1^{-(s)} e^{-\gamma_0 (l+l_0)} T$, and hence

$$\Gamma^+ = \frac{V_1^{-(1)}}{V_1^+} = -\frac{V_1^{-(1)}}{V_1^{-(s)}} = -\frac{V_m^{(1)}}{V_m^{(s)}}. \quad (11)$$

The parameters a and b are obtained from the calibration equations

$$\begin{cases} V_2^{+(1)} &= au^{(1)} + bv^{(1)} \\ 0 &= au^{(1)} - bv^{(1)} \end{cases} \quad (12)$$

with the straightforward solution

$$\begin{cases} a = \frac{V_2^{+(1)}}{2u^{(1)}} \\ b = \frac{V_2^{+(1)}}{2v^{(1)}} \end{cases} \quad (13)$$

where $u^{(1)}$ and $v^{(1)}$ correspond to the first order pulses of u and v , respectively. Fig. 2 illustrate the calibration signals in an experiment using an XLPE insulated power cable. Note that the assumption $u^{(1)} = AV = AV_2^{+(1)}$ and $v^{(1)} = BI = BI_2^{+(1)} = BV_2^{+(1)}/Z$ yields the correct answer $a = \frac{1}{2A}$ and $b = \frac{Z}{2B}$. The calibration procedure can now be summarized by the following operations

$$\begin{cases} \Gamma^+ &= -\frac{V_m^{(1)}}{V_m^{(s)}} \\ V_2^{+(1)} &= V_m^{(0)} e^{-\gamma_0 (l-l_0)} (1 + \Gamma^+) \\ a &= \frac{V_2^{+(1)}}{2u^{(1)}} \\ b &= \frac{V_2^{+(1)}}{2v^{(1)}}. \end{cases} \quad (14)$$

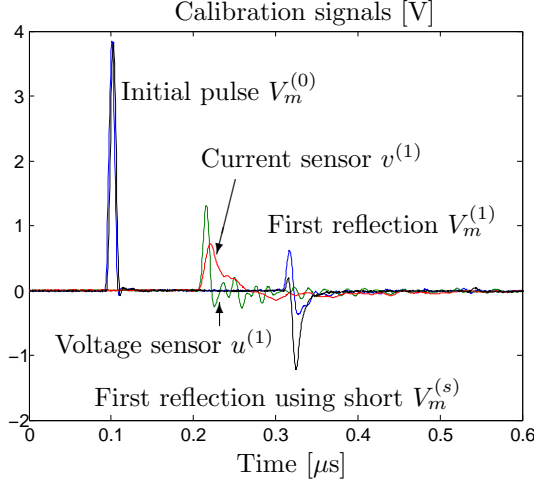


Figure 2: The calibration signals recorded for calibration of a DDC implemented on an XLPE insulated power cable. The bandwidth is approximately 50 MHz. Each pulse is marked by the corresponding frequency domain representation.

Let \hat{a} and \hat{b} denote estimates of the parameters a and b according to the measurement model given in (4). The estimated wave amplitudes are thus given by

$$\begin{pmatrix} \hat{V}^+ \\ \hat{V}^- \end{pmatrix} = \begin{pmatrix} \hat{a} & \hat{b} \\ \hat{a} & -\hat{b} \end{pmatrix} \begin{pmatrix} u \\ v \end{pmatrix}. \quad (15)$$

Using (2) and (3) with $A = \frac{1}{2a}$ and $B = \frac{Z}{2b}$, the estimation (15) is given by

$$\begin{cases} \hat{V}^+ = \left(\hat{a} \frac{1}{2a} + \hat{b} \frac{1}{2b} \right) V^+ + \left(\hat{a} \frac{1}{2a} - \hat{b} \frac{1}{2b} \right) V^- \\ \hat{V}^- = \left(\hat{a} \frac{1}{2a} - \hat{b} \frac{1}{2b} \right) V^+ + \left(\hat{a} \frac{1}{2a} + \hat{b} \frac{1}{2b} \right) V^- \end{cases} \quad (16)$$

The cross-coupling V_{cc} is given by

$$V_{cc} = \hat{a} \frac{1}{2a} - \hat{b} \frac{1}{2b} = \Delta a \frac{1}{2a} - \Delta b \frac{1}{2b} \quad (17)$$

and the coupling V_c

$$V_c = \hat{a} \frac{1}{2a} + \hat{b} \frac{1}{2b} = \Delta a \frac{1}{2a} + \Delta b \frac{1}{2b} + 1 \quad (18)$$

where $\Delta a = \hat{a} - a$ and $\Delta b = \hat{b} - b$.

Using standard definitions from microwave technology [Poz98], the *coupling*, *directivity* and *isolation* (in dB) can be obtained for the DDC,

$$C = -20 \log(|V_c|), \quad (19)$$

$$D = 20 \log \left(\left| \frac{V_c}{V_{cc}} \right| \right), \quad (20)$$

$$I = -20 \log(|V_{cc}|), \quad (21)$$

respectively, where $I = D + C$. An ideal directional coupler has infinite isolation and directivity corresponding to $V_{cc} = 0$ and perfect coupling, *i.e.*, $V_c = 1$.

The isolation and coupling properties of the calibrated DDC can be conveniently estimated from measured pulses as

$$I = 20 \log \left(\frac{|V_2^{+(1)}|}{|\hat{V}^-|} \right) \approx 20 \log \left(\frac{|V_m^{(0)}| |1 + \hat{\Gamma}^+|}{|\hat{V}^-|} \right) \quad (22)$$

and

$$C = 20 \log \left(\frac{|V_2^{+(1)}|}{|\hat{V}^+|} \right) \approx 20 \log \left(\frac{|V_m^{(0)}| |1 + \hat{\Gamma}^+|}{|\hat{V}^+|} \right). \quad (23)$$

3 Experiments

In an experiment at a power distribution station, the DDC was used to measure and separate PD signals based on the direction of travel. A schematic diagram of the experiment is depicted in Fig. 3. The equipment consists of a 0 – 230 V variac, one low to medium voltage transformer with a ratio of 1 : 90.7, and one 140.6 m long 22 kV XLPE insulated single-phase power cable. The variac is supplied via the service-net 230 V, 50 Hz using low-pass filters to mitigate disturbances and interference. Using an Ultrasonic receiver, the equipment was verified to be free of partial discharges when the applied voltage was less than 13 kV. The phase velocity on the 22 kV power cable was estimated to 0.5 – 0.55 times the speed of light. At the points marked

by 1 or 2 in Fig. 3, we connect a 10 kV power cable of 1 m that has been prepared to create partial discharges at an applied voltage of approximately 5 kV. To obtain partial discharges from the 10 kV cable, either one end of the cable is left un-terminated or a needle is used to penetrate the insulation. By changing *e.g.*, the thickness of the needle, the penetration depth and the applied voltage, we can vary the properties of the partial discharges.

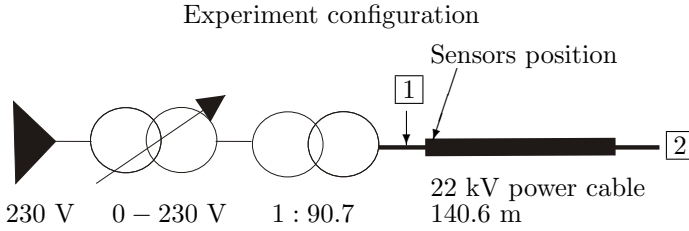


Figure 3: Schematic picture of the experiment. At points marked by 1 and 2 additional power cables are connected as described in the experiments. The sensors are mounted on the 22 kV power cable. Starting from the left is the service-net, the variac, the low to medium voltage transformer and the power cable.

The inductive current sensor was designed as a Rogowski coil, see *e.g.*, [ZYJZ05], using a toroidal ferrite core and mounted around the center conductor of the 22 kV power cable. The capacitive voltage sensor is connected to the center conductor via a coupling capacitor. Both sensors were designed to operate in the frequency range of 2 – 50 MHz. In the calibration of the DDC, a function generator capable of supplying pulses with amplitude $\mathcal{E}_g = 8$ V and 100 MHz bandwidth was used. The required frequency domain representation of the sensor signals were obtained using a zero-padded 4096-point FFT at a sampling rate of 400 MS/s. The forward and backward traveling waves \hat{V}^+ and \hat{V}^- were calculated in the frequency domain and then transformed back to the time domain using the IFFT.

In Fig. 4 is shown the estimates of a and b as functions of frequency (left figure) and the estimated isolation I and coupling C (right figure).

The calibration of the DDC results in the estimates of a and b , which we utilize in (15). To obtain the estimates of I and D depicted in Fig. 4, a second measurement was made, where \hat{V}^+ and \hat{V}^- were calculated. In the time domain we then extract the initial pulse from both \hat{V}^+ and \hat{V}^- , which corresponds solely to a forward traveling wave (no backward traveling wave

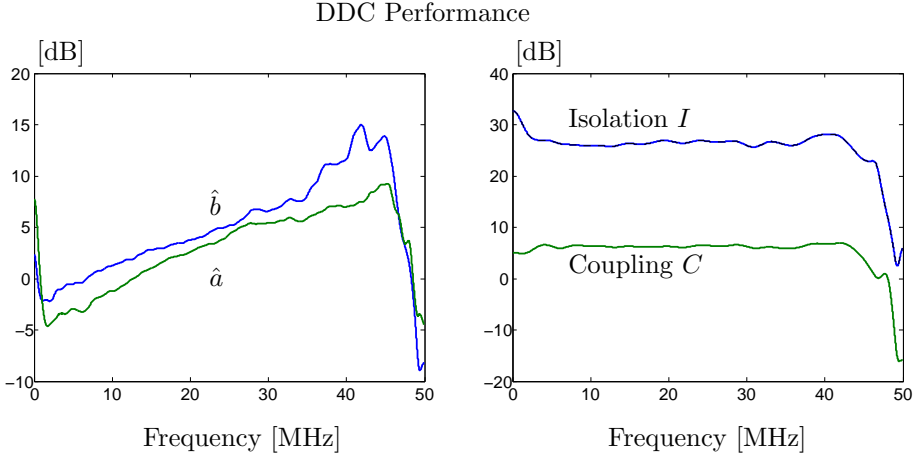


Figure 4: The left figure depicts the estimates of a and b . Observe that the sharp edge at 50 MHz is due to the noise reduction processing. The right figure depicts the isolation and coupling of the DDC as functions of frequency. Note the flat characteristics of the isolation and coupling.

present). Finally, we obtain $V_m^{(0)}$ and from the calibration measurement we have $\hat{\Gamma}^+$ and we calculate I and C using (22) and (23), respectively.

Before the wave splitting operation is applied to measurements of partial discharge signals, each measurement series is filtered using a digital filter bank to attenuate strong interferers *e.g.*, narrow band radio transmissions. The filters are notch type and the total number of filters are dependent on the number and power of the interferers. Investigation of the noise characteristics confirmed that during short time periods the noise could be described as a sum of additive white Gaussian noise and narrow-band interferers, similar to the model in [SNPB05].

In [BPW96] a Gaussian pulse function was employed to model a partial discharge pulse,

$$s(t) = \frac{V_0}{\sqrt{2\pi\beta^2}} e^{-t^2/2\beta^2}, \quad (24)$$

where β is the half pulse width at 60 % amplitude measured in seconds. Let $f_\beta = \sqrt{2}/(2\pi\beta)$ be a measure of the bandwidth of the pulse. The amplitude V_0 can be related to the charge Q of the PD, using $QZ = \int s(t)dt$, as

$$V_0 = QZ. \quad (25)$$

To provide some insight into the sensitivity of the DDC and the properties of the experiment, we provide numerical values of measured quantities related to (24) *e.g.*, V_0 . These are often termed *effective* values since the calculations are based on measurements using the sensors located at a position (often at the end of a power cable) not equal to the position of the partial discharge location [Bog90]. The PD signals are distorted by the power cable that is acting as a low-pass filter.

3.1 Experiment I

In the first experiment we connect the 10 kV power cable at point 1 and leave point 2 unconnected, *i.e.*, the 22 kV power cable is open at the far end from the sensors position. In Fig. 5, a short period of the recorded sensor signals are depicted in the left figure and the corresponding forward traveling wave amplitude (FTWA) and backward traveling wave amplitude (BTWA) obtained from the DDC are depicted in the right figure.

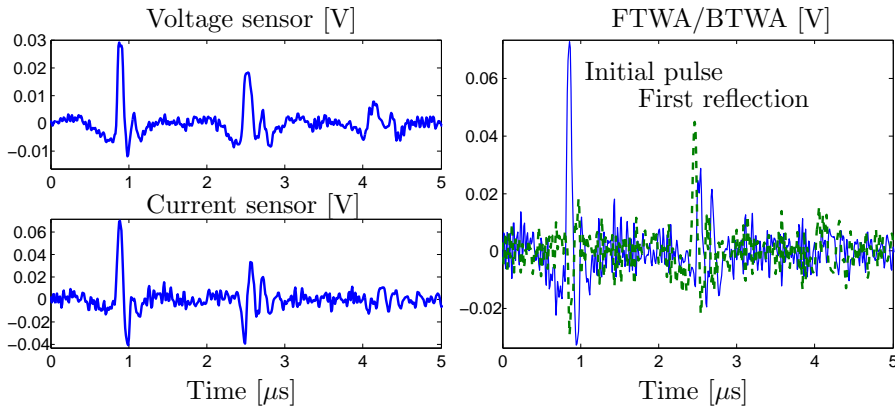


Figure 5: In the left figure is shown the signals recorded from the sensors and in the right figure the corresponding output signals of the DDC where the solid and dashed curves corresponds to FTWA and BTWA, respectively. The initial pulse corresponds to a PD pulse while the first reflection corresponds to the PD pulse reflected at the open end of the 22 kV power cable.

The first pulse in the right figure is a forward traveling wave, marked as the initial pulse and coming from the PD site on the 10 kV power cable. The

second pulse, marked as the first reflection, is a combination of a forward and a backward traveling wave *i.e.*, a reflection of the initial pulse at the open end of the 22 kV power cable. The initial pulse has a pulse width of approximately $0.1 \mu\text{s}$, corresponding to $\beta = 15 \text{ ns}$ and $V_0 = 13 \cdot 10^{-10} \text{ V}$ in (24). The corresponding bandwidth of the pulse is $f_b = 15 \text{ MHz}$. Typically, the pulse width is $1 - 10 \text{ ns}$ at the source, [SSS00, BD00], corresponding to β less than 5 ns . Investigations where β equals $5 - 80 \text{ ns}$ have also been conducted [BPW96].

The time difference between the two pulses corresponds to the time needed to travel back and forth on the 22 kV power cable. The initial pulse is barely visible in the BTWA. For the first reflection, both outputs of the DDC display a pulse where the BTWA is greater than the FTWA. Taking both FTWA and BTWA into account it is easy to verify from which direction a pulse arrive. However, this is not necessary if the isolation and directivity of the DDC can be further enhanced. Also, the time delay between two consecutive pulses can serve as a simple but crude tool to exclude multiple reflections. Due to the length of the 22 kV power cable (the power cable has a large attenuation per meter for higher frequencies [OBP⁺05]) and the sensitivity of the sensors, only one reflection is clearly visible and also resolved by the DDC.

3.2 Experiment II

In the second experiment, the 10 kV power cable is connected at point 2 in Fig. 3 so that PD pulses travels the 22 kV power cable before recorded at the sensors. A 22 m long 12 kV XLPE insulated power cable is connected at point 1 and left open-ended to create multiple reflections for the DDC to resolve. Also, based on the previous experiment we decrease the bandwidth of the DDC to $2 - 10 \text{ MHz}$ to further mitigate interference. This flexibility is one advantage of the versatile DDC. The result is depicted in Fig. 6.

A PD pulse created on the 10 kV power cable will travel the 22 kV power cable and when reflected at the position of the sensors, some energy will be transmitted to the 12 kV power cable. The DDC will classify this pulse as a combination of a forward and a backward traveling wave. After reflection at the open-end of the 12 kV power cable the pulse will return to the 22 kV and be classified by the DDC as a forward traveling wave.

The initial pulse in the right figure of Fig. 6 clearly corresponds to a backward traveling wave and a much weaker forward traveling wave. The pulse width is approximately $0.2 \mu\text{s}$, $\beta = 30 \text{ ns}$ and $V_0 = 15 \cdot 10^{-10} \text{ V}$. This corresponds to an approximative bandwidth $f_b \approx 7.5 \text{ MHz}$ and a charge of 60 pC .

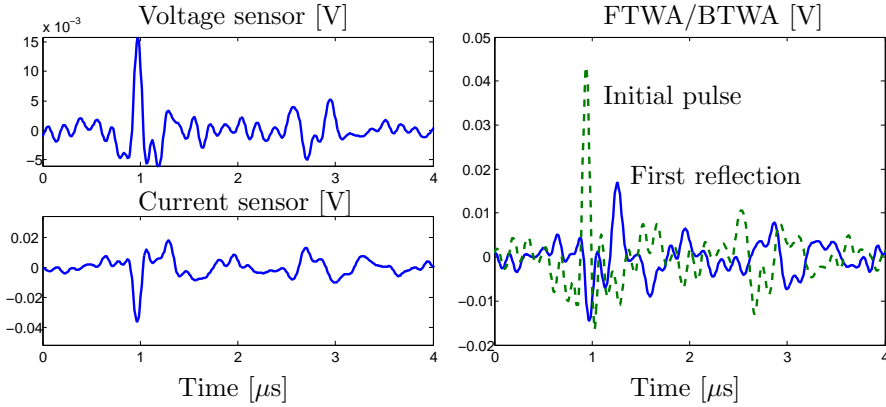


Figure 6: In the left figure is shown the signals recorded from the sensors and in the right figure the corresponding output signals of the DDC where the solid and dashed curves corresponds to FTWA and BTWA, respectively.

The time difference between the initial pulse and the first reflection is approximately $0.3 \mu\text{s}$, corresponding to the measured phase velocity of 0.5 times the speed of light and twice the length of the 12 kV power cable. Observe that the first reflection is hard to see in the sensor signals but readily seen in the FTWA.

Also, in the experiment we verified that the DDC was able to resolve an initial PD pulse with $\beta = 30 \text{ ns}$ and $V_0 = 4 \cdot 10^{-10} \text{ V}$, corresponding to a charge of 16 pC.

4 Summary and Conclusions

We have presented partial discharge measurements using a Digital Directional Coupler (DDC) that separates forward and backward propagating waves on a transmission line. The DDC is based on two independent wide-band measurements of voltage and current and a frequency domain digital wave splitting using the FFT. A practical procedure is described for calibration of the digital processor with respect to the particular transmission line and the sensors that is employed. Experiments using medium voltage equipment in a power distribution station and a DDC implemented on an XLPE insulated power cable are described. The isolation and coupling of the DDC were determined

to 27 dB and 5 dB, respectively; over a bandwidth of approximately 50 MHz. Measurements displays the ability of DDC to separate partial discharge pulses based on the direction of travel even for pulses hardly visible in the sensor signals.

Acknowledgement

The authors gratefully acknowledge the financial support by the Swedish Knowledge Foundation. The authors also express their gratitude to Öresundskraft AB, Sweden, and especially to Olle Corfitsson for access to high voltage cables and systems.

References

- [And98] P. M. Anderson. *Power System Protection*. Wiley-IEEE Press, 1998.
- [BD00] S. Boggs and J. Densley. Fundamentals of partial discharge in the context of field cable testing. *IEEE Electrical Insulation Magazine*, 16(5):13–18, Sep./Okt. 2000.
- [Bo00] Z. Q. Bo. Transient based protection for power transmission system. In *IEEE Power Engineering Society Winter Meeting*, volume 3, pages 1832–1837, 2000.
- [Bog90] S. A. Boggs. Partial discharge III. Cavity-induced PD in solid dielectrics. *IEEE Electrical Insulation Magazine*, 6(6):11–16, 19–20, 1990.
- [BPW96] S. A. Boggs, A. Pathak, and P. Walker. Partial discharge XXII: high frequency attenuation in shielded solid dielectric power cable and implications thereof for PD location. *IEEE Electrical Insulation Magazine*, 12(1):9–16, Jan./Feb. 1996.
- [FS06] M. Fenger and H. Sedding. Recent experiences with on-line PD testing of MV XLPE and EPR cable. In *Conference Record of the 2006 IEEE International Symposium on Electrical Insulation, 2006*, pages 42–45, 2006.

-
- [LPP03] V. Latva-Pukkila and P. Pakonen. Disturbances occurring in on-site partial discharge measurements. In *Conference record of Nordic Insulation Symposium (NORDIS)*, pages 11–19, 2003.
- [Mas00] M. Mashikian. Partial discharge location as a diagnostics tool for power cables. In *Proceedings of the IEEE Power Engineering Society Winter Meeting*, volume 3, pages 1604–1608, 2000.
- [MYJ80] G. Matthaei, L. Young, and E. M. T. Jones. *Microwave filters, impedance matching networks, and coupling structures*. Artech House, Inc., 1980.
- [OBP⁺05] H. N. O, T.R. Blackburn, B.T. Phung, M. Vakilian, M.S. Naderi, and H. Zhang. Investigation of high frequency signal propagation characteristics on HV XLPE cables. *The 7th IEEE International Power Engineering Conference*, pages 1–6, 2005.
- [PE03] R. Papazyan and R. Eriksson. Calibration for time domain propagation constant measurements on power cables. *IEEE Transactions on Instrumentation and Measurement*, 52(2):415–418, April 2003.
- [Poz98] David M. Pozar. *Microwave Engineering*. John Wiley & Sons, New York, 1998.
- [PSH⁺99] D. Pommerenke, T. Strehl, R. Heinrich, W. Kalkner, F. Schmidt, and W. Weissenberg. Discrimination between internal PD and other pulses using directional coupling sensors on HV cable systems. *IEEE Transactions on Dielectrics and Electrical Insulation*, 6(6):814–824, Dec. 1999.
- [SHV91] E. F. Steennis, E. Hetzel, and C. W. J. Verhoeven. Diagnostic medium voltage cable test at 0.1 Hz. In *Proceedings of the 3rd IEEE International Conference on Insulated Power Cables*, pages 408–414, 1991.
- [SNPB05] S. Sriram, S. Nitin, K. M. M. Prabhu, and M. J. Bastiaans. Signal denoising techniques for partial discharge measurements. *IEEE Transactions on Dielectrics and Electrical Insulation*, 12(6):1182–1191, Dec. 2005.

- [SSS00] I. Shim, J. J. Soraghan, and W. H. Siew. Digital signal processing applied to the detection of partial discharge: an overview. *IEEE Electrical Insulation Magazine*, 16(3):6–12, May/June 2000.
- [Sto05] G. C. Stone. Partial discharge diagnostics and electrical equipment insulation condition assessment. *IEEE Transactions on Dielectrics and Electrical Insulation*, 12(5):891–904, 2005.
- [Vee05] J. Veen. *On-line signal analysis of partial discharges in medium-voltage power cables*. Ph.d. thesis , Eindhoven University of Technology, the Netherlands, 2005.
- [ZYJZ05] J. Zhu, L. Yang, J. Jia, and Q. Zhang. The design of rogowski coil with wide band using for partial discharge measurements. In *Proceedings of 2005 International Symposium on Electrical Insulation*, pages 518–521, 2005.
- [ZZK05] X. Zhou, C. Zhou, and I. J. Kemp. An improved methodology for application of wavelet transform to partial discharge measurement denoising. *IEEE Transactions on Dielectrics and Electrical Insulation*, 12(3):586–595, 2005.

ABSTRACT

This doctoral thesis is comprised of five parts. The first three parts concern signal processing and electromagnetic modelling of multiport antennas. The last two parts concern signal processing and transmission line theory applied to wave splitting on transmission lines.

In Part I, the spherical vector wave expansion of the electromagnetic field is used to completely characterize a multiport antenna. A general framework for modelling an antenna configuration based on measurement data and numerical computation is obtained. The generic electromagnetic model for arbitrary multiport antennas or vector sensors is applied in direction of arrival (DOA) estimation.

Next, in Part II using the generic electromagnetic model (from Part I), we obtain the Cramér-Rao bound (CRB) for DOA and polarization estimation using arbitrary multiport antennas. In the Gaussian case, the CRB is given in terms of the transmission matrix, the spherical vector harmonics and its spatial derivatives. Numerical examples using an ideal Tripole antenna array and a non-ideal Tetrahedron antenna array are included.

In Part III, the theory of optimal experiments is applied to a cylindrical antenna near-field measurement setup. The D-optimal (determinant) formulation using the Fisher information matrix of

the multipole coefficients in the spherical wave expansion of the electrical field result in the optimal measurement positions. The estimation of the multipole coefficients and corresponding electric field using the optimal measurement points is studied using numerical examples and singular value analysis.

Further, Part IV describes a Digital Directional Coupler (DDC), a device for wave splitting on a transmission line. The DDC is a frequency domain digital wave splitter based on two independent wide-band measurements of the voltage and the current. A calibration of the digital processor is included to account for the particular transmission line and the sensors that are employed. Properties of the DDC are analyzed using the CRB and an experiment where wave splitting was conducted on a coaxial-cable is accounted for.

Finally, in Part V the DDC has been designed and implemented for wave splitting on a medium voltage power cable in a power distribution station using low cost wide-band sensors. Partial discharge measurements are conducted on cross-linked polyethylene insulated power cables. The directional separation capabilities of the DDC are visualized and utilized to separate multiple reflections from partial discharges based on the direction of travel.

